Optically addressed light modulators using an organic photovoltaic layer

Thomas Regrettier

▶ To cite this version:

Thomas Regrettier. Optically addressed light modulators using an organic photovoltaic layer. Micro and nanotechnologies/Microelectronics. Université de Strasbourg, 2017. English. NNT : 2017STRAD038 . tel-02917964

HAL Id: tel-02917964

https://theses.hal.science/tel-02917964

Submitted on 20 Aug 2020

UNIVERSITÉ DE STRASBOURG

ÉCOLE DOCTORALE 269 MSII

Laboratoire ICube UMR 7357

THÈSE présentée par :

Thomas REGRETTIER

Soutenue le : **8 décembre 2017**

Pour obtenir le grade de : **Docteur de l'Université de Strasbourg**

Discipline/ Spécialité: Sciences de l'Ingénieur, Électronique et Photonique

Modulateurs de lumière à commande optique composés d'une couche photovoltaïque organique

Optically addressed light modulators using an organic photovoltaic layer

THÈSE dirigée par :

M. HEISER Thomas	Professeur, Université de Strasbourg, France

RAPPORTEURS:

M. NEYTS Kristiaan	Professor, Ghent University, Belgium
M. COLSMANN Alexander	Doctor, Karlsruhe Institute of Technology (KIT), Germany

---

AUTRES MEMBRES DU JURY:

Mme. KACZMAREK Malgosia	Professor, University of Southampton, United Kingdom
M. ADAM Philippe	Docteur, RDS Photonique, DGA/MRIS, France
M. MERY Stéphane	Chargé de recherche, IPCMS (CNRS), France

Science is made up of so many things that appear obvious after they are explained.

Frank Herbert, Dune

Acknowledgments

I would like to express my appreciation to all of you who make our common work together possible.

This thesis is part of a collaborative work between the University of Southampton and the University of Strasbourg. The UK-France PhD programme jointly managed by DSTL and DGA funded it. Thank you for providing such opportunities.

I am delighted to welcome and thank the members of my jury particularly Kristiaan Neyts and Alexander Colsmann that accept to assess this manuscript. A special thought for Malgosia Kaczmarek with whom I look forward to continuing this work.

I further wish to acknowledge the notable role of Giampaolo D'Alessandro and Christopher Burgess who have a different, but most of all, very interesting and inspiring ways of reasoning.

I do not forget to thank the scientific workforce of Southampton, especially Matthew Proctor who welcomed me to this magnificent city, as well as Nina Podoliak, Andrew Acreman and Elena Mavrona.

I apologize to the British readers if they feel offended, but I need to move on to a more subtle and elegant language.

Je tiens à remercier Philippe Adam et Stéphane Méry, membres francophones de mon jury d'avoir montré de l'intérêt pour mon travail.

Je tiens surtout à exprimer ma reconnaissance aux personnes qui m'ont encadré lors de mon passage au laboratoire, en commençant par le principal instigateur de ce projet, Thomas Heiser, sans qui rien n'aurait été possible. Tu as des qualités rares pour un encadrant, tu t'imposais, malgré un emploi du temps chargé, de suivre l'avancement de mes travaux de manière hebdomadaire, afin de me donner tes conseils et tu t'es toujours rendu disponible lorsque j'en avais besoin.

Je dois aussi remercier Patrick Lévêque d'avoir pris sur son temps et de m'avoir très bien formé lorsque j'étais stagiaire. Pour finir une course de fond, l'important, c'est de donner la bonne impulsion au départ.

Dans la même idée, je tiens à exprimer toute ma reconnaissance aux enseignants qui m'ont permis d'en arriver là. Pour m'avoir intéressé à la physique des composants, je remercie les professeurs Adele Carradò et Daniel Mathiot. Sans oublier tous les autres intervenants de la licence ESA et du master MNE, Denis Muller en tête, qui est une équipe pédagogique à lui tout seul. Un grand merci à mes camarades de promotion Nicolas Bresson, Hugo Machado, Jovan Nikolic et Jérémy Schlachter, je vous souhaite ce qu'il y a de meilleur pour le futur.

J'ai aussi eu la chance d'intervenir à l'IUT de Schiltigheim durant ma thèse grâce à deux de mes anciens enseignants : Denis Montaner et Gérald Ferblantier. Je vous suis reconnaissant de m'avoir donné cette opportunité.

Je remercie aussi le duo de choc composé de Jérémy Bartringer et de Nicolas Zimmerman qui m'a aidé à mettre en place des bancs de mesure ainsi que le reste de l'équipe administrative et technique du laboratoire : Marina Urban, Nicolas Colin, Stéphane Roques, Sébastien Schmitt et Florent Dietrich ("Liewer met de gläser ahnstosse àls met de käpf").

J'aimerais aussi remercier l'ensemble des gens avec qui j'ai pu avoir des discussions intéressantes et qui ont pu m'aider, d'une façon ou d'une autre, à débloquer des situations qui semblaient impossibles à résoudre. Je veux bien sûr parler de Nicolas Leclerc, Caroline Eckert, Rony Bechara, Frédéric Lincker, Sadiara Fall et Laure Biniek.

J'aurai toujours une pensée pour mes collègues doctorants, qui ont été, ou sont encore en thèse au laboratoire : Laurent Osberger, Abdellatif Chelouche, Nacereddine Boubiche, Octavian Maciu, Maroua Garci, Olzhas Ibraikulov, Tianyan, Imane Malass, Peter Lienerth, Rémy Claveau et Fitsum Aweke.

Pour finir, je souhaite remercier ma famille, ma mère, ainsi que mes deux sœurs Pauline et Marie, qui m'ont soutenu durant cette période.

Acknowledgments

À Sarah et à ma fille Liv : comme je n'ai jamais su exprimer mes sentiments aux gens qui comptent le plus dans ma vie, je préfère laisser ce travail aux personnes compétentes.

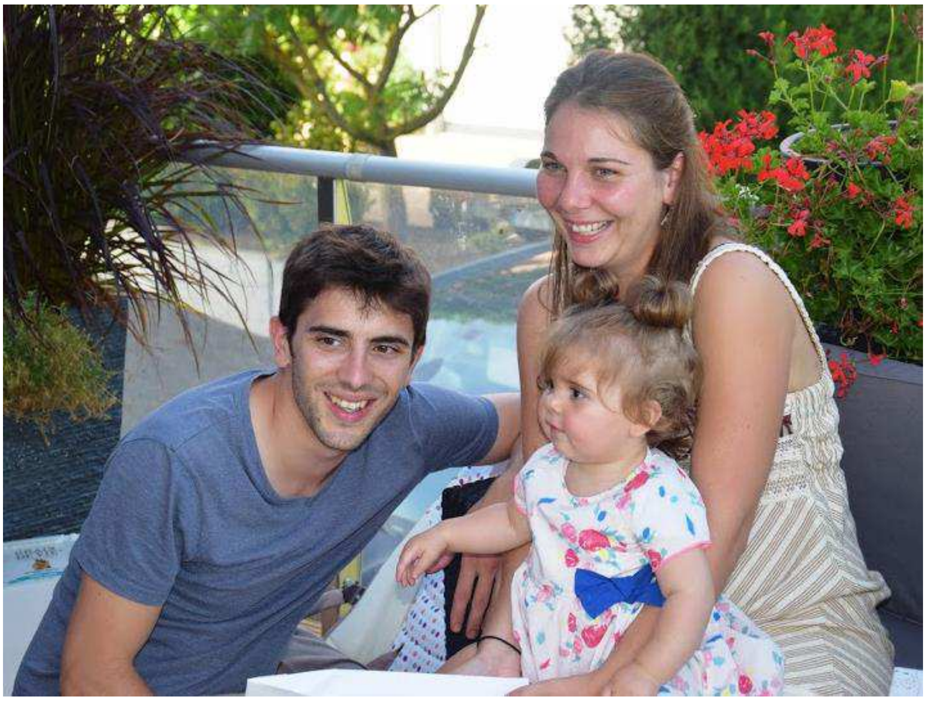

Comme l'a si bien dit Jean d'Ormesson: "Tout le bonheur du monde est dans l'inattendu."

Contents

Contents

Contents

List of Abbreviations

A	*Acceptor*
AL	*Alignment layer*
C_{60}	*Buckminsterfullerene*
CPI	*Cross-Polarized Intensity*
D	*Donor*
DGA	*Direction Générale de l'Armement*
DSTL	*Defence Science and Technology Laboratory*
EA	*Electron Affinity*
HOMO	*Highest Occupied Molecular Orbital*
IP	*Ionisation Potential*
ITO	*Indium Tin Oxide*
LC	*Liquid Crystal*
LCD	*Liquid Crystal Display*
LCLV	*Liquid Crystal Light Valve*
LUMO	*Lowest Unoccupied Molecular Orbital*
LV	*Light Valve*
OASLM	*Optically Addressed Spatial Light Modulator*
OFET	*Organic Field-Effect Transistor*
OLED	*Organic Light-Emitting Diode*
ORFID	*Organic Radio-Frequency Identification Devices*
P3HT	*Poly(3-hexylthiophène-2,5-diyl)*
PCBM	*[6,6]-Phenyl-C61-Butyric acid Methyl ester*
PCL	*Photoconductive Layer*
PEDOT	*Poly-(3,4-ethylenedioxythiophene)*
PEIE	*Polyethylenimine-ethoxylated*
PSS	*Polystyrene Sulfonate Sodium*
PVK	*Poly-(N-vinyl carbazole)*
PVL	*Photovoltaic Layer*
SCLC	*Space charge limited current*
SLM	*Spatial Light Modulator*
WF	*Work Function*

1 Introduction

Who can predict the future impact of scientific discoveries in people's daily lives? Today's adds exhort us to buy the novel Organic Light-Emitting Diode (OLED) [1] television stating that "life is in every pixel". The road that led to this scientifically questionable but catchy slogan was long. It necessitated a considerable amount of efforts, time and long debates.

When Faraday discovered in 1833 [2], that, in some materials, electrical conductivity can be enhanced with increasing temperature, he did not realize that he made the first documented observation of a material class that we now call semiconductor. In addition, it was impossible for Friedrich Wöhler to anticipate the fact that when he synthesized urea in 1828 [3], organic synthesis will be another option to tailor semiconductors. At that time, scientific issues were different, but thanks to them and countless scientists, organic electronic was able to see the light of day.

Nowadays, conventional electronics mainly rely on inorganic semiconducting materials such as amorphous or crystalline silicon. Nonetheless, times are changing and silicon starts to be partially substituted by plastic electronics. It is a slow ongoing metamorphosis, only visible to the general public via commercial advertisements. Even though the main market for organic electronics is the OLED display's technology, other applications may find their way into our daily lives: OLED lightning [4], Organic Solar Cells (OSC) [5], organic field-effect transistor (OFET) [6], and Organic Radio-Frequency Identification Devices (ORFID) [7], to mention just a few.

For longer-term applications, organic materials are possible candidates as laser gain material [8], for thermoelectricity [9], or magnetoresistance applications [10]. More specifically, in our research team at ICube laboratory, organic semiconducting materials have been used for organic solar cells [11], to tailor gas sensors [11] and in 2014, via a French-UK collaboration, I started working on implementing these materials in Optically Addressed Spatial Light Modulators (OASLM) [12]. The latter is the main topic of my PhD project.

It is important to know that this subject gathers experts from different fields: Mathematics, optics, physics of semiconductors, organic chemistry and electronics. As a consequence, the people involved in my project work often originate from different disciplines and countries. Will I be capable to understand the very essence of what these people have to teach me? Fortunately, everyone speaks English, and therefore the language is not the main barrier. Nevertheless, I was not prepared after a master's degree in microelectronics to deal with the fact that these people do not necessarily speak a common scientific language. It turns out that each scientific field has its own dialect, each community has its specific characteristics. For this reason, I realized that I needed to become proficient in basic communication skills with chemists, mathematician… This observation leads us to the next question.

Am I competent to work on this subject? I quickly understood that the answer is no. However, it has to be like this. At first, when I read the project, it seemed simple and I was confident. Replacing one inorganic photoconductor with its organic counterpart seemed easy. Yet, as the years went by, the well-defined outline of the project became more and more fuzzy. Who could predict with assurance the result of experiences not yet performed? This is the reason why I am writing this manuscript. A student without prior knowledge of the subject might be the more qualified for the job because he has time to learn and "try different things that have a low success rate" in other terms doing research.

During the bibliography phase inherent to every PhD student, I realized that all books or communications in my field of studies were very specific to a scientific domain. Consequently, it was difficult to understand them at first. For example, from a chemist point of view, liquid crystals are molecules with a certain chemical structure. Therefore, if chemists write a publication or a book, they will focus on the synthesis of liquid crystals. From a physical point of view, liquid crystals are rod-shaped molecules with a dipole. They consider liquid crystals as a molecule or mixture of molecules defined by physical parameters, for example, refractive index, elastic or dielectric constants. In order to simplify complex problems, some parameters should be set aside. The issues are also not exactly the same when it comes to the manufacturing of liquid crystal devices, which is the perspective of an engineer. With no prior knowledge of such a vast domain, a life is not long enough to become an expert. Nevertheless, one has to start somewhere and unfortunately, I did not find a book named OASLM “for beginners” when I began my thesis.

I hope that this manuscript will be more accessible to students or researchers that may have an interest for this topic and that by reading this document, they will be less lost than I was at the time. This might be the harder part to succeed and it is up to you, the reader, to decide if I have accomplished this last task.

Light valves (LV) and optically addressable spatial light modulators (OASLMs) are now part of a well-established technology. Currently available designs mainly rely on combining a photoconductive inorganic window, such as crystalline semiconductors (Gallium arsenide (GaAs) [13], Silicon (c-Si) [14]…) or amorphous silicon (a-Si) [15] with a liquid crystal layer. While reliable, their design is mainly limited to the reflection mode, as these photoconductors are strongly absorbing in the visible part of the spectrum. The spatial resolution of such devices is limited by charge diffusion in the photoconductive layer due to their inherently high charge carrier mobilities. In addition, the production costs of these technologies remain high.

For all these reasons, photosensitive organic semiconductors [16], [17] can compete with their inorganic counterparts for OASLM applications. They are not only responsive to light but are also easily processed at low cost from solution or by sublimation under vacuum and their absorption spectrum can be tuned (through molecular engineering). Additionally, the typically three orders of magnitude lower charge carrier mobility of organic semiconductors compared to amorphous silicon limits lateral charge diffusion and should lead to an improved spatial resolution.

During my PhD project, I aimed to use a new class of organic semiconductors as the photosensitive layer in a liquid crystal OASLM, to investigate the underlying physical processes and to optimize the device performances.

The manuscript is organized as follows:

Chapter 2 repeats the general working principles of OASLMs followed by a detailed description of the different elements constituting such devices. The chapter will end with a presentation of the basic properties of organic semiconductors since these materials will be used as photosensitive layers in OASLMs.

Chapter 3 describes the different families of semiconductors used previously as photoconductive layers to tailor OASLMs. We will review the advantages and weaknesses of each technology such as inorganic crystals, inorganic thin films and organic semiconductors. In each case, we will describe the applications for which they have been designed or their potential uses.

Chapter 4 presents the organic semiconductors, P3HT and PCBM, used in my work and the OASLM fabrication procedure that I developed. The test bench that has been designed as well as the electro-optical characterization methods that I implemented, namely cross-polarized intensity (CPI), voltage transfer function (VTF), and impedance spectroscopy (IS), will be described in detail.

In Chapter 5 our first results obtained on liquid-crystal OASLMs will be described. A detailed analysis of CPI, VTF and IS data treatments will also be given. In order to better understand the impact of a change in the photoconductive layer impedance on the device response, the electro-optical response of a “standard”, i.e. non-photosensitive, LC cell will be presented. Although these tests were initiated to evaluate our device elaboration and characterization processes, the results give some useful hints for the interpretation of CPI, VTF and IS data obtained on OASLMs including an organic semiconductor layer. The last section covers the issue of OASLM spatial resolution. While our experimental set-up did not allow us to measure the resolution, I introduce a simple electrical model that allows us to clarify the link between the OASLM resolution and the electrical properties of the photosensitive layer.

Chapter 6 presents the behaviour of OASLMs including a blend of organic semiconducting materials (P3HT and PCBM) at different mass ratios. A detailed analysis of the experimental is given and reveals in particular that the organic layer does not behave as a standard photoconductive cell. The possible contribution of a photovoltaic effect to the device response is discussed.

Chapter 7 describes the changes brought in by modifying the nature of interfacial layers. In particular, the impact of interface engineering on photosensitivity, lateral resolution and LC alignment are discussed and used to rationalize the OASLM response. Finally, new routes to increase the performances of photovoltaic OASLMs will be presented.

2 SCIENTIFIC BACKGROUND

In this chapter, we will begin by describing the working principle of optically addressed spatial light modulators (OASLMs). Afterwards, we will give more details on the different elements constituting such devices. Finally, we will discuss the reasons leading us to use organic semiconductors as photoactive materials in OASLMs.

2.1 Optically Addressed Spatial Light Modulators

A spatial light modulator (SLM) is a device that controls light in two dimensions. It consists of an address part and a light modulation part. The information written in the address part changes the optical characteristics of the light modulation part. The modulation of the readout light properties such as polarization state or intensity is tuned by the command part, producing an optical output that reflects the written information.

The simplest example of a spatial light modulator that you can find in everyday life is addressed electrically. It is used to change the amount of reflected light on a two-dimensional pixelated array. In short the screen of your calculator. There are many varieties of spatial light modulators: SLMs can be reflective, transmissive or transparent, controlled electrically or, in our case, optically.

Unlike electrically addressed spatial light modulators (EASLM) that use an addressing circuit formed on a silicon substrate with a pixel array structure [18], optically addressed spatial light modulators (OASLM’s) use a photosensitive material to control the light modulation part [19]. Transmissive OASLMs are the subject of our studies. They are also referred to as "light valve". The light modulation material can be a non-linear optical crystal such as lithium niobate ($LiNbO_3$) [20], or more commonly a liquid crystal (LC) layer. The latter was used in the course of this thesis due to its unique feature to control light properties as a function of molecular orientation, which can be tuned by the application of an electric field. These devices are helpful for the treatment of optical information, like real-time incoherent to coherent conversion [21], projection displays [22], optical limiters [23] and holography [24] [25].

A typical LC device can be used to change light properties such as its polarization state or transmitted intensity as a function of an applied voltage. Its device structure is as follows: A LC material is sandwiched between two transparent conductive electrodes, generally made of Indium Tin Oxide (ITO) glass plates coated with a LC alignment layer such as polyimide (PI), which will be described later. An electric potential applied to both electrodes drops across the different layers according to their electrical properties (dielectric constant, thickness, resistivity…). As an example, if the alignment layer is more resistive than the LC layer, the potential drop will be more important across the alignment layer and vice versa. The potential drop occurring across the LC layer and thus the value of the electric field controls the orientation of the LC molecules, which affects the optical properties of the LC medium.

The above description forms the fundamental basis of OASLMs made of a LC and a photoconductive layer (PCL).

If we replace one of the alignment layers with a photoresistive material assuming for simplicity that it also acts as an alignment layer, its conductivity will vary as a function of illumination intensity. Therefore, the potential drop across the LC cell and consequently the LC molecular orientation affecting the light properties will depend on light intensity as depicted in Figure 1.

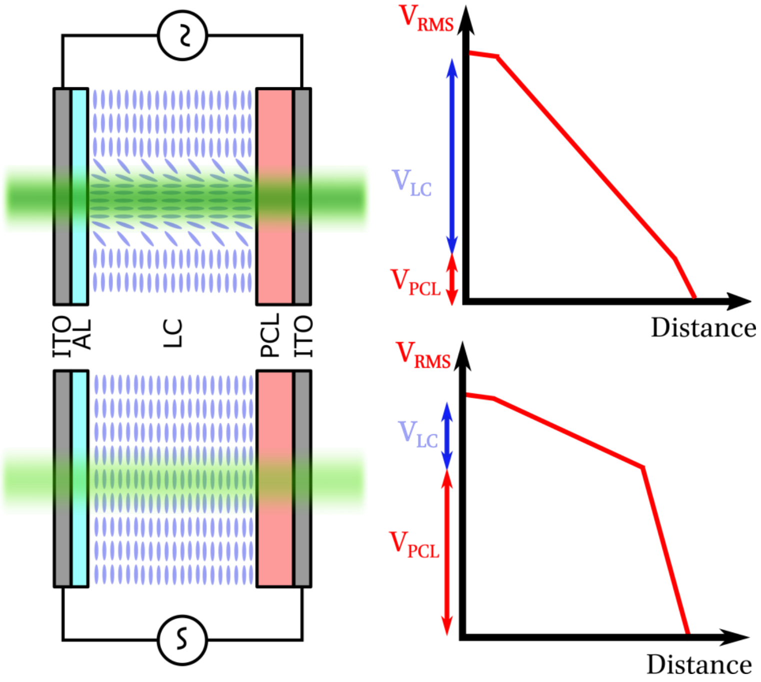

Figure 1: Schematic representation of a transmissive OASLM. Liquid crystal (LC) is sandwiched between two conductive glass slides (ITO), one of the ITO glass slides is coated with a thin insulating polymer layer, which serves as an alignment layer (AL), and the other ITO glass slide is coated with a photoconductive layer (PCL). Depending on illumination intensity, charge carriers are generated, which modifies the PCL impedance and change the voltage drop across the PCL layer (V_{PCL}) consequently altering the voltage drop across the LC layer (V_{LC}).

A polarized incident light ray interacts strongly with such a device. This is due to the peculiar optical property of liquid crystalline materials known as birefringence. This physical property will be the subject of the next section.

2.2 Liquid crystals

2.2.1 Propagation of light through a birefringent medium

To change the properties of an incident light beam (phase, intensity or polarisation), materials with anisotropic optical properties are generally used. Anisotropic crystals like calcite have crystallographically distinct axes and interact with light in a manner that is dependent upon the orientation of the crystalline lattice with respect to the incident light. The refractive index of such an anisotropic crystal is dependent on the direction and polarization of light. Here we focus on uniaxial mediums that possesses two different refractive indices (n_o

and n_e respectively ordinary and extraordinary refractive index) also called uniaxial materials. Birefringence (Δn) is defined by the difference between the extraordinary and ordinary refractive indices of the material ($\Delta n = n_e - n_o$).

Figure 2 illustrates the effect of linearly polarized light travelling through a birefringent medium. In this arrangement, the transmission axis of the linearly polarized light (dashed black line) is half-way (45°) between the horizontal and vertical axis of the medium (black axis). Both, the vertical (blue line) and the horizontal (red line) components are initially in phase. When the light propagates through the birefringent medium, both components experience different refractive indices ($n_o \neq n_e$) and therefore different phase velocities $v_0 = \frac{c}{n_0}$ and $v_e = \frac{c}{n_e}$ (c: Speed of light in vacuum). In this example, the refractive index of the vertical component is supposed to be higher than the horizontal one, i.e. the blue component “slows down”. Therefore, the phase difference between the two components increases as light travel through the medium. Their sum (black dashed line) or polarization is changing. In the example Figure 2, when the light ray exits the material, the originally linearly polarized light is elliptically polarized at the output.

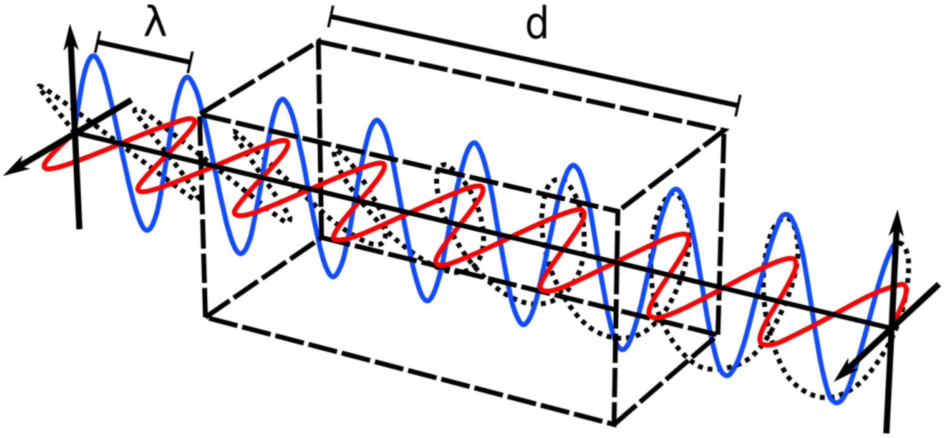

Figure 2: Propagation of light through a birefringent medium

Polarization at the output varies as a function of light wavelength (λ), material thickness (d), birefringence (Δn) and polarization at the input.

Waveplates are a common application of birefringent crystalline material and are often made of quartz. Careful adjustment of the crystal thickness is used to set the phase difference between both components of a specified wavelength to either π (half-wave plate) or π/2 (quarter-wave plate).

2.2.2 Liquid crystalline state

The first rule that we learn in school about states of matter is that three states exist: solid, liquid and gas. Nevertheless, if a rule exists, it has exceptions. In the field of matter states, one of these exceptions is the liquid crystalline state.

Although there seem to be some contradictions within the term “liquid crystal” (LC), it implies that these materials possess properties from both states. A material in the liquid crystalline phase is fluid and, when observed under polarized light, shows birefringent properties, indicating some order within the material.

In the 1880s, Friedrich Reinitzer an Austrian chemist and botanist discovered the first liquid crystal phase while working on cholesteryl benzoate. He found that this material possessed two melting points. At 145.5°C, the crystal melted into a distinctive state, which exists until 178.5°C where it became liquid. Convinced that his unusual observations were an important discovery, he collaborated with Otto Lehmann who obtained his PhD at the University of Strasbourg under the direction of crystallographer Paul Groth. Using a heating stage on a microscope with polarizing filters, he made experiments that confirmed Reinitzer's initial observations. Together they discovered this new state of matter, showing that something in-between solid and liquid exists. There are different classes of LC materials. The work of Georges Friedel established a classification scheme of the different LC phases. In this work, we will focus on thermotropic nematic (rod-like) LCs.

Nematic liquid crystals are composed of molecules that have a longitudinal, rod-like shape. This class of thermotropic LCs possess a nematic phase within a certain temperature range, as shown Figure 3. Below the melting temperature (Tm), the material crystallizes and each molecule has its specific position forming a periodic arrangement. Above the clearing temperature (Tc), the positions of the molecules are randomly distributed and the material acts as an isotropic fluid. Between these two points, the nematic phase exists. The periodic arrangement is lost and molecules orient themselves due to neighbouring molecules. An average director represents the average direction of all molecules $\vec{n}$, but individual molecules may be more or less aligned with this vector.

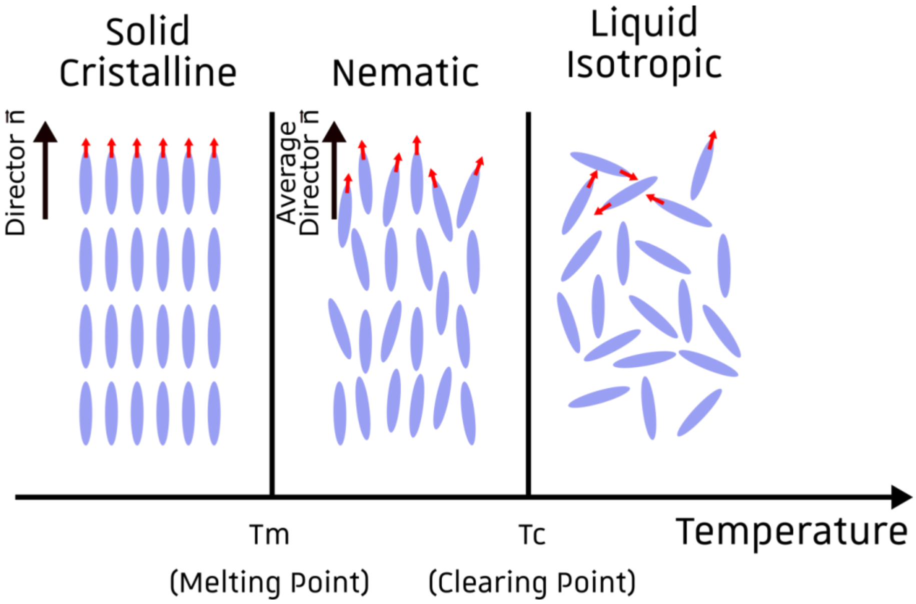

Figure 3: Phase of thermotropic liquid crystalline material as a function of temperature.

In the nematic phase, the material appears milky, because many small domains exist (except if a special treatment has been applied), each with its own orientation.

2.3 Alignment layer

By depositing a layer of LCs on a glass substrate, the molecules will not be uniformly oriented along a single direction. However, most optical applications require a well-defined LC orientation. The deposition of a thin polymer film over the substrate subsequently rubbed using a rotating cloth, as depicted in Figure 4, permits the alignment of the LC molecules. The contact between the cloth and the polymer layer creates microscopic grooves on the surfaces of the polymer and aligns polymer chains [26]. Non-contact methods do also exist, such as photo-alignment, which uses polarized UV light to generate order on a photo-alignable material. In this work, we will exclusively use the rubbing method.

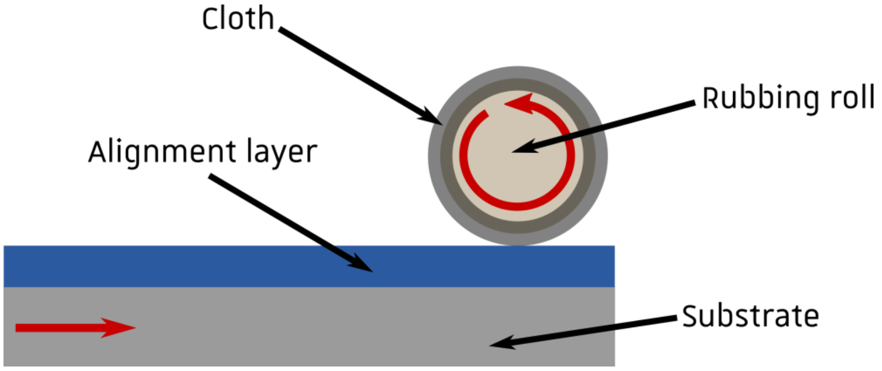

Figure 4: Generation of uniform alignment with the rubbing technique, a rubbing cloth is taped on a rotating drum, the polymer-coated substrate is moving toward the rotating drum. This treatment forces the organisation of the first layer of molecules.

Polyimides, whose structure is displayed in Figure 5, are an example of polymers routinely used as alignment layer material. They exhibit high thermal stability, are lightweight, cheap and easy to deposit.

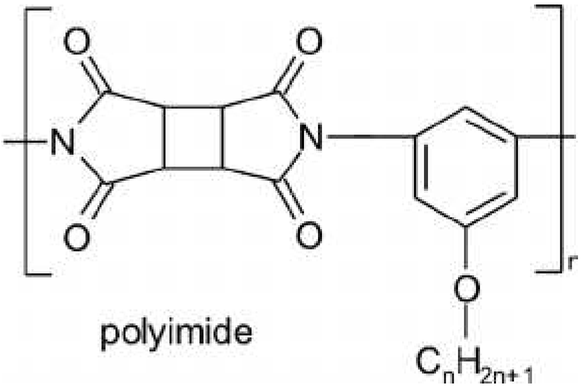

Figure 5: Chemical structure of polyimide

2.3.1 Operating principle of LC devices

LCs and alignment layers introduced in the previous section are the building blocks of liquid crystal devices.

The main applications of LCs are display devices (LCDs). In its simplest form, the LC material is sandwiched between two substrates with electrodes and alignment layers facing the inside of the cell. When a voltage is applied to the electrodes, an electric field is created which applies a torque to the LCs molecules so that their orientation is modified. It is important to note that the voltage applied needs to be superior to a certain threshold value called the Fréedericksz transition. Below this value, no reorientation occurs. Its value depends on the liquid crystalline material used. When LCs molecule reorients, the birefringence value changes, leading the incident polarized light to a different polarization state.

Generally, LC molecules possess an electric dipole moment. The electric dipole can be parallel to the long axis of the molecule, as shown in Figure 6, or perpendicular to the long axis of the molecule, as depicted in Figure 7. The chemical structure of the LC molecules affects the direction of the electrical dipole moment, which in turn leads to different electrical and optical properties. Above a critical voltage, the molecular dipoles reorient parallel to the electric field.

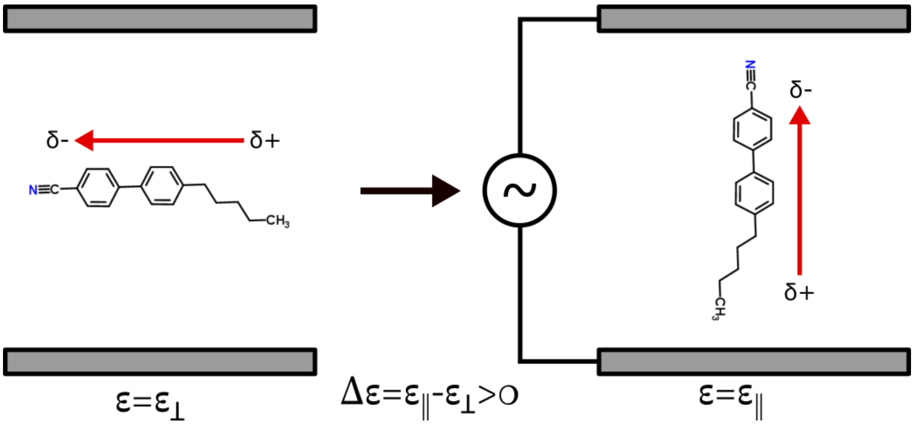

Figure 6: Nematic LC molecule with an initial planar orientation with respect to the substrate surface, a longitudinal dipole moment and positive dielectric anisotropy.

The direction and amplitude of the dipole moment of the molecule determine the dielectric anisotropy defined as $\Delta\varepsilon = \varepsilon_{\parallel} - \varepsilon_{\perp}$, with $\varepsilon_{\parallel}$ and $\varepsilon_{\perp}$ being the dielectric constants parallel and perpendicular to the average direction of the LC molecule's long axes, respectively. LC molecules with a dipole moment directed along their long molecular axis lead to positive dielectric anisotropy ($\Delta\varepsilon = \varepsilon_{\parallel} - \varepsilon_{\perp} > 0$), whereas LC molecule with a dipole moment direction perpendicular to their long molecular axis leads to negative dielectric anisotropy ($\Delta\varepsilon = \varepsilon_{\parallel} - \varepsilon_{\perp} < 0$).

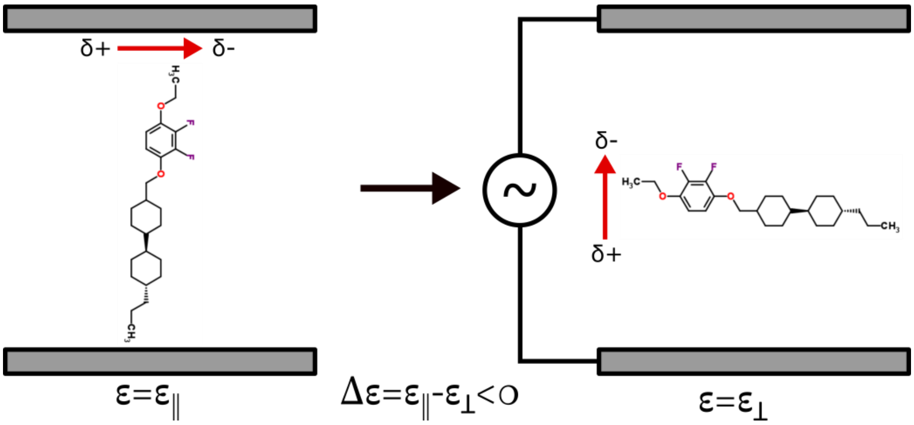

Figure 7: Nematic LC molecule with an initial vertical orientation with respect to the substrate surface, a transversal dipole moment and negative dielectric anisotropy.

Commercially available liquid crystalline materials are rarely composed of a single molecule. Different LC molecules are blended together forming a so-called mixture. The liquid crystal optoelectronic properties, such as the Fréedericksz threshold voltage, birefringence etc. depends on the type of LC materials used and on their molar ratio.

Apart from the mixture composition, device engineering is another way to tune the response of a LC cell. The substrate properties need to be taken into account in order to align LC molecules. For instance, the alignment layer used to obtain an initially vertical orientation of 90° is different from the one used to obtain a planar orientation (0°).

It is sometimes desirable to form a small angle (also known as the pre-tilt angle) between the LC molecules and the substrate plane to reduce the threshold voltage or to increase the switching speed. The counterpart is that doing so, the LC cell birefringence diminishes because the molecules are already tilted before the application of an electric field.

An angle can also be formed between the two aligning substrates, which results in a twisted cell. The discovery of the so-called twisted-nematic effect was a breakthrough that permitted the use of LCs in displays [27] (see below). This type of cells is used to control the intensity of transmitted light. When placed between properly arranged polarizers, each polarizer is oriented with its axis parallel to the rubbing direction of the adjacent electrode (so that the polarizer and analyzer are crossed), the LC pixel appears transparent due to the induced rotation of light in the LC cell waveguide by 90°. When a voltage is applied, the LC molecules reorient, the birefringence tends toward zero and the LC cell becomes dark.

2.3.1.1 Examples of LC devices

In my thesis, I mainly used homogeneously aligned anti-parallel cells (where the top and bottom substrates are rubbed in the opposite direction, to avoid a splay deformation [28]). This corresponds to a liquid crystal device geometry that is used to change the polarization of light as a function of the applied voltage. Figure 8 depicts the two different types of LC cells and their respective response as a function of an applied bias.

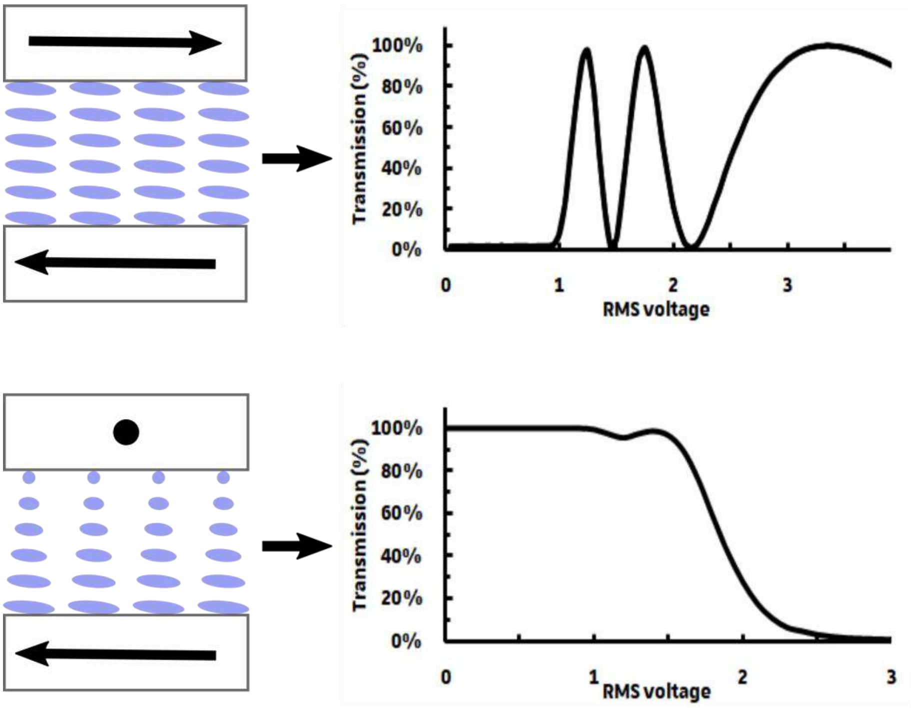

Figure 8: On top homogeneously aligned anti-parallel LC cell structure (left) and light transmission as a function of the applied bias (right). Below, homogeneously aligned Twisted Nematic cell structure (left) and light transmission as a function of the applied bias (right). The arrows indicate the rubbing direction both cells are filled with a liquid crystal mixture known as E7 that will be described later.

The transmission versus voltage curve of a homogeneously aligned anti-parallel cell is a consequence of the LC birefringence properties that was discussed in section 2.2.1. When a monochromatic ray of light is polarized at 45° with respect to the slow and fast axis of the LC material, its output polarization at the cell exit depends on the wavelength of the light, the cell thickness and total birefringence of the LC material. In the example shown in Figure 8, the output polarization is opposite to the polarizer (analyzer) axis and the fact, that without applied bias the cell transmission is close to null, depicts this particular case. With increasing applied voltage, we observe the Fréedericksz transition (around 1V) after which the LC molecules start to reorient inducing a birefringence decrease resulting in a different polarization state at the cell output.

In the twisted nematic configuration, the directions of the LC molecular alignment on both plates exhibit an angle of 90°. This induces a continuous rotation of the long axes of the liquid crystal molecules across the LC layer thickness. The polarisation direction of linearly polarized light travelling through such a twisted-nematic configuration follows the rotation of the molecule's long axes (this is the so-called twisted-nematic effect). At the cell output, the light is rotated by 90°, following the twist formed by the LC molecules. When such a layer is placed between linear cross polarizer with its axis parallel to the rubbing direction of the adjacent electrode, the light rotates by 90° due to the LC cell and can pass the second (crossed) polarizer. Inversely, if the second polarizer direction is the same as the first polarizer, the light is blocked. In Figure 8, the polarizers are crossed and the wavelength monochromatic. With increasing voltage, the LC molecules reorient, breaking the twisted configuration so that the light polarisation does not rotate by 90° and is blocked. This principle is still used nowadays for displays based on the twisted nematic effect.

2.3.2 Liquid crystal devices driven by a DC field

Ions are always present in liquid crystals. They may result from an undesired contamination during cell manufacturing. The glue used to encapsulate the cell, as well as the spacers and alignment layers, may contain ions that can diffuse into the LC.

Unwanted ionic contamination is known to have a negative impact on the LC cell performances and many studies have been made to reduce ionic contamination. For example, the use of nanoparticles that trap ions and decrease the overall ionic conductivity of liquid crystals, have been reviewed in reference [29].

One detrimental effect of ionic contamination occurs when the LC cell is driven by a DC bias. When a DC electric field is applied across a LC cell, ions start to drift towards their respective electrodes (which are supposed to be impermeable to ions): positive ions move towards the negatively charged electrode and negative ions towards the positive electrode. As a result, accumulated ions compensate the charges accumulated at the electrode and the potential gradient is limited to a region close to the electrodes. In addition, selective adsorption of ions by the alignment layer cause an irreversible performance degradation of the LC cell subjected to a DC bias [30].

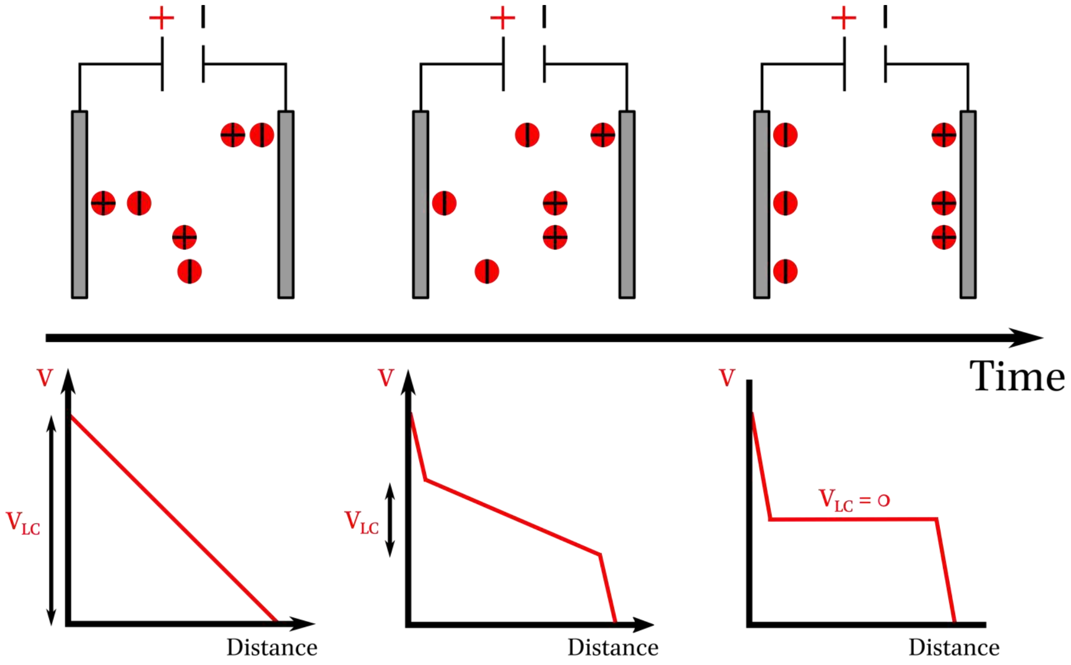

Figure 9: Schematic representation of ionic charge build-up and potential vs distance as a function of time when a LC cell is driven by a DC field.

This effect is commonly referred to as electrical double layer (EDL). It cancels the effect of the voltage on the liquid crystal orientation. For this reason, LC-based devices are generally driven by AC fields.

2.4 Photoconductive layer

Photoconductivity is the phenomenon that gives rise to a change in the electrical resistivity of a material upon illumination. This phenomenon is generally observed in semiconducting materials. The properties of semiconductors can be understood in terms of the band structure sketched in Figure 10. The valence and conduction energy bands indicate the possible energy states of the most weakly bonded electrons in the crystal and are separated by an energy gap or bandgap (Bg). At thermal equilibrium, the probability that an electron occupies a state of energy E is given by the Fermi-Dirac function, which depends on the Fermi level position (E_F). The electrons occupying states of the conduction band (so-called conduction electrons) and empty states of the valence band (or holes) are responsible for the electrical conductivity. It is important to note that, according to the band theory, a full energy band (for instance the valence band at $0\ K$) does not contribute to an electrical current.

For a metal, the valence and conduction bands overlap (no energy gap). The resulting band is partially filled and leads therefore to a high conductivity. In an insulator, both bands are separated by a large bandgap (Bg), that renders the probability for an electron to reach the conduction band negligible. Finally, semiconductors possess a small bandgap (1-3 eV). At non-zero temperature, thermal energy allows electrons to transit from the valence band to the conduction band, leading to a non-zero temperature-dependent conductivity. These different situations are depicted in Figure 10.

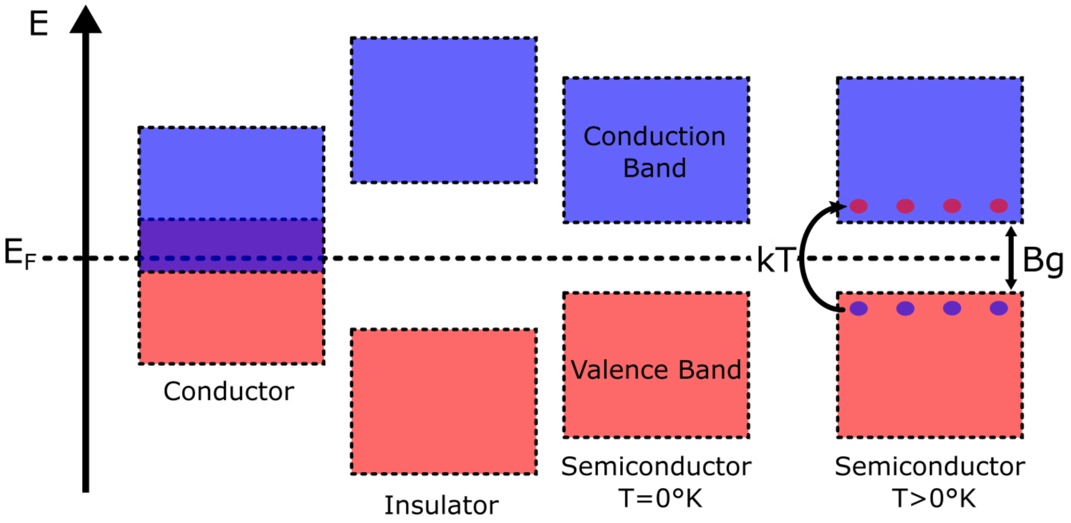

Figure 10: Schematic of band theory.

Light absorption is another way to excite electrons from the valence band to the conduction band, provided that the photon energy is larger than the bandgap. As depicted in Figure 11, the vacuum level is generally taken as a reference to define the conduction and valence band edges. The energy difference between the vacuum level and the Fermi level is the work function (W_F). The electron affinity (EA) is the energy gained if you add an electron from the vacuum to the bottom of the conduction band (Ec). Finally, the ionization potential (IP) is the amount of energy required to remove the most loosely bound electrons from the valence band (Ev).

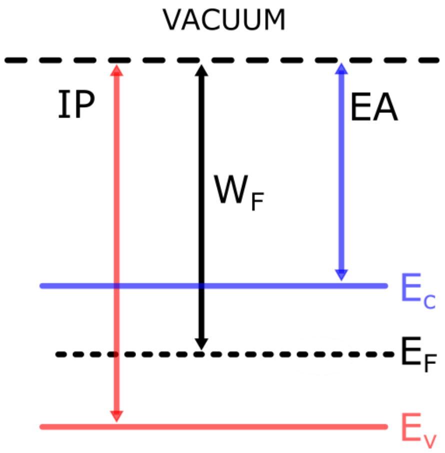

Figure 11: Energy band relations

A photoconductor is generally composed of a slab of semiconductor (in bulk or thin film form) with ohmic contacts affixed to opposite ends. By definition, “Ohmic contacts” induce a negligible voltage drop, compared to the voltage drop across the semiconductor bulk, when current is flowing across the device. Under illumination, free charge carriers (i.e. conduction electrons and holes) are generated either by band-to-band transitions (intrinsic) or by transitions involving forbidden-gap energy levels (extrinsic). In both cases, the conductivity increases [31].

From the previous definition, we learn that two routes exist in order to generate free carriers from light absorption. The first one is to use photons whose energy is higher than the bandgap energy difference, also called intrinsic transition. In this case, the long wavelength cutoff is given by:

$$\lambda_c = \frac{hc}{\nu} = \frac{1240}{B_g(eV)}\ (nm)$$

where h is the Planck constant, c the light celerity and λ_c is the wavelength corresponding to the semiconductor bandgap Eg. For a photoconductor, the conductivity is given by:

$$\sigma = q(\mu_n n + \mu_p p),$$

where μ_n and μ_p are the electrons and holes mobility, n and p are the electron and hole densities and q the elementary charge. The increase of conductivity under illumination is mainly due to the increase in the number of carriers. "Semi-insulating (SI)" or intrinsic (undoped) semiconductors with a low charge carrier density are generally used. In this case, a low light intensity is sufficient to generate more charge-carriers than the density already present in the dark state. The density of charge carriers in the dark state is therefore an important parameter that influences the sensitivity (detectivity) of the photoconductor.

For sub-bandgap or extrinsic transitions, discrete energy levels within the band-gap, due for instance to defects in the crystalline lattice or impurities, must be present. In such cases, the long wavelength cutoff is determined by the defects energy level position within the bandgap.

Generally, inorganic materials (such as amorphous silicon, $BaTiO_3$, CdTe, GaAs, InP...) are used as photoconductive layers. Unfortunately, these photosensitive materials are generally thick (hundreds of micrometres) and decrease the OASLM's transparency. Moreover, the high charge carrier mobility in some inorganic photoconductive crystals lead to lateral charge diffusion that limit the spatial resolution of OASLM devices [32]. In addition, the production costs of these materials remain high. Replacing inorganic photoconductors with novel organic photoconductors having the potential to increase the resolution and reduce the OASLM production costs is the main motivation of my PhD thesis.

2.5 Organic semiconductors

Organic materials are carbon-based molecules or polymers that can adopt a crystalline, semi-crystalline or amorphous structure. We can categorize organic materials into two families. Low molecular weight materials or small molecules and higher molecular weight polymers. This difference has its importance when it comes to implement the material in a device. Though both polymers and small molecules can be deposited in thin layers using a wet deposition method (spin-coating, doctor blading, inkjet printing ...), only small molecules can be thermally evaporated.

Rather than using crystalline inorganic semiconductors, whose arrangement of atoms in crystalline lattice gives rise to delocalised electronic states and band structure, an alternative approach is to use organic semiconductors with intrinsic semiconducting behaviour. Semiconducting organic molecules include generally chains of sp^2-hybridised carbon atoms. The existence of π electrons, whose orbitals are delocalized along the molecular backbone give rise to the semiconducting properties. More or less random intramolecular coupling (between the molecular segments along the polymer chain) and/or intermolecular coupling (between the π orbitals of neighbouring molecules) give rise to a Gaussian distribution of the molecular orbital energy levels named

HOMO (Highest Occupied Molecular Orbital) and LUMO (Lowest Unoccupied Molecular Orbital) levels. These energy level distributions are named HOMO and LUMO band, respectively, and play a similar role to the valence and conduction bands of inorganic semiconductors. HOMO and LUMO are often referred to as frontier orbitals, and can respectively be determined by measuring the IP and EA of the material (see Figure 11 in the previous section). The HOMO (IP) and LUMO (EA) energy difference corresponding to the electrochemical bandgap of the organic semiconductor.

The fact that organic semiconductors can be processed from solution is a major advantage compared to rigid, thick (hundreds of microns) silicon wafers with a limited surface area obtained from Czochralski processes [33] at high temperature (more than one thousand degree Celsius). Organic materials are more flexible, thinner (hundreds of nanometers) and can be processed at low temperature (from room temperature up to a few hundreds of degree). Although it is unlikely to replace silicon by organic semiconductors in high-end electronic circuitry like central processing units, in view of the ease of implementation of these materials, applications that require flexibility and/or large areas might be cheaper to produce using organic semiconductors.

Unfortunately, organic materials have several drawbacks: lower charge-carrier mobility, sensitivity to ambient atmosphere (oxygen for instance) that affect their lifespan and one major drawback for the application of this project, which requires a high photosensitivity: the strong exciton binding energy and limited diffusion length.

2.5.1 Overcoming the exciton high binding energy and small diffusion length in organic semiconductors

Organic semiconductors (OSC) are van der Waals materials, i.e. low-density materials with weak intermolecular coupling, and are therefore characterized by a rather low relative permittivity ε_r (typically between 3 and 4). Therefore, absorption of photons with energies above the OSC band-gap generates coulombically bound electron-hole pairs (or “excitons”) rather than free charge carriers.

Dissociation of photo-induced excitons into free charge carriers may be achieved by introducing a heterojunction composed of an electron-donor (D) material (i.e. having a low ionisation potential) and an electron-acceptor (A) material (i.e. having a high electron affinity). If the differences in electron affinity and ionisation potential between both materials are sufficiently large (typically above 0.3 eV which correspond roughly to the exciton binding energy [34]), excitons generated close enough to the D/A interface may be dissociated into a pair of free charge carriers by charge transfer (CT) from the D to the A (or vice versa). An illustration of this concept is depicted in Figure 12. Note that to make this mechanism efficient, most photons need to be absorbed at a distance less than the exciton diffusion length to the D/A interface (i.e. typically less than 10 nanometers [35]).

To overcome this bottleneck, the concept of bulk heterojunction (BHJ) has been introduced a few decades ago [36] and has since allowed the development of organic photovoltaic devices with power conversion efficiencies exceeding 10%. In brief, in a BHJ the photon-absorbing layer is composed of a blend of D and A materials (Figure 12c) rather than of a planar D/A heterojunction (Figure 12b). Controlled micro-phase separation occurring during the film deposition or upon thermal annealing leads to an interpenetrated network of nanometre-sized D and A domains, with a large D/A interfacial area, making exciton dissociation highly efficient. The free charge carrier density (and therefore the electrical conductivity) in a BHJ increases upon exposure to light.

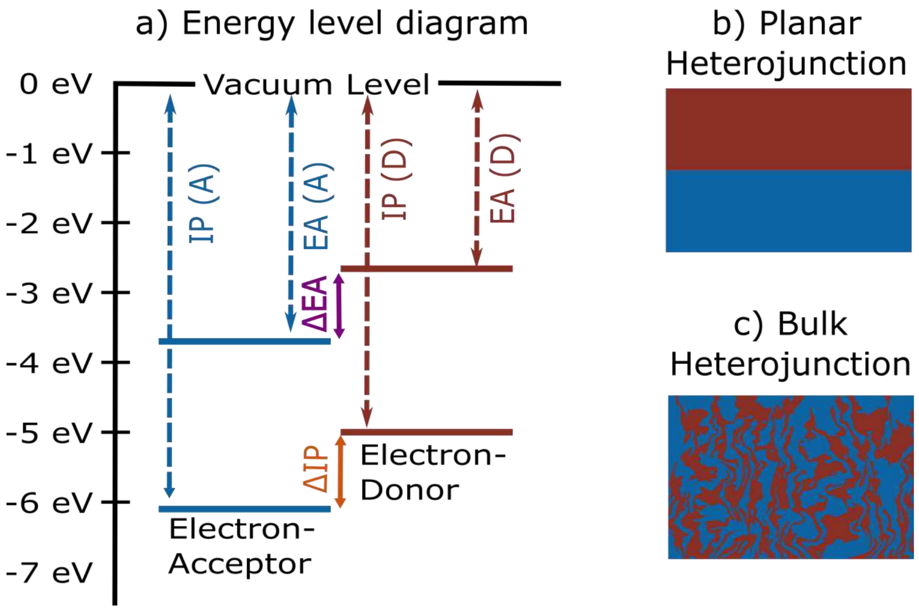

Figure 12: Energy level diagram of an organic heterojunction (a) and schematic representation of a planar (b) and bulk (c) heterojunction.

If similar electrodes are used on both sides of the heterojunction and if the random morphology is isotropic, a metal/BHJ/Metal device will act as a photoresistor. In other words, if no external voltage is applied, the free carriers will have no preferential pathway towards the electrodes. Therefore, no current should flow and no voltage difference should appear at the device electrodes under illumination.

2.6 Thesis in context

My thesis is in the continuity of the work done by the Soft Photonic Systems Group led by Professor Malgosia Kaczmarek from Southampton University. They have been working on OASLMs using PVK (Poly-(N-vinyl carbazole)) a polymer historically used as xerographic photoreceptors since 1970 [37].

PVK is an electron-donating molecule when blended with electron-accepting molecules such as fullerene (C_{60}) or trinitrofluorenone (TNF). It shows interesting photoconductive properties [37]. Due to its wide band-gap (3.5 eV) PVK possess the advantage of being almost transparent to visible light. Unfortunately, this system, although functional, suffers from several drawbacks.

Its operation in an OASLM has been found to be limited to low frequencies (< 1 Hz) [38]. Also if the conductivity (due to ionic impurity) of the LC mixture is too high, no liquid crystal modulation by light can be achieved [38]. To address these issues, novel organic materials circumventing those drawbacks are needed.

To address the need for novel organic semiconductors, a collaboration was initiated between the groups of Malgosia Kaczmarek, specialized in the experimental and theoretical response of light modulators from Southampton University, and the group of Thomas Heiser specialized in devices made of organic semiconducting materials, from Strasbourg University. A UK-French PhD program, jointly managed by DGA and DSTL, funded this work.

3 State of the art

The numbers of photoconductors and LCs available on the market are high, so is the number of possible combinations of both objects to design an OASLM. In this section, we will focus on state of the art photoconductors. We can classify them into three categories: Bulk inorganic crystals, inorganic thin films and organic thin films. Several parameters are important such as the spectral sensitivity, the transparency/reflectivity, the spatial resolution, the working frequency, the response time and the fabrication method, which influences the device cost.

The required specifications depend on the focused application. As an example, for the design of a light valve that acts as an optical shutter to protect for instance human eyes from high light intensity, it is most necessary to use transparent photoconductors with a sufficiently high response time, whereas the spatial resolution is not very important. However, if the goal is to design an OASLM for telecom applications that widely use wavelengths around 1500 nm, the transparency in the visible is not as important as the transparency and photosensitivity in the Infrared (IR) region. If the objective is to encrypt an image as a function of LC modulation in holographic applications, the spatial resolution is most important. For a display device, the resolution is limited by the pixel size and is defined by the following equation:

$$Spatial\ resolution\ (lp.mm^{-1}) = \frac{1000\ (\mu m/mm)}{2 \times pixel\ size\ (\mu m)}$$

The perfect photoconductor does not exist. There are pros and cons for each semiconductor technology, as illustrated in this chapter.

3.1 Bulk Semiconductor Crystals

Modern semiconducting technologies mainly rely on monocrystalline substrates made of Silicon or III-V compounds. The common trait of these semiconductors is that they have been manufactured using a crystal growth method, the

Czochralski process [33] being the most frequently used technique. The thickness of such commercial wafers is around hundreds of micrometres and the wafer size limits the maximum device area. To my knowledge, the main advantage of this class of materials is the perfect control of most electrical and optical parameters achieved after decades of research, which facilitates the conception of an OASLM. Even the defects within the bandgap are well defined. These defects are important to define the spectral sensitivity of crystalline photoconductors, as they permit sub-bandgap absorptions. One of the best known crystalline defects used in OASLMs is the native defect level known as EL2 in Gallium arsenide (GaAs) [39] [40]. It permits to design infrared sensitive OASLMs.

3.1.1 Semi-Insulating GaAs (SI GaAs)

In the specific application of fiber optics sensors, the attenuation of the optical signal is lowest around 1500 nm. Therefore, it is necessary to choose a photoconductor sensitive to telecom wavelengths. IR sensitive GaAs photoconductors have been recently used to design an OASLM which serves as holographic medium in an adaptive interferometer based on two-beam coupling [13], [24] and is to be used in conjunction with optical fiber technology. The working principle is as follows: a linearly polarized continuous-wave fiber laser beam ($\lambda = 1.55$ μm) is divided into two optical paths, forming the reference and signal wave of the interferometer. The two waves recombine on the OASLM. Along the "signal arm", a calibrated phase modulator induces a small phase shift that induces a phase grating inside the OASLM, which in turn diffracts incident light. By measuring the intensity of the diffracted orders with a photodiode, it is possible to measure small phase shift differences between the reference and the signal fiber. For some applications, the phase difference may be induced by the modulation of the signal fiber length. It can for instance, be applied to probe mechanical deformations induced by sound waves or by mechanical stress. Figure 13 schematizes the adaptive interferometer in which the OASLM is the recombining medium.

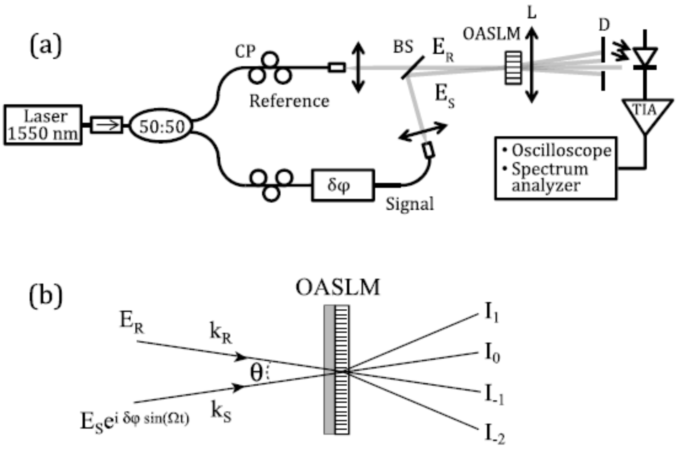

Figure 13: (a) Adaptive interferometer setup: a 1.55 µm laser source is split into two paths, reference and signal, and then recombined on the OASLM. A calibrated phase modulator is inserted in the signal arm. BS, beam splitter; D, diaphragm; L, far-field lens (400 mm focal length); PC, polarization controller; TIA, transimpedance amplifier. (b) Two-beam coupling process occurring in the OASLM. Reproduced from [13]

Even though the light modulation has been demonstrated at a wavelength of 1.55 µm, the very high charge carrier mobility of this semiconductor, around 5000 $cm^2/(V.s)$, limits the spatial resolution to hundreds of microns (around 5 $lp.mm^{-1}$) due to lateral charge diffusion [32]. Improving the spatial resolution would permit the integration of OASLM in systems that are more compact. However, for non-holographic applications, the spatial resolution is less important. Moreover, it is often more interesting to use visibly transparent semiconductors (i.e. with a wide band-gap) such as silicon carbide (SiC).

3.1.2 Silicon carbide (SiC)

Silicon carbide is well-known for its polymorphism [41], which is the ability of a crystalline material to exist in more than one crystal structure. It is a complex material, due to the wide variety of polytypes, which give rise to different bandgap energies [42]. SiC bandgap varies in a broad energy range, from 2.4 to 3.3 eV. It is correlated to the material crystalline lattice structure, as illustrated Figure 14.

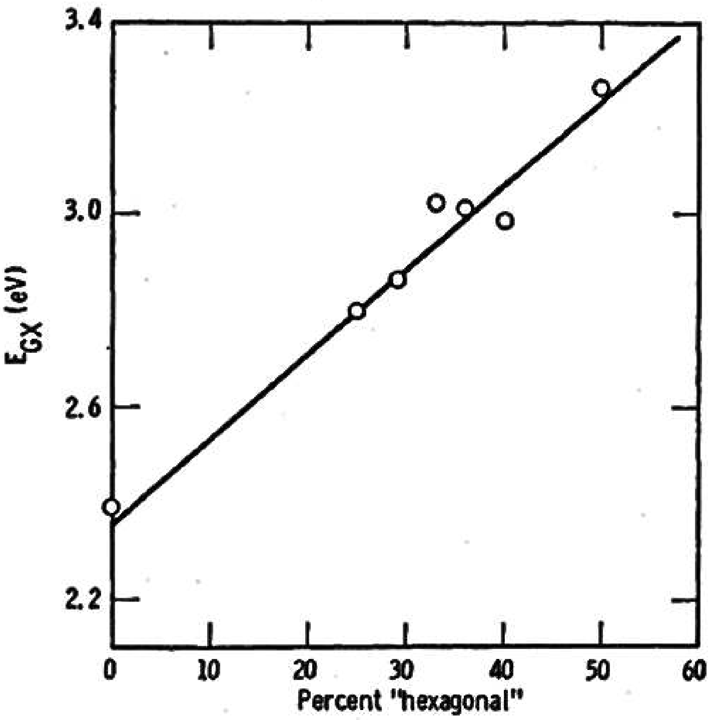

Figure 14: The bandgap energies of seven SiC polytypes, namely 3C (Cubic 2.390 eV), 8H (2.80 eV), 21R (2.86 eV), 15R (2.986 eV), 33R (3.01 eV), 6H (3.023 eV) and 4H (3.263 eV), as a function of the hexagonality, reproduced from [42]. The indicated line was only drawn as a guide to the eye.

Vanadium is known to create both a deep donor level and a deep acceptor level in 4H [43] and 6H [44] [45] SiC crystals, with the deep donor level located below the deep acceptor. It has therefore the unique capability to compensate residual dopants in order to confer semi-insulating properties to both p-type and n-type SiC, whatever polytype 4H or 6H. The position of the acceptor and donor levels for these two polytypes as a function of different crystal growth techniques has been the subject of many scientific papers and is summarized in reference [46].

4H or 6H SiC polytypes wide band-gap photoconductors are transparent in the visible spectrum, while the presence of Vanadium related deep levels enhances its spectral sensitivity in the visible and IR range [47], [48]. The charge carrier concentration is generally very low at room temperature [44], [45] which makes V-doped SiC an ideal candidate for applications as optical limiters. The V-SiC photoconductor has been used to design a liquid crystal light valve in order to protect devices or human eyes from high-intensity light source [23] [49]. Figure

15 depicts the operation of such devices with the LC being in a twisted nematic configuration.

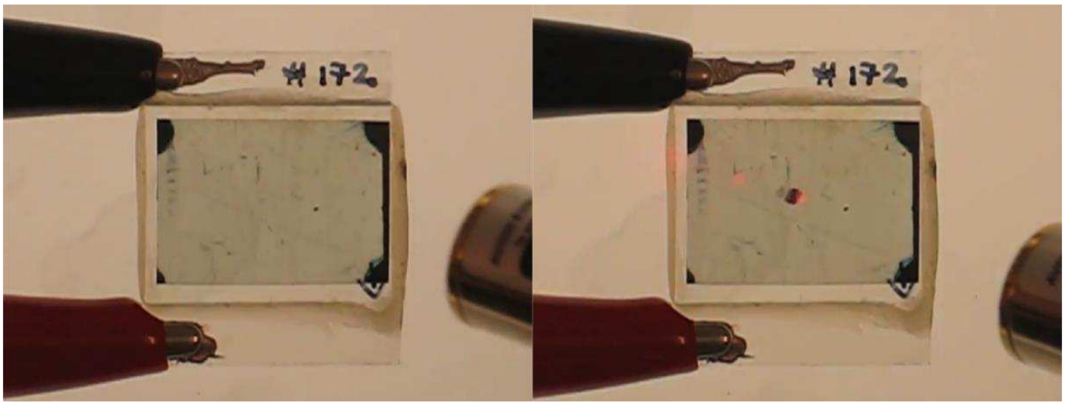

Figure 15: Operation of a transparent optically addressed light valve. The cell is in the twisted nematic configuration, located in-between a polarized light source and a polarizer, an external electric field is applied to the ITO/glass sheet. When the red laser is on, the impedance locally diminishes and the LC reorient rendering the illuminated area opaque (right). The video is available online on Ploughshare Innovations YouTube channel. Ploughshare Innovations is the UK government's technology transfer organisation.

3.1.3 Photorefractive crystals

Another photoconductor known as Bismuth Silicon Oxide (BSO) has particularly interesting optical properties (see reference [23]). It has been shown to be optically active, causing a wavelength-dependent rotation of linearly polarized light passing through the crystal medium. BSO belongs to the class of photorefractive semiconducting crystals. Upon illumination, the local refractive index of a photorefractive medium is modified. Consequently, the light ray self-modifies its propagation conditions in the medium. Photorefractive crystals, when used in conjunction with liquid crystals, can lead to novel properties. Lithium Niobate ($LiNbO_3$) is another photorefractive material used as light modulation medium in Microchannel Spatial Light Modulator (MSLM) [20].

3.1.4 Lithium niobate ($LiNbO_3$), a "photovoltaic substrate"

$LiNbO_3$ has been recently used as "photovoltaic substrates" for liquid crystal cells [50] [51]. $LiNbO_3$ is a trigonal crystal system, which lacks inversion symmetry and is known for its nonlinear optical polarizability, and for its so-called abnormal "bulk photovoltaic effect" [52]. In non-centrosymmetric crystals, such as $LiNbO_3$, the probabilities for electron photo-excitation, electron scattering or relaxation are anisotropic. Consequently, a photocurrent may arise under illumination and build up space charge. Such photocurrents are sometimes called "photogalvanic" currents to differentiate them from the usual photovoltaic effect. In addition, the electric field changes the refractive index of photorefractive $LiNbO_3$.

In iron doped $LiNbO_3$ ($LiNbO_3$:Fe) the bulk photovoltaic effect is significantly enhanced due to the presence of two valence states of the iron dopant: Fe^{2+} (donor ions) and Fe^{3+} (acceptor ions) [53]. Upon illumination, the excited charges follow a statistically favourable direction of motion. Therefore, the orientation is critical to obtain an electric field in the desired direction. $LiNbO_3$ substrates are cut in the Z direction (C-plane). Upon illumination, it gives rise to an electric field that is perpendicular to the substrate plane as depicted Figure 16.

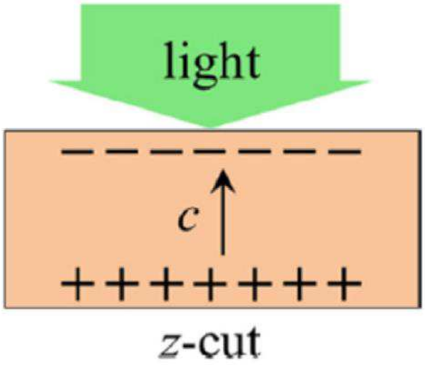

Figure 16: Light-induced charge separation in z-cut $LiNbO_3$ crystals, reproduced from [54]

A hybridized LC cell arrangement utilizing the bulk photovoltaic field and consisting of a LC layer comprised between two $LiNbO_3$:Fe substrates was initially proposed by Carns in 2006 [50]. When illuminated, the bulk photovoltaic effect in each substrate creates an internal electric field between the two substrates that is sufficient to reorient the LC molecules. No external electrical field is required, as illustrated in Figure 17.

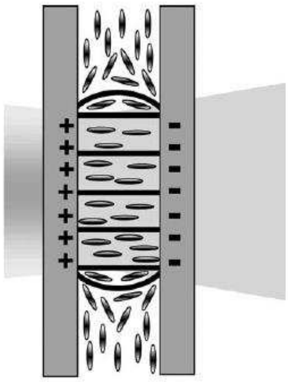

Figure 17: Principle of a voltage free LC light valve using two LiNbO$_3$:Fe substrates cut in the C-plane, reproduced from [50]

Such devices display a transient response of several seconds, which depends on the illumination time. The possibility to optically generate a static electric field, avoids the need for electrical contacts, wires and power generators, rendering the device more compact. Therefore, LiNbO$_3$ is a promising material for all-optical devices and has been suggested to be integrated in optofluidic systems, where a high degree of compactness is required [55]. However, the concept still needs to be demonstrated in practical applications.

To conclude, bulk semiconductor technology is a vast topic that has been for decades the focus of intense research, triggering its application to OASLM devices. However, they generally suffer from low resolution (some tenth of lp.mm^{-1}) and high production costs (due for instance to high-temperature processing). In addition, the crystal size is hard to control and impedes the development of large area devices.

3.2 Inorganic thin films

Unlike the previous bulk crystalline materials, inorganic thin films do often lack long-range structural order. Wide varieties of deposition methods are available to deposit inorganic thin films: from the utilization of a gaseous precursor to wet deposition techniques. The material process parameters strongly affect the resulting semiconducting properties and often lead to lower electronic performances. However, these materials can be processed at a lower temperature, allowing deposition on plastic substrates and making them compatible with roll-to-roll processing techniques. The latter has a great impact on the production costs. Inorganic semiconducting nanoparticles, such as ZnO, can be processed from solution, while amorphous silicon (a-Si) can be deposited over large areas by Plasma-Enhanced Chemical Vapor Deposition (PECVD).

3.2.1 Amorphous hydrogenated silicon

Hydrogenated amorphous silicon, a-Si:H was first fabricated by Chittick using a silane gas (SiH_4) precursor [56], a hazardous gas that has already caused explosions in photovoltaic fabrication plants [57].

Despite these technical issues, amorphous silicon possesses a major advantage compared to crystalline silicon as the photoconductive material for OASLM. The charge carrier mobility is three orders of magnitude lower [58] than its crystalline counterpart, improving the OASLM spatial resolution [32]. However, despite thinner films, the strong extinction coefficients of a-Si:H (direct bandgap material) [59] limits its use to reflexion mode structures. OASLMs based on a-Si:H thin films were first proposed by Ashley and Davis in 1987 [60]. To address the OASLM they use the reflection mode proposed by Grinberg in 1975 [61] schematize in Figure 18. In this configuration, a write light is used to address the photoconductor, which spatially modulates the LC layer. The LC spatial modulation is probed by the read-light (labelled as projection light in Figure 18) which is spatially modulated by the light pattern induced by the writing light. The dielectric mirror and the blocking layer separate the photoconductor from the read-out light.

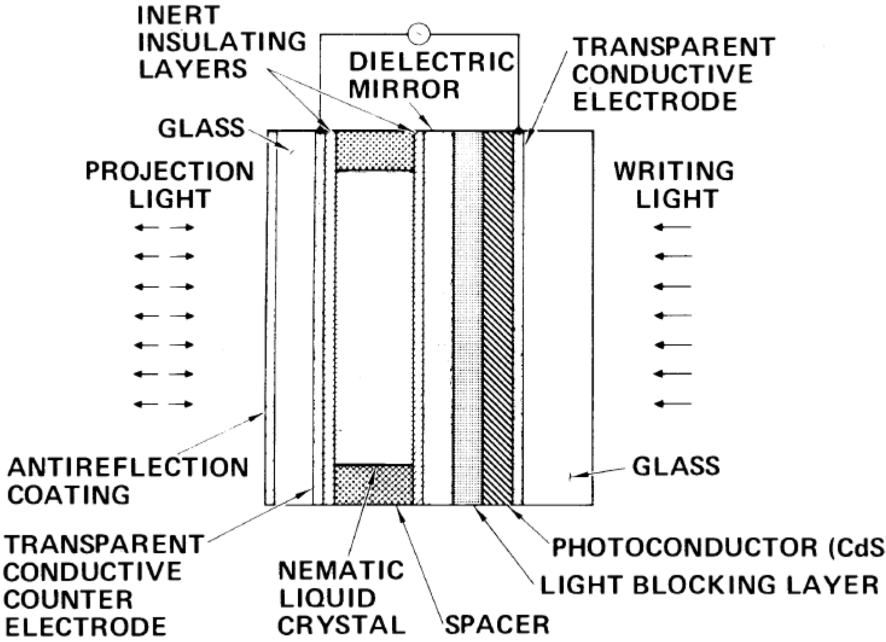

Figure 18:Schematic of the reflective LC light valve reproduced from [61]

Such devices were commercially available and are known as “Parallel Aligned nematic Liquid crystal – Spatial Light Modulator” (PAL-SLM, Hamamatsu Photonics [62]). The spatial resolution achieved with an a-Si:H photoconductor has been rapidly increased, from 40 lp/mm in 1989 [19], to 175 lp/mm in 1991 [63] (measured diffraction efficiency (DE, see chapter 6.3.5) of 0.01%) and attained 370 lp/mm in 1999 (DE of 8%). Note that in the last case the photoconductor was a carbon-doped a-Si:H.

The low resolution of OASLMs based on inorganic crystalline photoconductors was thus greatly improved by the use of their amorphous counterpart. On the other hand, the fabrication process of such layers is more hazardous and security measures need to be taken, increasing the fabrication costs. Moreover, a-Si:H OASLMs are limited to the reflexion mode, and can therefore not been used as optical limiting filter.

3.2.2 Zinc Oxide (ZnO)

Zinc oxide (ZnO) is a semiconductor known for its wide bandgap energy of around 3.35 eV [64]. It is generally n-type due to the presence of oxygen vacancies or zinc interstitials [65]. Several deposition techniques can be used to grow ZnO thin films on a variety of substrates [66]. The electrical and optical properties of ZnO films make them highly suitable for applications both in civilian and military areas, such as the fabrication of acoustic- and electro-optical devices [67]. In 2008 a UV photodetector exhibiting high resistivity (> 1 TΩ) with a responsivity of 61 A/W has been demonstrated [68]. Moreover, a solution processing method was used to deposit a colloidal suspension of ZnO nanoparticles (ZnO NPs). Such deposition methods are compatible with large area devices. Naturally, a transparent semiconductor that displays high resistivity and good responsivity is an ideal photoconductive material to design a UV sensitive transparent light valve.

The first OASLM using ZnO as photoconductor was developed by White & Feldman in 1970 [69], this device reached a resolution of 5 lp/mm. In a more recent work (2015) ZnO NPs have been used successfully in OASLM devices and allowed to achieve a resolution of 825 lp/mm (DE of 0.05%). However, the device worked only at low frequencies (0.2 Hz) and operated at high AC voltages (around 6V). To the best of my knowledge, no further application has been developed with OASLMs based on ZnO photoconductors.

3.3 Organic thin films

Another class of semiconducting materials displays advantages similar to ZnO, namely, organic semiconductors. They can also be processed from solution and have been historically used as xerographic photoreceptors [37]. This class of materials displays a wide variety of forms and shapes: crystalline, semi-crystalline and amorphous, bulk or thin films. Thermal sublimation or wet deposition methods can be used to form thin films. Like the previous class of materials, their electronic properties are strongly affected by the processing conditions. For instance, the structure and morphology of the polymer film can be modified through chain alignment by mechanical rubbing [70]. In particular, the charge carrier mobility can vary over orders of magnitude [71] depending on the processing conditions. This offers the possibility to design OASLM with different properties. A priori using a low mobility material should increase the OASLM spatial resolution at the expense of slower response time, while higher mobilities may be more suitable for fast response devices.

The chemical structure of these molecules (given in the appendix) determines their energy bandgap. The latter varies for instance from 3.5 eV [72] for PVK down to 1.9 eV [73] for P3HT. Sub-bandgap absorption is not well defined for most polymer materials and blends, except for P3HT [74] and MDMO-PPV [75] blended with PCBM. These photoconductive materials offer a wide range of possibilities to design novel organic OASLMs. However, to date, only PVK blended with either TNF or C_{60} have been used as photoconductive material in OASLMs. The use of bilayer films rather than blends, composed in particular of a phtalocyanine (H_2Pc) layer and a C_{60} layer, were foreseen by Collings [76] in 2004 as a possible novel organic photoconductor for OASLMs. Unfortunately, no OASLM devices based on such bilayers have been reported so far, limiting this overview of organic photoconductors to PVK blends.

3.3.1 PVK doped with TNF or C_{60}

The term doping [37] was historically introduced to describe PVK:TNF or PVK:C_{60} composite materials. However, because this term inherently indicates that the dopant concentration is orders of magnitude lower than the host material, and taking into account the rather large molar ratio of the “dopant” (i.e. TNF or C_{60}) generally used, we prefer to use the term “blend” or “bulk heterojunction” in this manuscript. In the seventies, PVK was one of the most studied conducting polymers. A lot of attention was put on charge transport. It is for instance well established today that the electron and hole mobilities are field dependent and vary with the addition of TNF [77] as shown Figure 19.

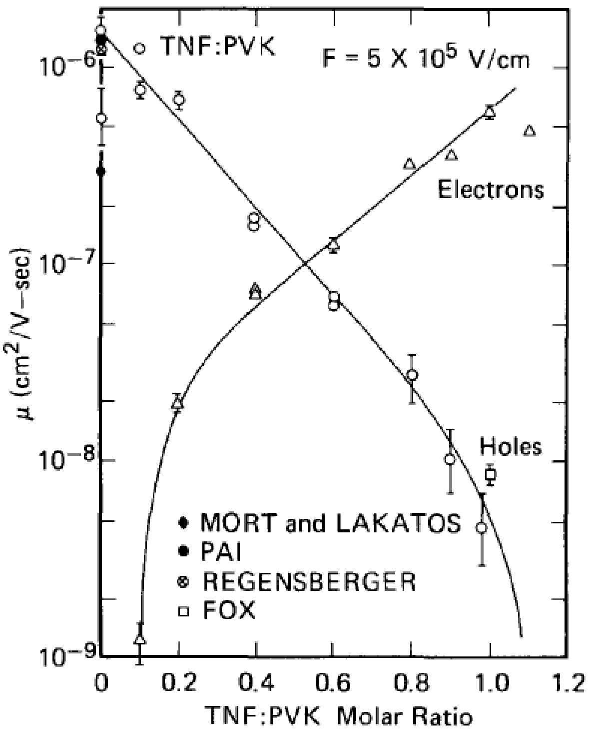

Figure 19: Variation of hole and electron drift mobility with TNF:PVK molar ratio, reproduced from [77] at an electric field of $5 \times 10^5\ V/cm$.

PVK blended with TNF or fullerenes [78] were popular for their good photoconducting properties and for a large amount of data available on its physical properties. Naturally, this material was seen as an ideal candidate to exploit its properties as a photoconductor in OASLMs. Furthermore, its wide bandgap and its potential low-cost production were considered to open the possibility to replace inorganic V:SiC photoconductors in larger area optical limiters.

In 1997, H. Ono et al. reported the first utilisation of PVK:TNF as an organic photoconductor in an OASLM device. A resolution of 83 lp.mm-1 [79] under a DC field of 200 V could be demonstrated. Later on, Kaczmarek et al. used PVK:C_{60} as the photoconductor and monitored the LC cell threshold DC voltage shift as a function of light intensity. In addition, a resolution as high as 143 lp.mm-1 [16] could be obtained. In 2008, Yao succeeded to attain a resolution as high as 527 lp.mm-1 [80] (DE of 0.015) with a PVK:C_{60} photoconductor.

More recently, Proctor et al. [38] extracted the electrical parameters of PVK:C_{60} LC light valves using a standard LC cell model [81]. Through an experimental method known as Voltage Transfer Function (VTF) (see section 4.3.2) [82], they extracted the threshold voltage of the light valve as a function of light intensity and frequency of the applied AC voltage (Figure 20).

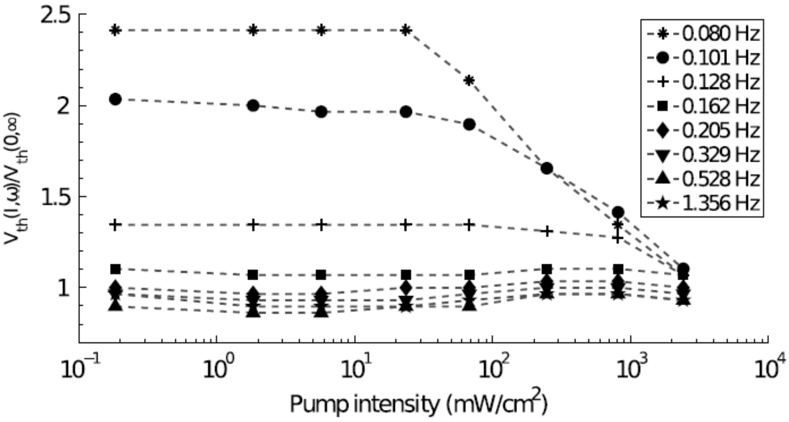

Figure 20: Frederiks transition as a function of frequency for different light illumination levels for an E7 cell. Reproduced from [38].

They showed that the conductivity of LC was a critical parameter to observe a light modulation. Whereas higher conductivity LC exhibited a LC modulation with varying light intensity, low conductivity LC revealed a weaker response. Therefore, the performances of PVK:C_{60} OASLMs are dependent on the LC electrical parameters. In addition, the best performances were attained at quasi-static frequencies (below 1 Hz).

Under quasi-static frequency conditions, the molecules are able to follow the slow variation of the electric field. Therefore, a twisted nematic cell will "blink" and pass from its dark to its transparent state with the same frequency. Such behaviour is inconvenient if the aimed application is a light valve that should act as an optical shutter. It is possible in principle to use a DC voltage (instead of an AC voltage) to avoid the "blinking" and characterize the performances of those devices as a light valve. However, a DC voltage leads to ionic accumulation at the photoconductor/LC interface, which may damage the LC cell and reduce its long-term stability.

3.4 Conclusion

The ideal photoconductor does not exist. However, thanks to decades of research in semiconducting materials, numerous photoconductors are worth considering. They can be sensitive to IR wavelengths such as GaAs at the expense of low resolution or visibly transparent such as V:SiC. No external electric field is needed for substrates such as Fe:LiNbO3, thanks to the bulk photovoltaic effect. Less costly OASLMs with a good resolution such as a-Si:H can be made. Finally materials such as ZnO and PVK:C_{60} display very high resolution at the expense of speed. In this thesis we chose to start working with a P3HT:PCBM blend, which has better charge carrier mobilities than PVK:C_{60} blends and is well documented (it has long been the "reference" material for the development of organic photovoltaic devices). The question, whether there will be a place for P3HT:PCBM among all these different materials, remains open.

4 Methods & materials

4.1 Materials

This chapter introduces the organic materials used in the course of my thesis.

4.1.1 P3HT

P3HT, or poly(3-hexylthiophene-2,5-diyl), is one of the most studied semiconducting electron donor (D) polymers. It has been used in many devices such as solar cells (OSCs), organic light-emitting diodes (OLEDs) and organic field-effect transistors (OFETs). The chemical structure of P3HT is shown in Figure 21.

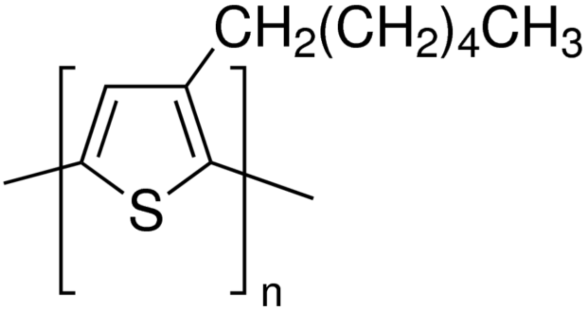

Figure 21: Chemical structure of poly(3-hexylthiophene-2,5-diyl)

It has a bandgap of 1.9 eV and absorbs a large portion of the visible spectrum. It will therefore render the OASLM more opaque when compared to the almost transparent PVK:C_{60} devices. Although this photosensitive semiconductor might not be the best final polymer choice for our application, it is a good starting point due to its good solubility, film-forming properties and commercial availability. The scientific community also has a good general knowledge of its physical properties.

4.1.2 $PC_{61}BM$

The other semiconducting material that we used to form our photosensitive layer is a soluble fullerene derivative: PC61BM or Phenyl-C61-butyric acid methyl ester (see Figure 22). It is one of the most widely used electron acceptor material (A) in organic solar cells. P3HT and PCBM have an appropriate offset in their energy levels, which permit excitons to be separated into free charge carriers at the D/A interface.

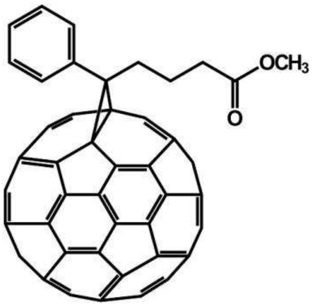

Figure 22: Chemical structure of Phenyl-C61-butyric acid methyl ester

4.1.3 PEDOT:PSS

It is a mixture composed of Poly-(3,4-ethylenedioxythiophene) or PEDOT and polystyrene sulfonic acid (or PSS). A fraction of its sulphur atoms is protonated (carries a positive charge) in the presence of strong acids. PSS is negatively charged and a fraction of the sulfonate groups SO3$^-$ carries a sodium ion, which acts as a counterion reservoir for the positively charged PEDOT.

PEDOT:PSS is a mixed ionic/electronic conductor, as PEDOT and PSS are responsible for respectively electronic and ionic conductivity [83].

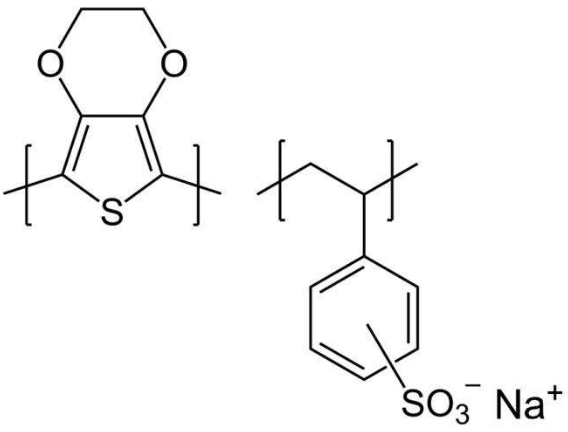

Figure 23: Chemical structure of PEDOT (left) and PSS (right)

Taken separately, each material has its interests for various applications: PEDOT, for instance, is the predominant counter electrode in aluminium and tantalum polymer capacitors [84], [85]. PSS can be used as an ion exchange resin in fuel cells or in medicine to treat Hyperkalemia [86], an excess of potassium in blood serum. PSS affinity is greater for potassium ions than sodium ions. Therefore, the excess potassium in the body is absorbed by the PSS resin, which releases its sodium ions. Later on, PSS is excreted by the organism. PSS allows the formation of a stable, easy to process dispersion of PEDOT:PSS mixture in aqueous solution.

Due to its unique properties, the PEDOT:PSS mixture has found numerous applications: antistatic coating, photographic films, interfacial layer... Furthermore, if organic compounds, like high boiling point solvents such as DMSO or surfactants are added, its conductivity increases by several orders of magnitude [85]. Therefore, this material is one of the best candidates to replace ITO in touchscreens, LCD, OLED, OSC... It is also used in organic electrochemical transistors (OECT) [87], electrochromic switching devices [88], bioelectronics [89] and in addition, it can be used as a planar alignment layer for LCDs [90]. Finally, it is commonly used as a hole transport layer in most optoelectronic devices.

4.1.4 PEIE

The work function at the surface of electrodes can be shifted due to unwanted contamination [91]. The changes of the WF value can be induced by a chemical reaction (chemisorption), such as the oxidation of an aluminium surface [92]. A molecule can also bind to the surface of a material via van der Waals forces (physisorption), like atomic adsorption of hydrogen on platinum, which leads to a WF decrease of the metal surface [93]. In both cases, a surface dipole is created inducing a vacuum level shift, which modifies the interface properties.

Polyethylenimine-ethoxylated (PEIE) is a non-conjugated polymer electrolyte that contains amine groups as depicted in Figure 24. This insulating compound is used as a surface modifier. Physisorbed PEIE on an electrode surface results in a decrease of the WF [94]. Therefore, thin PEIE layers (<10 nm) are often used as cathode interfacial material to permit electron extraction in photovoltaic cells [95].

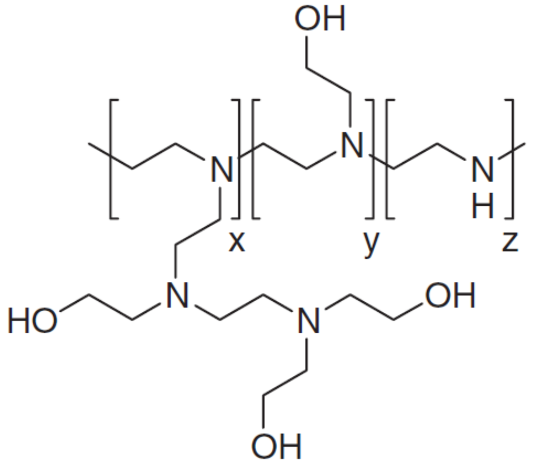

Figure 24: Chemical structure of PEIE

4.1.5 E7

In this thesis, we use the commercially available E7 nematic liquid crystal mixture, which contains cyanobiphenyls and cyanoterphenols components. The mixture molecular composition is shown in Figure 25. E7 displays high birefringence and a positive dielectric anisotropy ($\Delta\varepsilon > 0$).

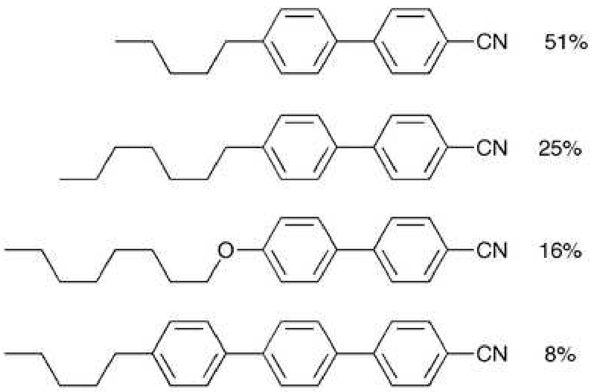

Figure 25: Composition of E7 mixture with from top to bottom 4-cyano-4'-n-pentyl-biphenly (5CB), 4-cyano-4'-n-heptyl-biphenyl (7CB), 4-cyano-4'-n-oxyoctyl-biphenyl (8OCB), 4-cyano-4''-n-pentyl-terphenyl (5CT).

Generally, the LC supplier provides the most important LC parameters. The values corresponding to the E7 commercialized by Instec are given in Table 1.

LC	$\varepsilon_{\|\|}$	$\varepsilon_{\perp}$	K_1 (pN)	K_3 (pN)	n_e	n_o	T_{IN} (°C)	T_{NC} (°C)
E7	19	5.2	11.55	19.1	1.746	1.521	60.5	-20

Table 1: Technical specifications of Instec's E7, $\varepsilon_{||}$ and $\varepsilon_{\perp}$ are the dielectric constant relative to the LC orientation. γ_1 is the rotational viscosity coefficient, K_1 and K_3 are respectively the splay and bend elastic constant, n_e and n_o are the extraordinary and ordinary refractive index of the material, finally T_{IN} and T_{NC} indicate the temperature range where the material is in its nematic phase.

The threshold voltage (V_{TH}) for the field-induced mechanical deformation in E7 is given by [96]:

$$V_{TH} = \pi \sqrt{\frac{K_1}{\varepsilon_0 \Delta\varepsilon}} = 0.97\ V$$

The threshold voltage has no dependence on the thickness of the cell.

All LC parameters are strongly influenced by external factors. For example, the birefringence $\Delta n = n_e - n_o$, varies as a function of wavelength and temperature. The manufacturing process may also affect the LC parameter. The rubbing process, for instance, may introduce dust particles. Additionally, the layers in contact with the LC material, such as the glue used to seal the cell and the interfacial layers might be the cause of ionic contamination.

4.2 Organic OASLM Fabrication

In this paragraph, the manufacturing process of organic OASLM devices that I set up at the beginning of my PhD project will be described. The general structure of an OASLM is recalled in Figure 26. The LC is comprised between two ITO glass slides and calibrated spacers are used to maintain a uniform cell gap. One of the ITO glass slides is coated with an alignment layer (AL). The second ITO glass slide is coated with a stack composed of a first optional interfacial layer (OIL_1), a photoconductive layer (PCL) and a second optional interfacial layer (OIL_2).

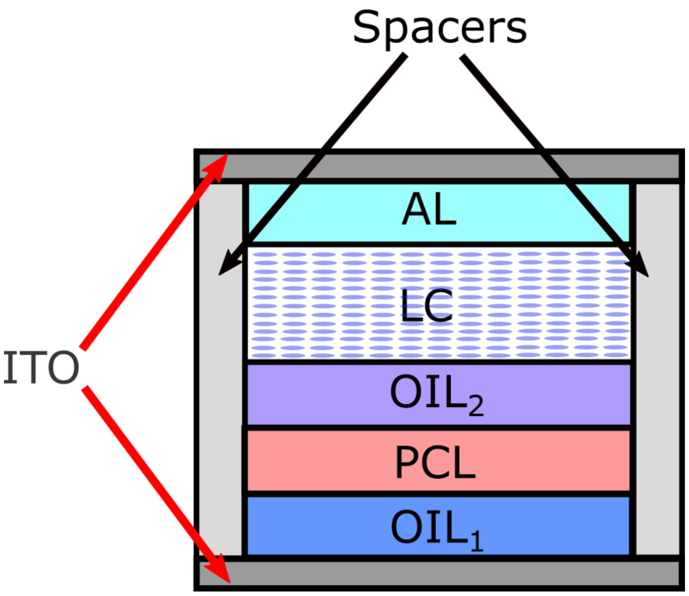

Figure 26: Structure of an OASLM with an organic photosensitive layer

Commercially available ITO substrates with the following specifications were purchased from Lumtec:

The sheet resistance is between 9 and 15 Ω/sq. The average roughness is Ra<6nm and the maximum roughness depth is R_{max}<35nm. The ITO transparency is >84% at 550 nm. The polished soda lime glass substrate surface is 20x20 mm with a thickness of 1.1 mm. Moreover, a thin (>20 nm) SiO2 barrier layer is located between the glass substrate and the ITO thin film in order to minimize diffusion of alkali-oxides from the soda lime glass into the photoconductor and liquid crystal.

To remove dust and contaminants that might be present on the ITO substrate surface, the samples are cleaned in an ultrasonic bath in the following order: acetone, distilled water and isopropyl alcohol for 15 minutes each. A subsequent UV Ozone treatment was made to ensure the removal of organic contaminants and increase the surface wettability.

After the cleaning procedure, organic films are spin-coated on top of the ITO substrates. A thin PEDOT:PSS (30 nm) alignment layer (AL) was deposited on the first ITO substrate in air and annealed at 140°C for 10 minutes in a glove box under a nitrogen atmosphere.

On the second substrate, for some devices, an OIL_1 has been deposited prior to the P3HT:PCBM layer (see chapter 7). The WF of ITO can be modified by spin-coating a PEIE solution (polyethylenimine, 80% ethoxylated solution, 35-40 wt. % in H2O, average Mw = 70000, purchased from Sigma-Aldrich) that has been further diluted with 2-methoxyethanol (with a weight ratio of 0.6% also purchased from Sigma-Aldrich). The PEIE solution was spin-coated onto the ITO coated glass slide in ambient conditions, transferred to a glovebox with an inert nitrogen atmosphere (<1 ppm 02 and H20), and dried for 10 min at 100°C.

The P3HT:PCBM PCL was deposited in a nitrogen atmosphere to avoid air-contamination and minimize photo-oxidation of the organic materials. It was annealed for 10 minutes at 140°C to remove residual solvents and improve the blend morphology (more ordered semi-crystalline P3HT and better-defined D and A domains).

For some devices, an additional OIL2 has been deposited on top of the PCL (see chapter 7). A thin layer of PEDOT:PSS (Clevios CPP 105 D, Heraeus) can be spin-coated on top of the photoactive layer in ambient atmosphere, transferred to a glovebox with an inert nitrogen atmosphere (<1 ppm 02 and H20), and dried for 5 min at 120°C.

Finally, the rubbing technique described in section 2.2 was used to brush superficially the layers in order to permit the alignment of the liquid crystal molecules. The layer sequence that was deposited depends on the device structure.

After thin film deposition, two ITO substrates with appropriate layer sequences were assembled together using a UV curable adhesive mixed with SiO2 microspheres. The resulting gap between the substrates is equal to the diameter of the SiO_2 beads (7.75 μm). The LC material is introduced into the gap by capillarity. Finally, the edges of the cells were sealed using a 2-component epoxy adhesive or a UV curable adhesive. For the latter case, the LC cell active area must be covered with a protective sheet to avoid damages induced by UV light during glue curing.

4.3 Characterization methods

In this section, I will present the measurement methods that I have set-up in the laboratory. The other techniques that I used will be described in the appendix.

I first installed a workbench dedicated to the optoelectronic characterizations of OASLM devices. It allows me to measure simultaneously and in the same environment, the cross-polarized intensity (CPI), the voltage transfer function (VTF) and the electrical impedance of the devices. Various LabVIEW programs had to be written to control the measurement setup.

In parallel, I also carried out a study of the photoconductivity of organic materials using metal/semiconductor/metal devices.

4.3.1 Cross Polarized Intensity (CPI)

CPI [97] is a technique used to measure the birefringence of a LC cell at a discrete wavelength and as a function of AC voltage. As explained in part 2.2.1, when a monochromatic polarized light travels through a birefringent medium, the phase velocity of each light component differs, creating a phase difference that depends on the LC birefringence.

The set-up is composed of a laser source, a polarizer, an analyser, a photodiode and a transimpedance amplifier (TIA). The sample is placed between the polarizer and the analyser (see Figure 27). The TIA voltage output is monitored by an oscilloscope. A voltage generator is used to drive the LC cell.

When the polarizer is tilted by 45° with respect to the LC alignment direction, the total phase shift (δ) between both light components at the output of the LC cell is given by:

$$\delta = \frac{2\pi d \Delta n}{\lambda}$$

where d the cell thickness, Δn the birefringence and λ the light wavelength. As δ changes (for instance because Δn decreases), the polarisation state at the LC cell output is modified. Consequently, the light intensity measured by the photodiode varies between zero, when the field is perpendicular to the analyser main axes, to a maximum value, when both directions are aligned.

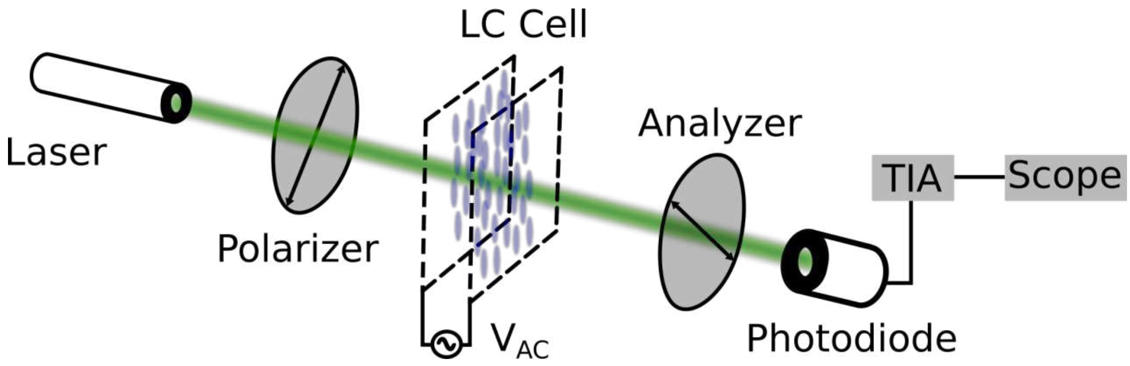

Figure 27: CPI experimental setup

As explained in chapter 2.2, when the voltage drop across the LC layer is superior to the Fréedericksz threshold value (V_{TH}), the birefringence diminishes, and so does the phase difference δ. Measuring the transmitted light intensity as a function of voltage permits us to estimate the phase difference or the change in birefringence, as indicated in Figure 28.

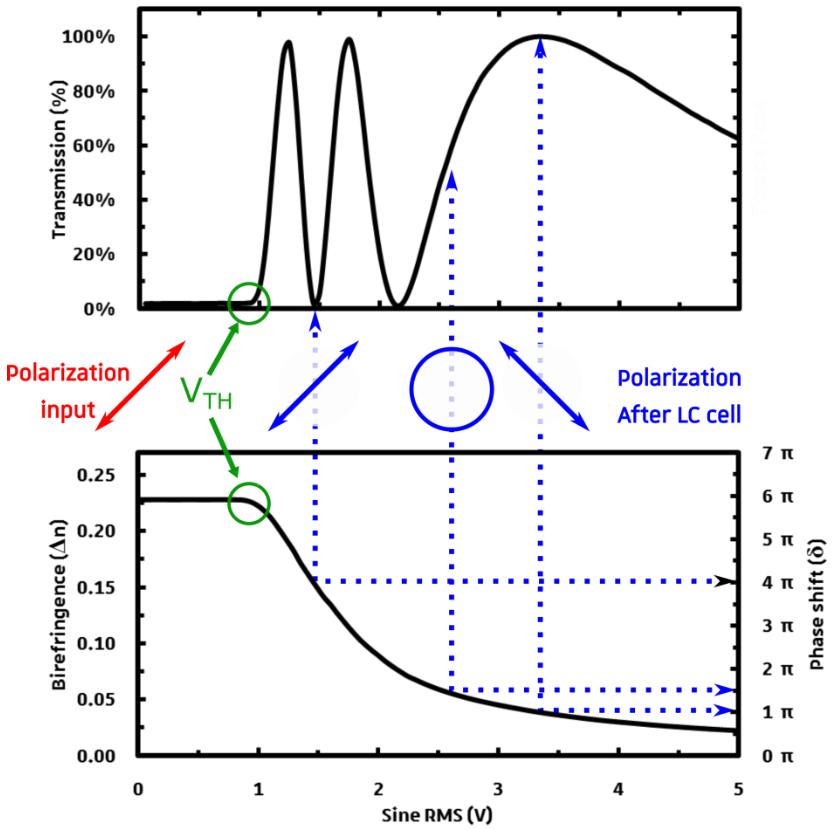

Figure 28: On top, experimental data of CPI experiment are shown. The associated phase shift and birefringence (bottom) can be determined from the light intensity versus voltage curves. Some specific polarization states are drawn and are related to their phase shift values by blue arrows. The LC used is E7 and PEDOT:PSS is used as an alignment layer. The measured cell gap is d = 6.7 µm, λ = 532 nm and the applied frequency is 1 kHz.

It should be noted that the pretilt angle affects the LC cell maximum phase shift. Assuming the same pretilt angle on both substrates, the phase shift decreases with increasing pretilt values (see Figure 29) according to the following equation [97]:

$$\delta = \frac{2\pi d \Delta n}{\lambda} \times cos^2 \theta$$

where θ is the angle formed between the substrate and the LC molecules.

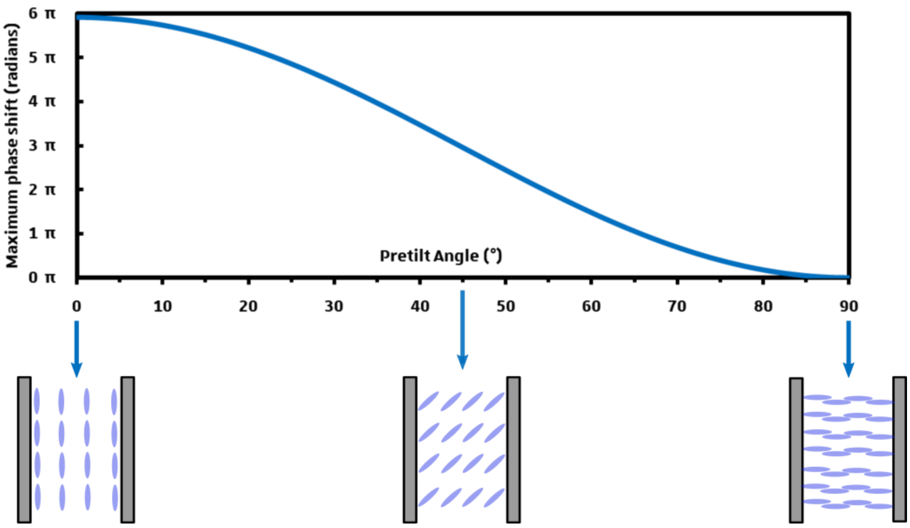

Figure 29: Maximum phase shift versus the LC pretilt angle

A high pretilt angle does not only affect the LC cell optical properties. It also affects its response time [98] and the threshold voltage. For instance, Hsu et al. [99] used a photocurable prepolymer to control the pretilt angle of a LC cell. Their results are shown Figure 30. They used a 3 μm thick LC cell coated with anti-parallel rubbed polyimide and filled with E7. A He-Ne laser (λ = 632.8 nm) was used to measure the CPI curves as a function of photocurable prepolymer concentration (NOA 65). It is important to notice that despite the fact that we use the same LC (E7), the number of peaks at the maximum and minimum transmission for the low pre-tilt sample is lower than the case shown in Figure 28. In this example, the gap of the LC cell is thinner and the wavelength used to measure the optical response is higher, consequently, the total phase shift decreases.

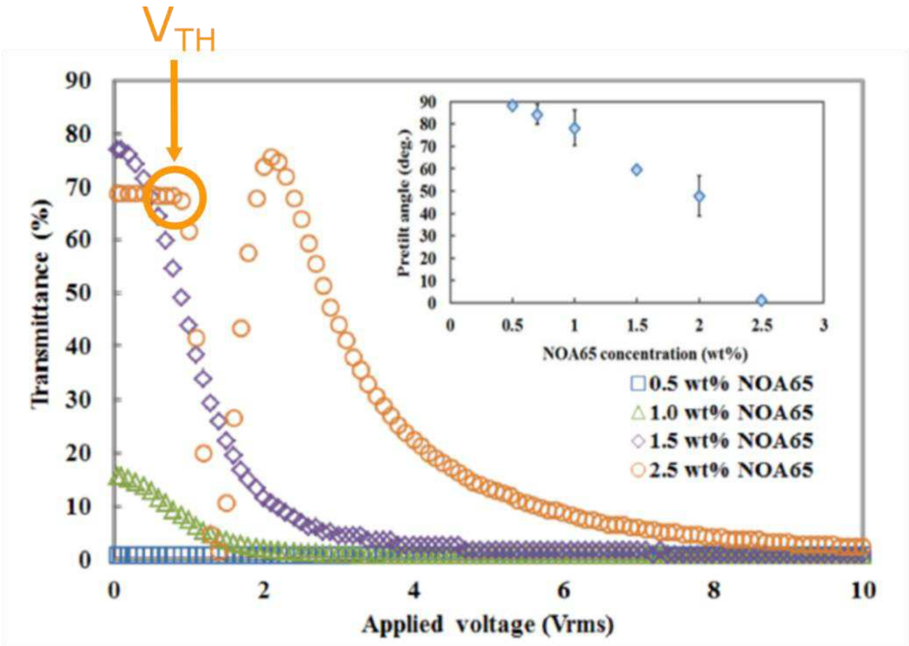

Figure 30: Measured CPI curves as a function of NOA65 concentrations. Inset: Pretilt angle formed by the LC molecules with the substrate as a function of NOA65 concentrations. Reproduced from [99].

The cell with the lowest pretilt (0° orange circle) angle shows a threshold voltage around 1V. With increasing pretilt angle, the maximum measurable phase shift diminishes. It decreases the number of maxima and minima between the different CPI curves. In addition, the threshold voltage around 1V is inexistent when the pretilt angle is large (>50°). Therefore, CPI measurements allow a straightforward estimate of the LC pretilt angle by measuring the threshold voltage value.

The LC cell response depends strongly on the driving frequency. For instance, if the signal frequency is low enough (1 Hz), the liquid crystal molecules will be able to follow the slow variations of the electric field as shown in Figure 31.

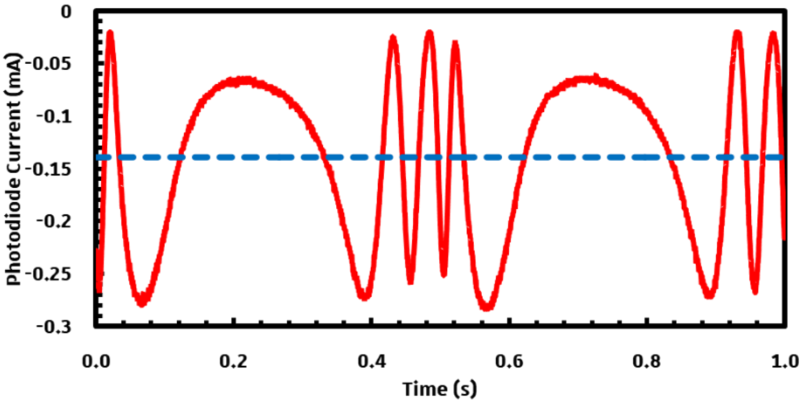

Figure 31: The LC cell is driven by an AC voltage of 10 V_{pp} at a frequency of 1 Hz. The LC molecules follow the slow variations of electric field, which are monitored by the photodiode as a function of time (red line). The blue line represents the signal recorded by the photodiode averaged over one period of time.

On the other hand, at a higher frequency (1 kHz), the LC molecules are not fast enough to follow the fast variations of the electric field. The optical response as displayed Figure 32 depends then mostly on the root mean square (RMS) value of the applied voltage.

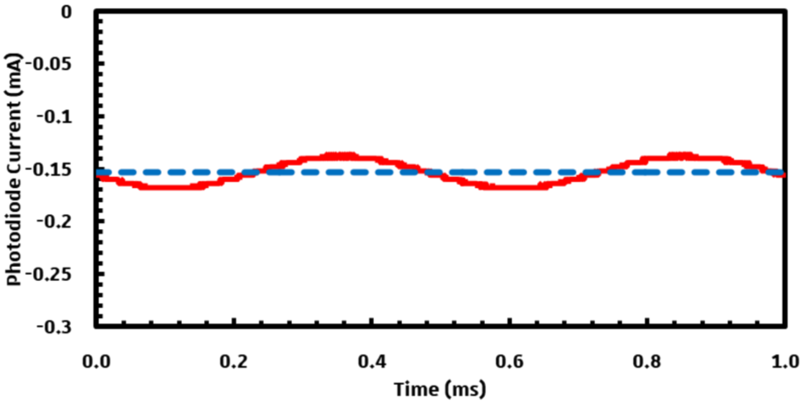

Figure 32: The LC cell is driven by an AC voltage of 10 Vpp at a frequency of 1 kHz. The LC molecules cannot follow the variations of the electric field, which are monitored by the photodiode as a function of time (red line). The blue line represents the signal recorded by the photodiode averaged over one period of time.

Regardless of the measurement frequency, the CPI curves always display the intensity of the photodiode, averaged over several periods (corresponds to the blue lines in Figure 31 and Figure 32) of the LC cell driving voltage, as a function of the applied voltage RMS. The liquid crystal motions due to frequency variations are not represented in the CPI curves

This leads us to interesting questions. What is the effect of the driving frequency on our LC cell? What information can we extract from these measurements? To assess these questions, a measurement technique based on CPI measurements called Voltage Transfer Function (VTF), which was initially developed at Southampton [82], has been set up in Strasbourg.

4.3.2 Voltage Transfer Function (VTF)

VTF is a convenient and graphical method to determine the electrical behaviour of liquid crystal cells from optical measurements. It has been used by Proctor et al. [38] to estimate the voltage drop variation across the LC layer as a function of light intensity on a PVK:C60 based OASLM.

In order to obtain the VTF data, several CPI measurements are made over a certain range of frequency and are plotted on a 3D graph. A measurement example is shown Figure 33. For this example, PEDOT:PSS was used as AL on both sides and no photoconductive layer was present. A colour code is used to depict the intensity values of the light transmitted for different frequencies (horizontal axis) and applied voltages (vertical axis).

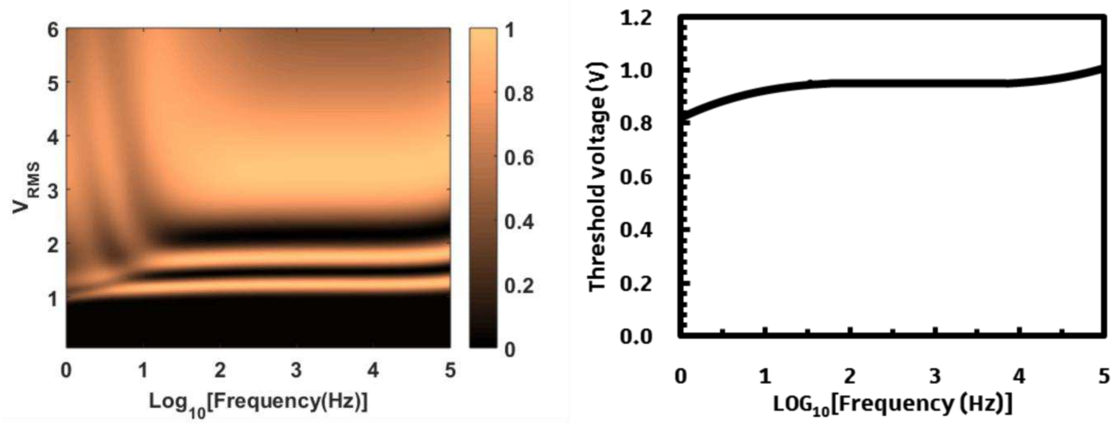

Figure 33: VTF curve (left) and threshold voltage value as a function of frequency (right.). PEDOT:PSS is used as an AL and λ = 532 nm.

The variation of the LC cell threshold voltage is shown in Figure 33.

A linear equivalent electrical circuit model depicted in Figure 34 can be used to extract quantitative information from VTF measurement data [81]. The model consists of an association in series of several impedances, each impedance characterizing the electrical properties of a given layer. The impedance Z_{ITO} of ITO can be considered as purely resistive while the impedances Z_{LC} , Z_{AL} and Z_{PCL} of respectively the LC layer (LC), the alignment layer (AL) and the photoconductive layer (PCL) behave like parallel RC-circuits.

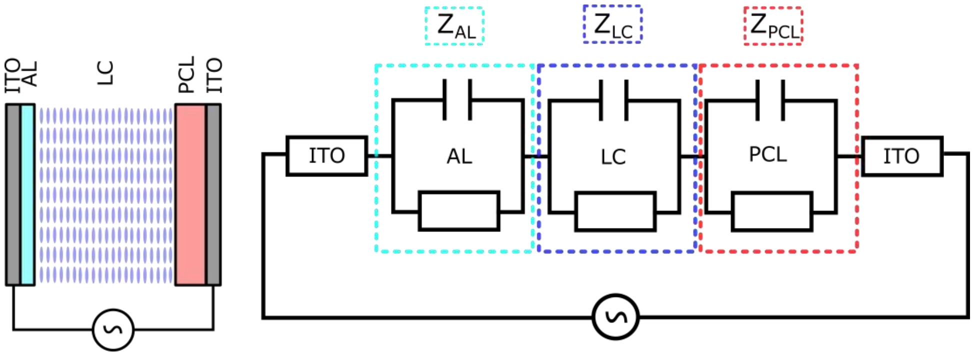

Figure 34: Electrical circuit of an OASLM (left) and its equivalent circuit (right). The Liquid crystal (LC) is comprised between two ITO glass slides (ITO), one of the ITO side is coated with a thin insulating layer generally polyimide which serves as an alignment layer (AL), while the other is coated with the photoconductive layer (PCL).

We can distinguish three parts on the curve in Figure 33. The high-frequency part, above $\text{Log}_{10}(f) = 4$ (10 kHz), shows an increase of the threshold voltage. At these frequencies, our model can be reduced to a simple low-pass filter circuit, with $Z_{ITO} = R_{ITO}$, $Z_{LC} = C_{LC} = \frac{1}{jC\omega}$. The potential drop across the LC is equivalent to $V_{LC} = \frac{Z_{LC}}{Z_R+Z_{LC}}$. With increasing frequency, the impedance of the liquid crystal layer decreases and more and more potential is dropped across the resistive part of the circuit. Therefore, the threshold voltage increases with the frequency.

At lower frequencies, between $\text{Log}_{10}(f) = 1.5$ (32 Hz) and $\text{Log}_{10}(f) = 4$ (10 kHz), the threshold voltage is constant. This point out that most of the potential drop occurs across the LC layer because Z_{AL} is dominated by the AL resistance. Moreover, below $\text{Log}_{10}(f) = 1.5$ (32 Hz), the threshold voltage decreases because the LC does not respond to RMS voltage but to the peak voltage, as stated in section 4.3.1.

The low-frequency behaviour would have been different if we had used an insulating Polyimide (PI) instead of a conductive polymer PEDOT:PSS as an alignment layer (see Figure 35).

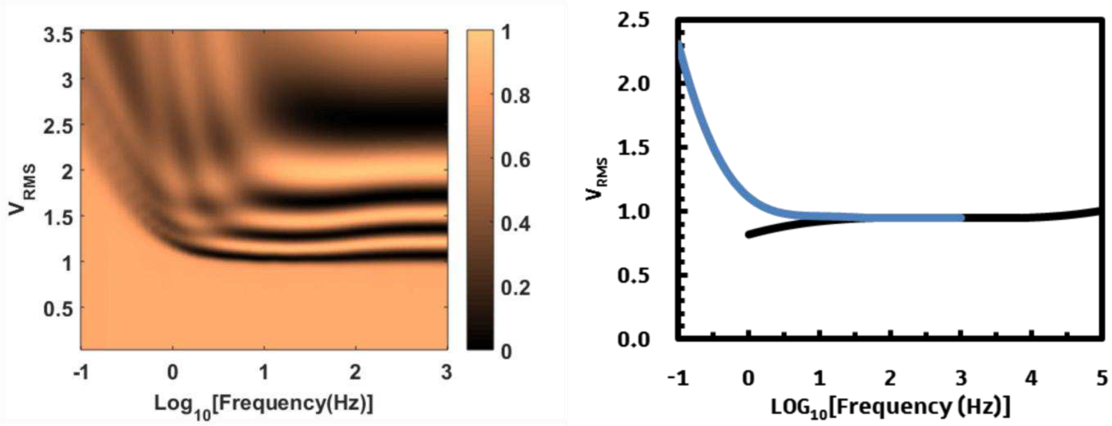

Figure 35: VTF curve (left) and threshold voltage value as a function of frequency (right) of a LC cell using PI as AL. The blue curve represents the PI cell and the dark curve the PEDOT:PSS cell.

The difference is most pronounced at low frequencies because the purely capacitive PI layer impedance gets higher than the impedance of the LC. Therefore, the threshold voltage increases rapidly. At higher frequencies, the threshold voltage value decreases to the same value as for the device with PEDOT:PSS as the alignment layer. As we can see from these two examples, the response of our liquid crystal cell is dependent on the electrical parameters of each element constituting the cell. The device response depends on the different layers thicknesses [81], resistivity and temperature [100].

The frequency range of our experiment is limited. At very low frequency, the acquisition time can be excessively long. For example, at 0.01 Hz, it would take 100 s to record each data point, which is prohibitive. In addition, if the frequency and intensity of the electric field applied to the LC cell are too high, the molecular dipoles in constant rotation disperse energy in the form of heat. This phenomenon, known as dielectric heating, has been reported in the literature. In the case of a LC cell, the temperature can rise by a few tenths of degrees [101]. This effect would induce “artefacts” on the VTF curve mainly due to temperature induced birefringence variation.

4.3.3 Impedance spectroscopy (IS)

Impedance spectroscopy can be used as a complementary method, to model the electrical behaviour of the LC cells. I used this technique to measure the impedance versus frequency of different physical systems, mainly photoconductors and liquid crystal cells, in order to build up equivalent electrical models.

This method relies on applying a small sinusoidal signal at different frequencies to the device under test and measuring the current. The current response is defined by two parameters: the phase lag or phase difference φ and its magnitude I_0. The impedance Z of the system is defined by:

$$Z(t) = \frac{E_t}{I_t} = \frac{E_0 \sin(\omega t)}{I_0 \sin(\omega t + \varphi)} = Z_0 \frac{\sin(\omega t)}{\sin(\omega t + \varphi)}$$

The impedance is generally represented as a complex number:

$$Z(\omega) = Z_0 e^{i\varphi} = Z_0(\cos\varphi + i \sin\varphi)$$

$Z(\omega)$ consists of a real part $Z_R = Z_0 \cos\varphi$ and an imaginary part $Z_{Im} = Z_0 \sin\varphi$. The real part, also known as the resistance R and the imaginary part is the reactance X. This notation is used to trace the “Nyquist plot”, with R plotted on the horizontal axis and X plotted on the vertical axis.

Generally, the simplified model of a LC cell with or without photoconductor is a sum of RC circuits in series with a resistance Rs (see Figure 34). The Nyquist plots for two exemplary circuits are displayed in Figure 36 and Figure 37. The Nyquist plot of an RC circuit is represented by a semicircle.

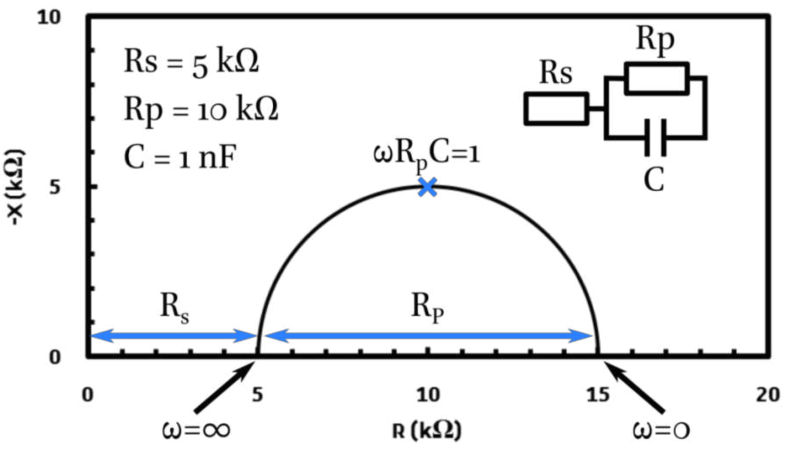

Figure 36: Nyquist plot of an R-RC circuit.

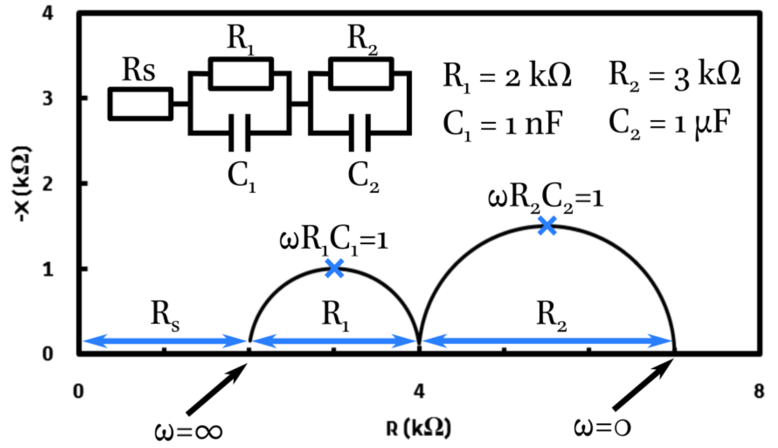

Figure 37: Nyquist plot of an R-RC-RC circuit.

Several points of interest are shown on the curves. At low frequency (ω = 0), the system response is purely resistive, so its impedance is equal to the sum of each resistor. At very high frequency (ω = ∞), the capacitor impedance tends to zero. They "short-circuit" the corresponding RC impedance, making the total impedance equal to the series resistor Rs. Finally, each time constant corresponds, for each semicircle, to the frequency at which the absolute value of the reactance is maximal.

IS measurements are quicker and give more detailed and accurate information than VTF. The drawbacks of IS is that you lose the optical information (pretilt angle, birefringence value…) and that the AC driving voltage is generally lower than the driving voltage of an LC cell. The maximum sinusoidal voltage available with the HP 4192A LF Impedance Analyzer that I used is 1.1 VRMS, which is not enough to drive a LC cell made of E7 whose Fredericksz threshold value is 0.97 V.

5 Electro-optic response of LC cell

It is not straightforward to decrypt the results from CPI or VTF measurements of an OASLM as a function of light intensity. The electro-optical response of OASLMs devices is complex and varies as a function of light intensity and applied voltage. Obviously, the photoconductive layer impedance should vary as a function of light intensity, but the liquid crystal impedance may also vary as a function of applied voltage due to its anisotropic behaviour. As an example, for a device with an E7 LC mixture in an initially planar orientation, the long axis of the LC molecules is aligned parallel to the substrate and its relative dielectric constant is equal to $\varepsilon_{\perp} = 5.2$. With increasing voltage, the LC molecules reorient along the electric field direction, increasing the relative dielectric constant up to the value of $\varepsilon_{||} = 19$, when the long axis of the LC molecules is perpendicular to the substrate. It implies that the LC impedance decreases with increased applied voltage.

The goal of this section is to illustrate, through VTF measurements, the consequence of an impedance (capacitor or resistor) put in series with the LC layer. This will give us some insight to recognize the different behaviours that may occur when a photoconductor, whose impedance varies under illumination, is used in the LC device. We will monitor the LC cell electro-optical response either with or without a series impedance as a function of frequency using the VTF method. The passive component placed in series with the LC device can be seen as the impedance change that would be induced by a photoconductive layer when the light intensity is decreased. Finally, we will estimate the changes that could be induced by a thin P3HT:PCBM layer under illumination.

5.1 IS measurement of the LC cell

The impedance value added in series with the LC cell should be high enough to lead to a measurable variation between two VTF curves (with and without series impedance), and low enough to avoid that the large potential drop decreases the electric field in the LC below the threshold value (the molecules would not reorient). I therefore first measured the LC cell impedance (without additional series impedance) within a frequency range of 10 Hz to 100 kHz at 100 mV_{RMS}, well below the Fréedericksz transition, using an impedance analyzer. The measurement results and the corresponding theoretical curves and equivalent electrical model are shown in Figure 38. The LC cell had the following structure: glass/ITO/PEDOT:PSS(30 nm)/LC (6.7µm)/PEDOT:PSS (30 nm)/ITO/glass

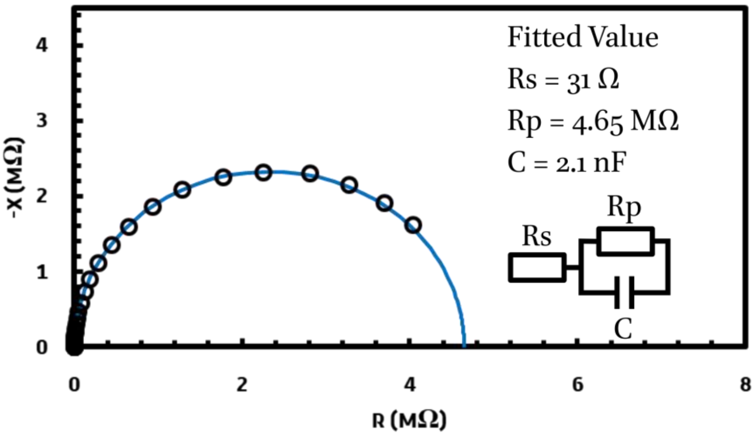

Figure 38: Nyquist plot of the experimental (black circle) and fitted data of a E7 filled liquid crystal cell using PEDOT:PSS as AL.

We can recognize that the LC cell behaves like a parallel RC circuit with a very small series resistance as expected considering the very small impedance of the highly conductive ITO and the two thin (30 nm) PEDOT:PSS layers. In the investigated frequency range, the series resistance is negligible in comparison to the LC impedance (Z_{LC}). The latter is defined by:

$$|Z_{LC}| = \frac{1}{\sqrt{\left(\frac{1}{R_p}\right)^2 + (\omega C)^2}}$$

In the low-frequency region, Z_{LC} is equal to R_P and equals $\frac{1}{\omega C}$ in the high-frequency region. Z_{LC} is plotted as a function of frequency on Figure 39. The impedance value of Rp (blue dot) and C (red dot) are also plotted on the graph.

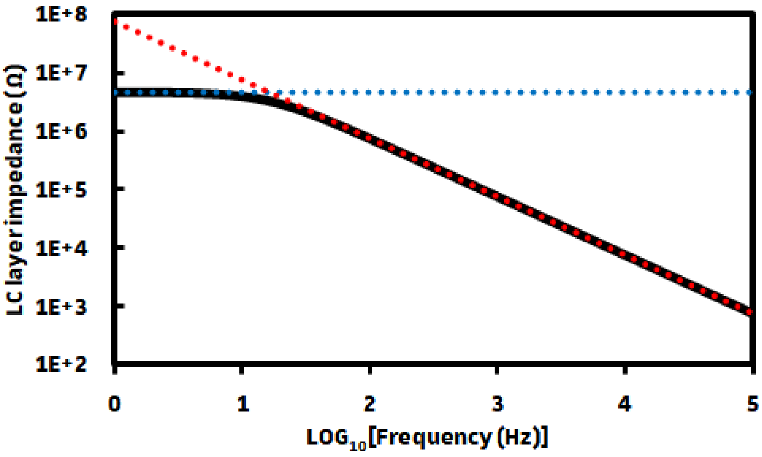

Figure 39: LC layer impedance (dark line) plotted versus frequency. The impedance value of Rp (blue dot) and C (red dot) are also plotted on the graph.

At high frequency, Z_{LC} is almost purely capacitive. Therefore, the device acts as a low pass filter with a cutoff frequency defined by:

$$f_c = \frac{1}{2\pi R_s C}$$

If an additional series resistance (R_a) of 5.11 kΩ is introduced, the cutoff frequency will decrease down to 15 kHz (≈ 4.2 in LOG_{10} scale). The potential drop across the series resistor increases with increasing frequency. Consequently, the voltage across the LC cell is attenuated. The voltage attenuation factor (A) decreases with increasing frequency according to the following equation:

$$A = \frac{1}{\sqrt{1 + ((R_a + R_s)\omega C)^2}}$$

Therefore, the threshold voltage of the LC cell will increase accordingly with increasing frequency. Figure 40 depicts the voltage attenuation across the LC layer (red line) and the threshold voltage value (blue line) as a function of frequency.

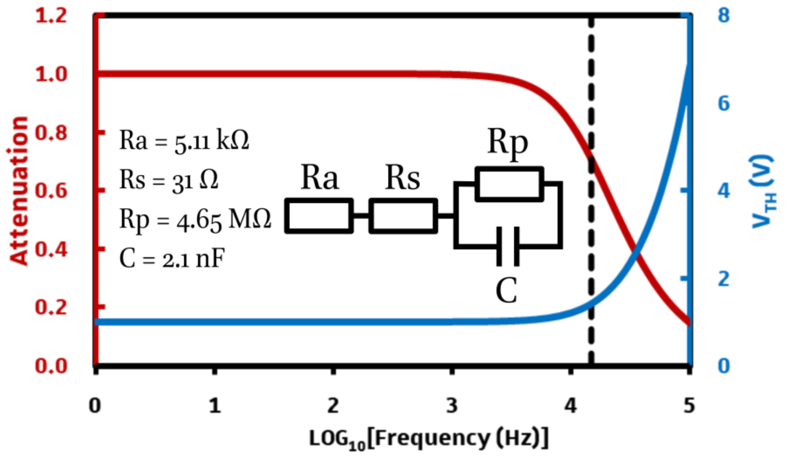

Figure 40: Voltage attenuation across the LC layer (red line, left red axis) and threshold voltage value as a function of frequency (blue line, right blue axis) induced by a series resistor (Ra). The cutoff frequency is also shown (dashed dark line)

According to the LC cell electrical model, a series resistance of 5.11 kΩ induces a sufficient voltage drop to be monitored via the VTF method.

A similar reasoning can be used to choose the capacitor value. In the frequency domain where the LC layer acts as a capacitor (above 10 Hz), we can neglect Rs and Rp. The LC cell electrical model reduces to a single capacitor (C = 2.1 nF). If we add an additional capacitor in series (Cs), the circuit will act as a voltage divider with two capacitors in series. The attenuation induced by the additional capacitor is given by the following formula:

$$\frac{V_{LC}}{V_{app}} = A = \frac{C_s}{C_s + C}$$

with V_{LC} the voltage drop across the LC layer, V_{app} the voltage applied, A the attenuation factor, C_s and C_{LC} the series and liquid crystal capacitance value. By choosing a capacitance value of 4.72 nF, the attenuation induced by the capacitor in series will be equal to 0.69, if the voltage RMS is below the threshold for LC reorientation, as shown in Figure 41.

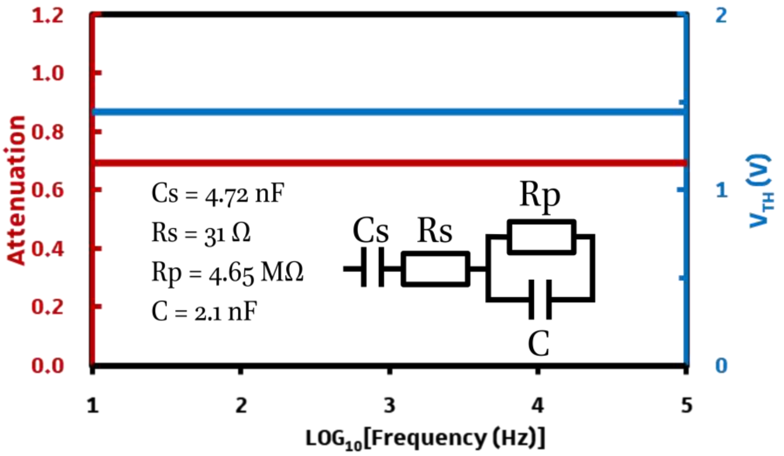

Figure 41: Voltage attenuation across the LC layer (red line, left red axis) and threshold voltage value as a function of frequency (blue line, right blue axis) induced by a series capacitor (Cs) of 4.72 nF.

By measuring the changes in the VTF response induced by either the 5.11 kΩ resistor (Ra) or the 4.72 nF capacitor (Cs), it is possible to investigate the variation of the LC impedance with applied voltage, and the screening of quasi-static electric field by ion accumulation.

5.2 Impact of series impedance on a LC cell electro-optic response

5.2.1 Series resistance

Figure 42 displays two VTF measurements showing the electro-optic response of a LC cell with and without the series resistor R_a. The frequency was varied from 1 Hz to 100 kHz (respectively 1 and 5 on the Log_{10} horizontal axis). The applied voltage varies from 0 to 6 V_{RMS}. The transmitted light intensity is coded by a grey colour code, dark for low intensity and white for high intensity.

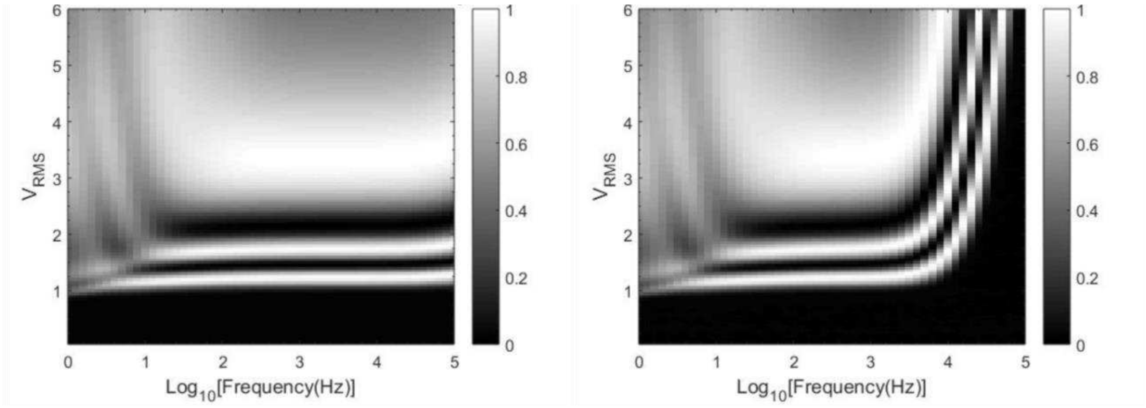

Figure 42: Experimental VTF graphs of a LC cell filled with E7 using PEDOT:PSS as alignment layer with(right) and without(left) a series resistance of 5.11 kΩ.

We do observe that, in the presence of R_a, the threshold voltage value increases with frequency, pointing out that the LC cell acts as a low pass filter. Therefore, for an OASLM device, which includes a photoconductor with a purely resistive behaviour, we should observe a similar trend with varying light intensity.

We can also estimate the capacitance of the LC cell from these graphs by measuring the attenuation induced by the series resistor. The latter is given by the following equation:

$$\frac{V_{LC_1}}{V_{LC_2}} = A = \left|\frac{Z_{C_{LC}}}{Z_{C_{LC}} + Z_{R_{eq}}}\right|, above\ 100\ Hz\text{:}\ Z_{C_{LC}} \approx \frac{1}{jC_{LC}\omega}$$

$$C_{LC} = \frac{\sqrt{1 - A^2}}{A \times (R_{eq}) \times 2\pi \times f}$$

with A being the attenuation induced by the series resistor R_a, it correspond to the ratio between V_{LC_1}, the voltage applied to the LC device which is assumed to be entirely dropped across the LC layer and V_{LC_2} the voltage applied to the LC device in series with the resistor R_a.

V_{LC_1} and V_{LC_2}correspond to the Fréedericksz transition measured with and without a series resistor, respectively. R_{eq} is the equivalent series resistance, i.e. the sum of the ITO resistance R_s and R_a.

Below $\mathrm{Log}_{10}(f) = 3.6$ (4 kHz), the potential is mostly dropped across the LC cell (since $R_{eq} << Z_{CLC}$). Above 3.6 (4 kHz), the potential drop induced by R_{eq} cannot be neglected anymore. The threshold voltage values between the two VTF curves are different above this frequency. Therefore, we can use the equation in this frequency region to estimate the capacitance value of the LC cell as a function of frequency, as depicted in Figure 43. The capacitance value extracted from the VTF measurement (red circle) is in good agreement with the value obtained from fitting the IS curve (dashed red line) as long as the attenuation induced is high enough to be measured accurately.

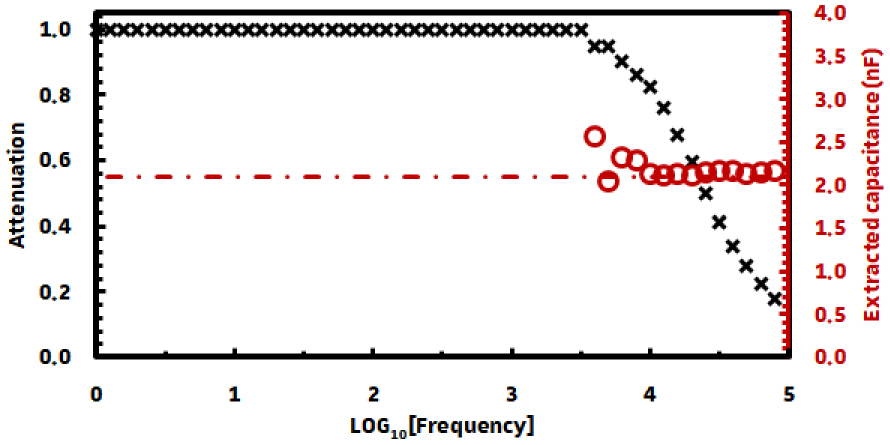

Figure 43: Attenuation dark cross (left axis), extracted capacitance red circle and fitted value by IS measurement dashed red line (right axis).

It is interesting to point out that the LC cell electro-optical response is unaffected by the series resistance as long as we work at an appropriate frequency. If for example we wanted to operate our LC cell at 1 kHz, a larger Rs value would be tolerated. In other words, the ITO thickness could be reduced, increasing the sheet resistance and the device transparency and decreasing the costs. Moreover a less conductive material such as PEDOT:PSS may be used instead of ITO. Such considerations are important for device transparency optimization or industrial applications.

5.2.1.1 Impact of LC dielectric anisotropy

Another interesting point to consider is the effective value of the LC layer capacitance. The latter may indeed depend on the applied voltage because of the LC dielectric anisotropy. What is the impact on the LC impedance when the LC molecules reorient? From the above measurements, we are tempted to conclude that the attenuation induced by the resistor is negligible at frequencies below 4 kHz and that the threshold voltage is constant and unaffected by the series resistor. However, a closer look at the CPI curves issued from both VTF measurements at a fixed frequency of $Log_{10}(f) = 3.5$ (3162 Hz) and depicted in Figure 44 reveals the opposite. The red line corresponds to the LC cell in series with R_a whereas the dark line to the LC cell has been obtained without R_a. While the threshold voltage is constant, both curves differ significantly at higher voltages.

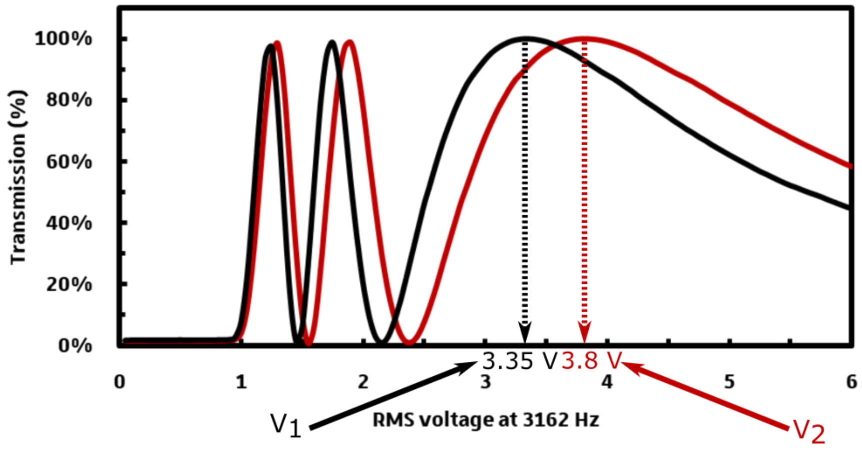

Figure 44: CPI measurement extracted from the VTF curves (Figure 42). With a series resistance of 5.11 kΩ (red line) and without (dark line)

From the voltage shift (red and dark arrows on Figure 44), we can deduce the attenuation induced by R_a with increasing voltages. The voltage applied by the function generator (V_1) equals the potential difference across the LC cell without R_a (V_{LC}). Adding R_a in series induces a shift of the CPI curves. One needs to apply a higher voltage V_{GENE2} to the LC cell with R_a (V_{LC}) to obtain the same retardation (LC orientation or Δn). The voltage across the LC cell is therefore attenuated, and the attenuation between both curves is defined as:

$$A = \frac{V_{LC}}{V_2} = \left|\frac{Z_{LC}}{Z_{R_a} + Z_{LC}}\right| \; and \; V_1 \approx V_{LC}, therefore:$$

$$A = \frac{V_1}{V_2}$$

This attenuation allows us to calculate the capacitance of the LC cell as a function of the applied voltage depicted in Figure 45. If we assume that the capacitance is proportional to the LC dielectric constant, Figure 45 traces the change in dielectric constant induced by the reorientation of the LC molecules. However, the spacers mixed with the glue in contact with the ITO induce a parallel parasitic capacitance that adds to the LC capacitance and cannot be neglected. In other words, we are measuring the capacitance of the LC layer in parallel with the spacer capacitance and not the liquid crystal capacitance. However, using a patterned ITO glass layer would fix this issue.

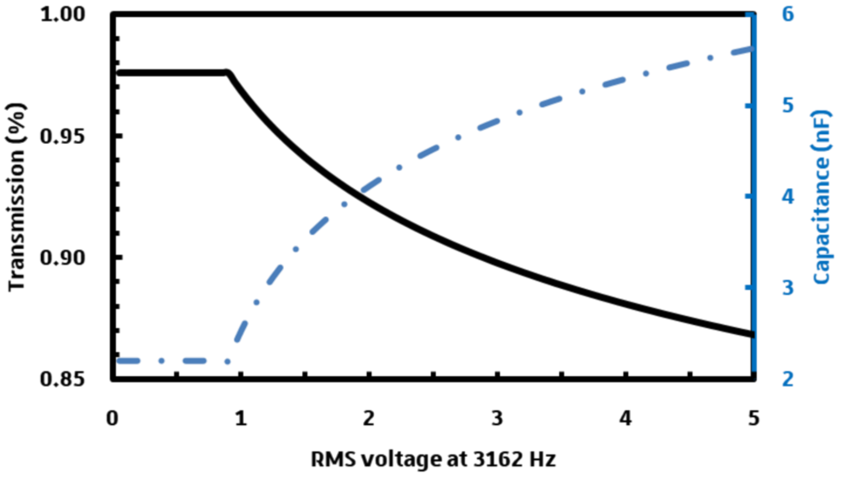

Figure 45: Attenuation induced by the series resistor at a frequency of 3162 Hz as a function of applied RMS voltage (Dark line, left axis) and calculated capacitance (blue dashed line, right axis)

The above results allow us to conclude that the change in LC dielectric constant under electric field produces a non-negligible voltage drop at high-applied voltages. This effect will be useful to understand the light-induced voltage shift in the presence of a photoconductive layer.

5.2.2 Series capacitor impact

The behaviour of the liquid crystal with an additional capacitor put in series with the LC cell is displayed in Figure 46. We can observe two different regimes. In the low-frequency region (below 10 Hz), when the LC cell behaviour becomes resistive, we can observe the behaviour of a high pass filter. At frequencies above 10 Hz, the LC cell behaves as a capacitance. Therefore, the potential is split between the LC cell and the series capacitor, the well-known voltage divider.

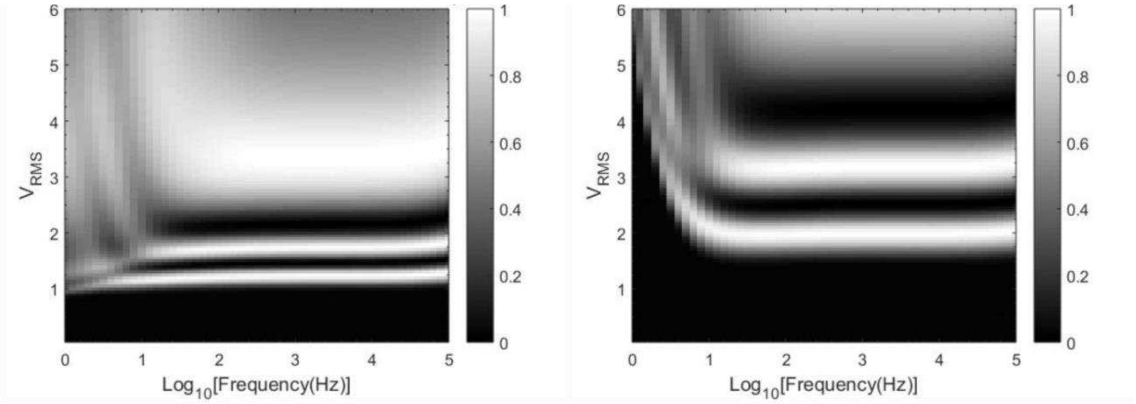

Figure 46: VTF graphs of a LC cell filled with E7 using PEDOT:PSS as AL with a series capacitor of 4.72 nF (right) and without a passive electrical component in series (left).

As previously, we can extract the capacitance value of our LC cell from these measurements. To simplify the problem, we assume that the LC cell acts as a pure capacitor, neglecting the ITO resistance and the LC cell ionic conductivity. The following equation is approximately valid above 10 Hz:

$$\frac{V_{LC_1}}{V_{LC_2}} = A = \left|\frac{Z_{C_{LC}}}{Z_{C_{LC}} + Z_{C_s}}\right|$$

$$C_{LC} = \left(\frac{1}{A} - 1\right) \times C_s$$

The Fréedericksz transition ratio between the two VTF curves, without (V_{LC1}) and with the series capacitance (V_{LC2}), gives the attenuation coefficient (A). C_s is the series capacitor that we fixed to 4.72 nF. Figure 47 depicts the attenuation (dark cross, left axis) and the LC cell capacitance value (red circle, right axis) as a function of frequency, as extracted from the VTF measurements. A good agreement is found with the IS measurements (dashed red line, right axis).

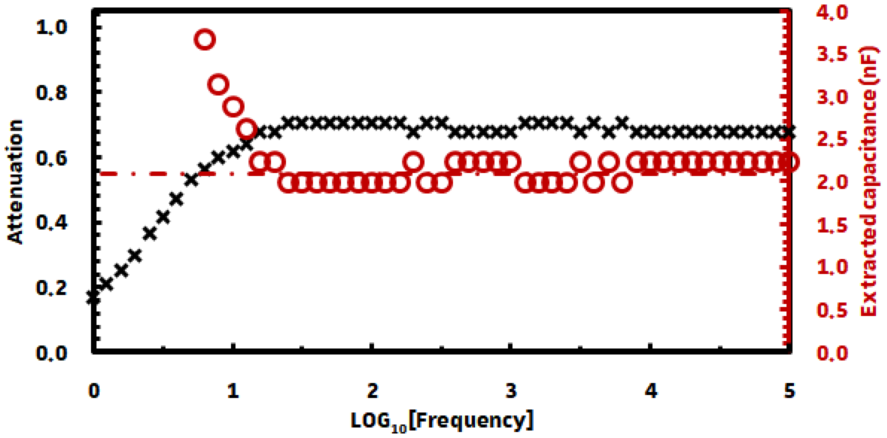

Figure 47: Attenuation dark cross (left axis), extracted capacitance red circle and fitted value by IS measurement dashed red line (right axis).

Below 10 Hz, we should be able to deduce the LC resistance or if you prefer its ionic conductivity. Indeed, below this frequency, the LC cell acts as an imperfect leaky capacitor, that can be modelled by a parallel RC circuit.

$$\frac{V_{LC_2}}{V_{LC_1}} = A = \left|\frac{Z_{LC}}{Z_{LC} + Z_{C_s}}\right|$$

$$R_p = \sqrt{\frac{-A^2}{(AC_s\omega)^2 + (AC_{LC}\omega)^2 + 2C_sC_{LC}\omega^2A^2 - {C_s}^2\omega^2}}$$

The Fréedericksz transition ratio between the two VTF curves measured either without (V_{LC1}) or with the series capacitance (V_{LC2}) yields the attenuation coefficient (A). C_s is the series capacitor (4.72 nF), C_{LC} and R_{LC} the equivalent capacitance (2.1 nF) and resistance of the LC cell.

The extracted resistance (Rp) value is shown in Figure 48. You may notice that its value (red circle, right axis) is higher than the value fitted from IS measurements (4.65 $M\Omega$ dashed red line) and increases with decreasing frequency.

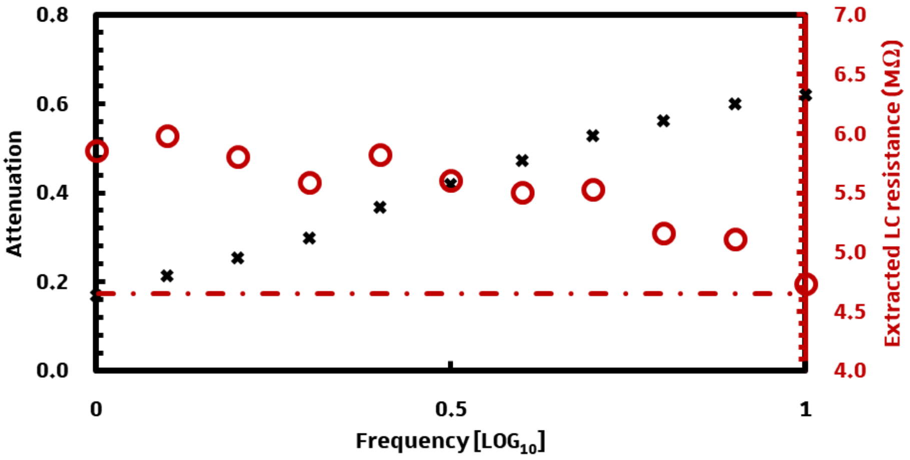

Figure 48: Attenuation dark cross (left axis), extracted resistance red dot and fitted value by IS measurement dashed red line (right axis).

Such a behaviour cannot be easily understood within the framework of our simple electrical model. If the ion motion is unhindered it should lead to a fixed resistivity, this is opposite to our observations. A possible reason for this discrepancy may be ion accumulation at the interfaces. As discussed previously (section 2.3.2), under a DC bias, the accumulation of ions screens the electric field (electrode polarisation). As the frequency is lowered, we get closer to this DC limit. Under such circumstances, the system response is no more linear, leading to a non-constant effective resistance. In addition, the electrode polarisation induces dielectric dispersion characterized by an increase of the dielectric permittivity with decreasing frequency [102], also leading to a non-constant capacitance value.

5.2.3 Simulated impact of a P3HT:PCBM layer.

In an OASLM device, the impedance of a P3HT:PCBM layer will change as a function of light intensity and therefore modify the voltage drop across the LC layer (similar to the effect of changing the series impedance in the previous paragraph). As we want to design a transmissive OASLM, a very thin (around 100 nm) P3HT:PCBM layer has been used. The impedance of the P3HT:PCBM PCL layer (Z_{PCL}) can be approximated by a parallel RC circuit [103]:

$$Z_{PCL} = \frac{R_{PCL}}{jC_{PCL}R_{PCL}\omega + 1}$$

with C_{PCL} the geometrical capacitance, and R_{PCL} the resistance of the P3HT:PCBM layer. C_{PCL} can be calculated assuming a relative dielectric constant value of 3.6, a thickness of 100 nm and a surface of 3.6 cm^2 (corresponds to the surface of the LC cell). This leads to the value of C_{PCL} = 115 nF. The device model and related parameters are given in Figure 49. For the LC layer, the impedance values extracted from the previous measurements are used.

As we have no prior idea yet of the resistivity of the P3HT:PCBM blend as a function of light intensity, its resistance (R_{PCL}) is assumed to vary from 100 Ω to 1MΩ.

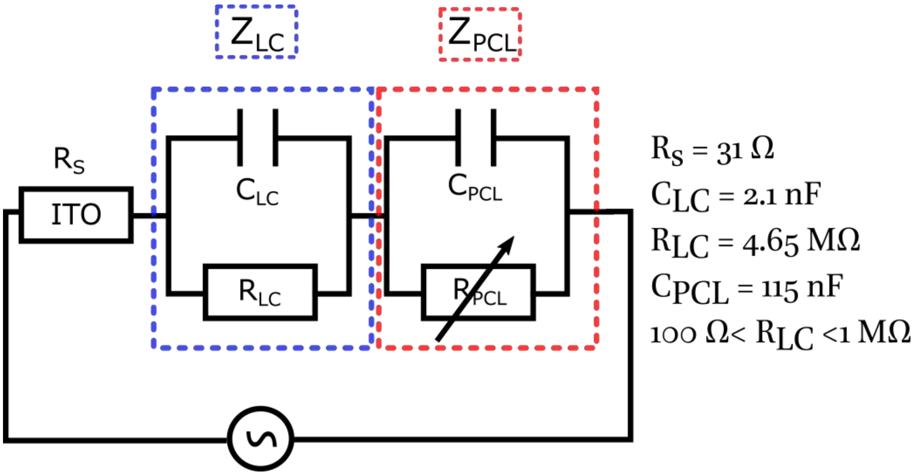

Figure 49: Electrical model and parameters used for the simulation.

The simulation results are given Figure 50. The attenuation induced by the P3HT:PCBM layer is given as a function of frequency for different resistance values (R_{PCL}) 100 Ω (red line), 10 kΩ (green line) and 1 MΩ (dark line).

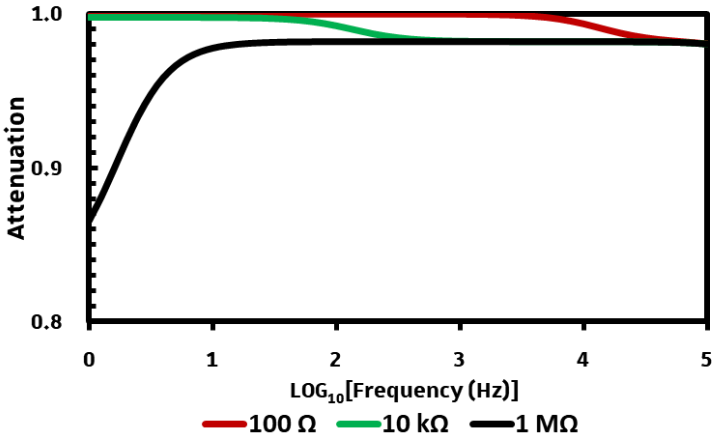

Figure 50: Simulation results of the voltage attenuation induced by a thin P3HT:PCBM layer (<100 nm). R_{PCL} values are specified in the legend.

Using such a thin layer, a significant variation of the threshold voltage should only be observed at low frequency and only if R_{PCL} can reach a sufficiently high resistance value similarly to PVK:C_{60}. An RC parallel circuit behaves as a capacitor above and as a resistor below a given frequency, which equals:

$$f_{LC} = \frac{1}{2\pi R_{LC} C_{LC}} = 16\ Hz\ (\mathrm{Log}_{10}(\mathrm{f}) = 1.2)$$

$$f_{PCL} = \frac{1}{2\pi R_{PCL} C_{PCL}} = 1.4\ Hz\ (\mathrm{Log}_{10}(\mathrm{f}) = 0.14)$$

for the LC and the PC layers respectively.

The circuit formed by Z_{PCL} in series with Z_{LC} will act as a high pass filter between 1.4 Hz and 16 Hz, which explain the large potential drop observed at low frequency when $R_{PCL} = 1\ M\Omega$. Below 1.4 Hz the maximum attenuation is fixed by the resistive tension divider formed by R_{PCL} and R_{LC}.

Above a given frequency, Z_{PCL} equals the impedance of the geometric capacitance. Assuming a threshold voltage of 0.97 V for E7, we should measure a threshold of 0.988 V for $R_{PCL} = 1\ M\Omega$ and 0.97 V for $R_{PCL} = 100\ \Omega$ at 1 kHz. A threshold voltage difference of 0.018 V is hardly detectable experimentally. However, we have shown that during the CPI measurements, the LC impedance decreases and more potential is dropped across the PCL. Consequently, the voltage attenuation will be more pronounced in the high voltage region of the CPI curves. This will be our only way to detect the P3HT:PCBM impedance variation in the high-frequency region (see section 5.2.1.1).

In addition, the electrical model developed above leads us to use the following important approximation for the analysis of the CPI curves obtained on P3HT:PCBM based devices: At high light intensities (low resistance), the potential difference across the LC layer (V_{LC}) equals approximately the voltage applied to the OASLM (V_O).

Indeed, considering that the charge carrier density in the PCL layer is of the order of $p = 2 \times 10^{16} cm^{-3}$ [104], [105] at high light intensities (>40 mW/cm^2 at λ = 532 nm), and that the average hole mobility equals $\mu_p = 3.5 \times 10^{-4} cm^2/(V.s)$ (as measured in section 7.2.1). The resistivity of the P3HT:PCBM PCL is estimated to $\rho_{P3HT} = 9 \times 10^5 \Omega.cm^{-1}$. Assuming further a layer thickness of 200 nm and surface area of 3.6 cm^2 (i.e. identical to the LC cell area), the resistance of P3HT:PCBM will be $R_{PCL} = 5\ \Omega$, which is negligible.

5.2.4 Conclusion

Through the VTF measurements, we quantified the effects of series impedances on the electro-optic response of a standard LC cell. Some well-known effects of LC cells were observed, such as the LC impedance variation with increasing applied voltage, ion screening and the impact of passive electrical components, which has to be taken into account to optimize device transparency or price. Generally, the alignment layers or the ITO series resistance induces such series impedances. In the following chapter, we will use some of the mechanisms described above when characterizing the OASLM as a function of light intensity.

5.3 OASLMs lateral resolution

Having a modulation of the OASLM impedance as a function of frequency is trivial and therefore, we may expect that by introducing an external photoconductor in series with a standard LC cell, we would obtain a modulation of the LC cell response as a function of light intensity. Of course, this would be useless for holographic applications. In our case, we want to translate a spatial variation of light intensity into a spatial variation of refractive index induced by the liquid crystal spatial reorientation. Therefore, observing a light modulation as a function of light intensity on a VTF curve does not guarantee that the OASLM can serve as holographic media. Other physical or electrical parameters are important in that case.

In this section, one important parameter will be further discussed: the spatial resolution (see chapter 3). This parameter can be estimated by measuring the OASLM diffraction efficiency (see section 6.3.5). However, it is important to understand which physical parameters can limit the spatial resolution of an OASLM, in order to be able to improve its spatial resolution. So far, the simplified electrical model presented in the previous sections does not reflect the performances of OASLMs in holographic applications, where the most important parameter is the resolution. The latter is equivalent to the efficiency of differentiating between an illuminated and dark area.

Ideally, only the illuminated area of the photoconductor should show a conductivity increase. Nevertheless, electrical charges may diffuse towards the non-illuminated area decreasing the dark resistivity. Therefore, the LC molecules may reorient even in the neighbouring dark regions, as schematized by Figure 51.

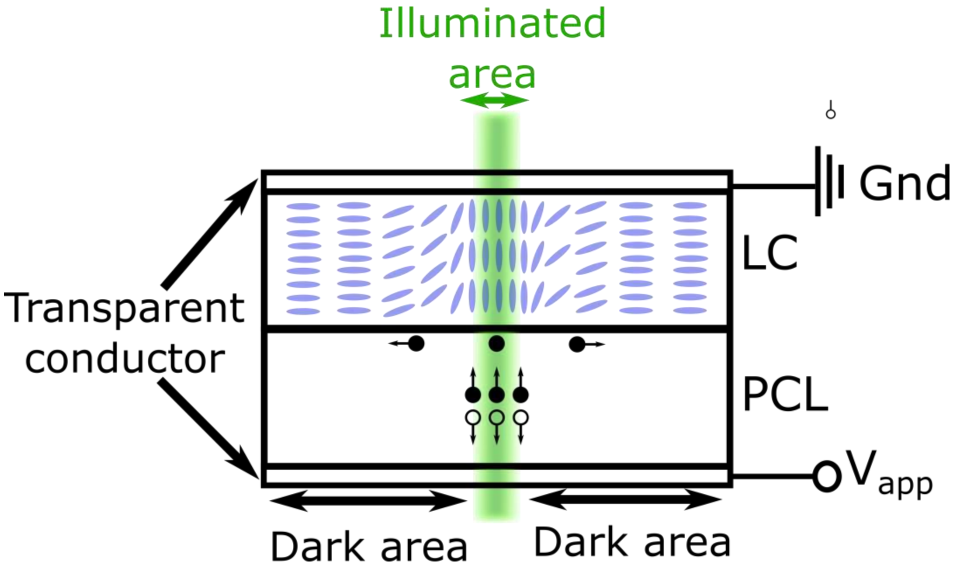

Figure 51: Side view of an OASLM illustrating the lateral charge diffusion, which induces the reorientation of the LC molecules in the dark area.

Once the charge carriers arrive at the PCL/LC interface they diffuse and drift laterally [32] in all direction of space, which is not easy to model electrically. However, we may simplify this problem as follows: As a starting point, we will assume that the OASLM can be divided in two parts. One part of the OASLM is illuminated, while the other is not. This leads to the electrical model depicted in Figure 52. A picture depicts the side view of our simplified OASLM (left) and its electrical model (right). The PCL resistance in the dark area corresponds to $R_{PCL}(D)$, while the resistance in the illuminated area corresponds to R_{PCL}. For simplicity, we will neglect the ITO resistance and it will be assumed that parameters such as the PCL geometric capacitance and the LC impedance (Z_{LC}) do not vary.

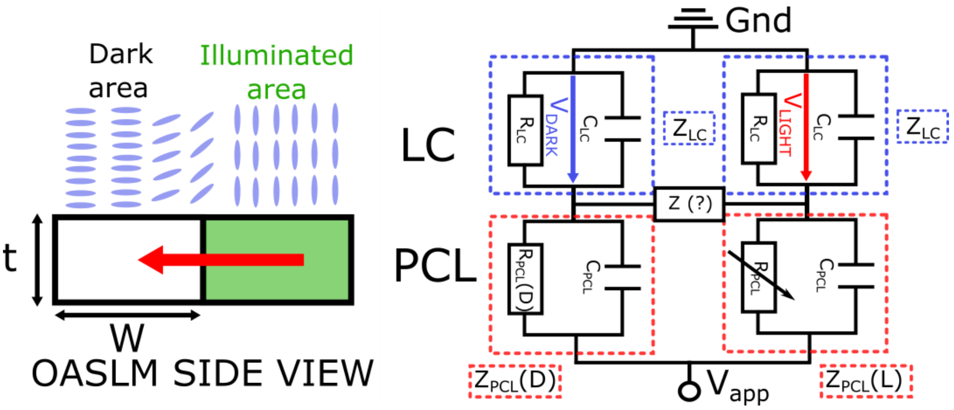

Figure 52: Side view of a simplified OASLM (left) and its equivalent electrical circuit (right).

A charge gradient builds up upon illumination between the dark and illuminated area. The impedance Z (?) is unknown and corresponds to the conduction phenomenon. Ideally, this impedance corresponds to an open circuit, in this case, the potential across the LC layer is always different ($V_{LIGHT} \neq V_{DARK}$), in short, an infinite resolution. In contrast, a short circuit corresponds to the worst case, as the potential across both LC layers would be the same ($V_{LIGHT} = V_{DARK}$). In order to estimate Z (?), we need to estimate the surface impedance of the circuit. The surface of the OASLM and its electrical model (Z (?)) are shown Figure 53. The surface impedance of the dark area (Z_{SPCL}(DARK)) is a parallel RC circuit composed of C_s and R_S(DARK). The surface impedance of the illuminated area (Z_{SPCL}(LIGHT)) is a parallel RC circuit composed of C_s and R_S(LIGHT).

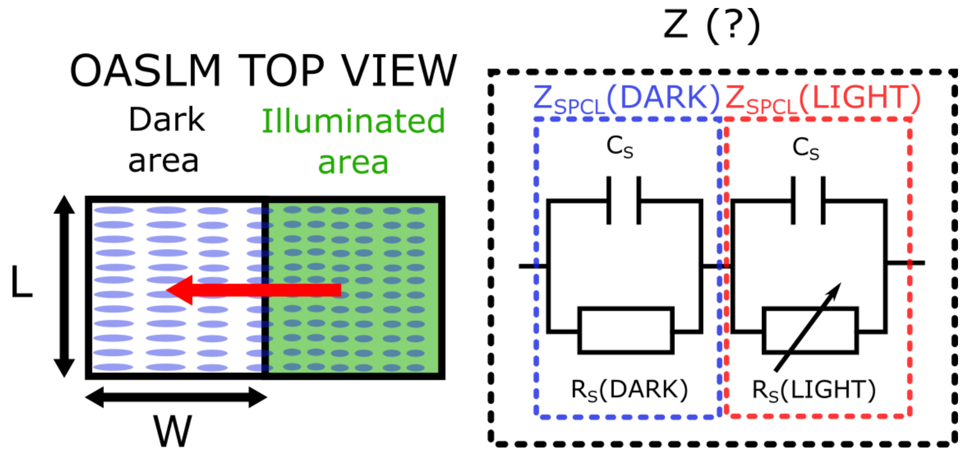

Figure 53: Top view of a simplified OASLM (left) and its equivalent electrical circuit (right).

In this simplified model, as the illumination is homogeneous in the bright area, the charges will flow in only one direction as indicated by the red arrow. R_s is defined by the surface resistance, which can be written:

$$R_s = \rho \frac{L}{W \times t}$$

where t is the PCL thickness. To simplify even more this problem we can state that W = L. In such case, the surface resistance of each layer equals the sheet resistance (R_s). Using a similar reasoning, we can define the sheet capacitance (C_s). C_s and R_s are defined by the following equations:

$$R_s = \frac{\rho}{t} \ and \ C_s = \varepsilon_0 \varepsilon_s t$$

It is important to notice that the values of R_s and C_s do not change if the surface decreases ($S = W \times L$) as long as $W = L$. Therefore, the surface impedance is not modified by a surface change. On the other hand, the values of all the other impedances are affected by a change in surface area. With these equations, all the passive components values of the model can be found assuming that we have the dielectric constant and resistivity values of the PCL and the LC layer. For the LC we will take the values of E7 ($\varepsilon_s = 5.2$, $\rho = 1\times10^8$ Ω.m and a thickness t = 7.75 µm). For the photoconductive layer, we will take the values of Semi-Insulating GaAs whose specifications are given by several manufacturers ($\varepsilon_s = 12.9$, $\rho_{DARK} = 1\times10^6$ Ω.m, $\rho_{LIGHT} = 1\times10^3$ Ω.m and a thickness t = 350 µm). We will simulate the maximum achievable spatial resolution of an OASLM using a GaAs organic PCL. In this model, a surface decrease corresponds to a resolution increase.

The surface (S = W×L and W = L) of the OASLM will be varied using the following values for W and L: 10 µm, 50 µm and 100 µm. In our model, only half of the OASLM is illuminated while the other half is not. This illumination pattern forms a simple image (a bright and a dark pixel). The corresponding spatial resolutions for a pixel of 10, 50 and 100 µm are 50, 10 and 5 lp.mm^{-1}. In this model, as the pixel surface decreases, the corresponding spatial resolution increases. The results of the simulation are given in Figure 54, the complete electrical model and the simulation parameters are given in the appendix. An idea of the resolution can be obtained by simulating the potential difference between the dark and bright pixel. The efficiency of the OASLM at a given spatial resolution is defined by the magnitude of the difference between the voltages dropped across both pixels ($|V_{LIGHT} - V_{DARK}|$see Figure 52).

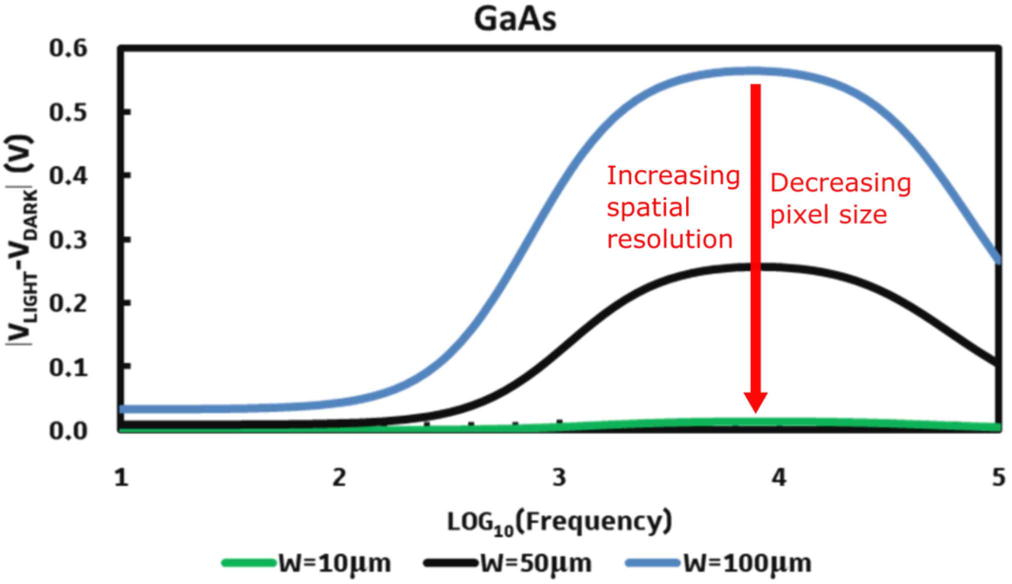

Figure 54: Voltage difference between the LC layer under the bright and dark pixel ($|V_{LIGHT} - V_{DARK}|$) versus frequency for 3 different pixel size as specified on the graph. Decreasing the pixel size is equivalent to increasing the spatial resolution (red arrow).

In Figure 54, the potential difference across the LC layer of both pixels as a function of frequency is plotted for different pixel size. Using these electrical parameters, the LC modulation is maximum around 10 kHz. It can be noticed that if we decrease the pixel size, the voltage difference tends towards zero and therefore the same voltage is applied across the LC layer. This means that an OASLM using a GaAs photoconductor has a limited spatial resolution. Experimentally, the resolution of a similar system using a GaAs photoconductor has been estimated from the measurement of the diffraction efficiency. The optimal resolution of such systems is generally less than 5 lp.mm^{-1} [13] as the diffraction efficiency decreases with increasing the resolution.

To conclude, through these simulations, we may learn that the spatial resolution is limited by the sheet resistance and the sheet capacitance of the photoconductor. In order to increase the spatial resolution, these parameters have to be optimized. One option is to decrease the thickness of the photoconductor as it increases R_s. Another route is to change the nature of the semiconductor, for instance using inorganic or organic thin films such as a:Si-H or PVK:C_{60}. For PVK:C_{60}, this electrical model has to be adapted to the case of photoconducting materials whose dark resistance is higher than that of the liquid crystal. On the other hand, if the PCL impedance is similar or lower than that of the LC, it remains unclear which layer is limiting the spatial resolution.

In the next chapter, we will present the first experimental results obtained using P3HT:PCBM as a photoconductive layer.

6 OASLM with a P3HT:PCBM layer

In the following chapter, we will study OASLMs using a thin P3HT:PCBM layer. Thin layers should not give a large LC modulation in the high-frequency region, as their impedance is small. Nevertheless, in theory, we should be able to probe optically the voltage shift induced by a light intensity change even with a 100 nm thick organic photoconductive layer.

The mass ratio of P3HT:PCBM has a strong impact on the optoelectronic performances of bulk heterojunction devices. It is expected to influence the amount of photo-generated charges and therefore the photoconductivity. Indeed, as explained in section 2.5.1, light absorption by pure P3HT leads to strongly bound excitons that recombine rather than dissociating into free charges. By increasing the PCBM content, we increase the D/A interface and thus the probability of photo-induced excitons to dissociate into free charge carriers.

To compare our benchmark material P3HT:PCBM to PVK:C_{60}, we started with the same layer sequence than the one used by Southampton for manufacturing PVK:C_{60} LC cells, namely: ITO/PCL/LC/AL/ITO schematized on Figure 55. Note that the PCL layer needs to be brushed in order to function as an AL as well. All the samples presented in this chapter are based on this structure.

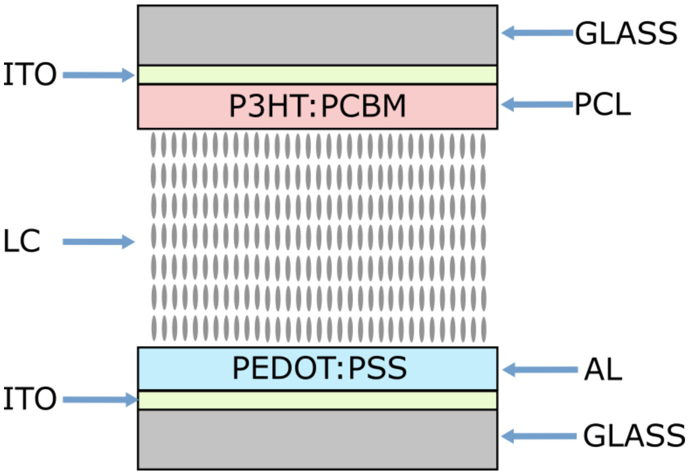

Figure 55: Structure of the OASLM devices discussed in this chapter.

However, unlike the Southampton devices, the cell gap was fixed to 7.75 µm. Also, instead of PI, we used PEDOT:PSS as top AL. This choice is motivated in particular by the facile deposition of PEDOT:PSS from an aqueous solution. In addition, the impedance of PEDOT:PSS is negligible in the low-frequency region, which is not the case of a thin polyimide layer, as shown section 4.3.2.

In these experiments, four different blends of P3HT:PCBM, with respectively, (1:0), (1:0.01), (1:0.5) and (1:1) weight ratios have been used, following the experimental procedure described in chapter 5. All LC cells were filled with the E7 mixture. A 532 nm laser was used as light source for CPI or VTF measurements.

6.1 Pure P3HT as PCL

In this first experiment, we used a pure layer of P3HT as PCL, without PCBM, as a reference. The CPI responses of this sample at 10 kHz and at two different light intensities of, respectively, 0.024 mW/cm² and 49 mW/cm² are depicted in Figure 56.

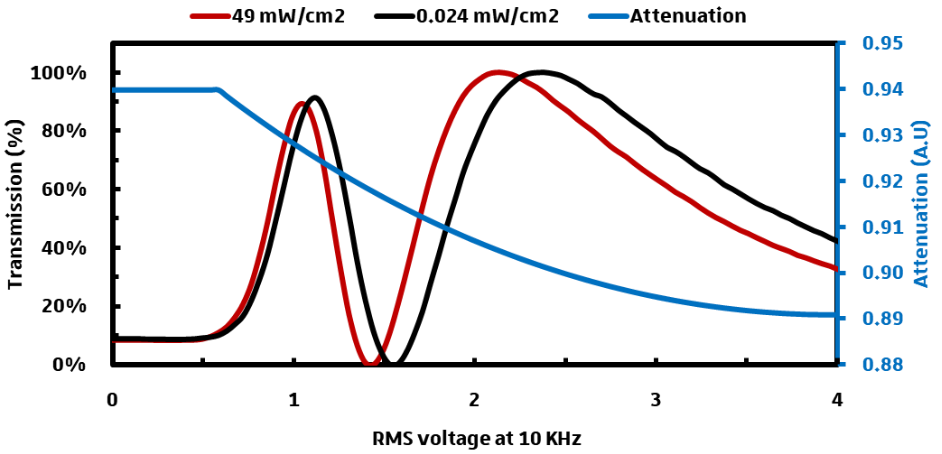

Figure 56: CPI measurement of an ITO/P3HT/E7/PEDOT:PSS/ITO OASLM at two different light intensities (49 mW/cm² red line and 24 µW/cm² black line, λ = 532 nm). The attenuation decreases with applied voltage (blue line).

The first measurement was made at low light intensity (0.024 mW/cm², dark line) and the second measurement at high light intensity (49 mW/cm², red line). The small number of peaks indicates that the cell gap was thinner than expected.

The thickness of the LC layer has been estimated to 4.3 μm from the CPI measurements assuming a birefringence of 0.235 for E7 (see section 4.3.1). In addition, it should be noted that the threshold voltage is around 0.5 V, which indicates that the PCL layer induces a large LC pretilt, as explained section 4.3.1. Indeed, when PEDOT:PSS or PI were used as the alignment layer, the LC cells displayed a threshold voltage close to 1V (see section 4.3.1). In addition, the light seems to be only partially polarized after the LC cell output: as indicated by the CPI measurements, the maxima and minima are different with increasing voltage, which is not the case with our standard LC cell using both PEDOT:PSS or PI as ALs. This could be due to the large pretilt angle at the P3HT/LC interface.

It is also possible that rubbing the P3HT:PCBM layer does induce potential damages that are detrimental for the performances of the device and modifies the orientation of the first layer of polymer chains, rendering the absorption anisotropic [117]. In other words, both components of the incident polarized light beam (45°) may experience a different refractive index as well as different absorption coefficients. Therefore, rubbing the PCL layer induces a small dichroism, rendering the optical response of the LC cell more difficult to apprehend.

With increasing light intensity, the curves shift to the left, which indicates that more potential is dropped across the LC layer. Thus, the impedance of the pure P3HT layer varies with light intensity suggesting a rather unexpected photoconductive behaviour. In the absence of PCBM, exciton dissociation might occur at the ITO/P3HT interface and possibly at the LC/P3HT interface, leading consequently to the observed photoconductivity.

The voltage attenuation across the LC cell has been estimated from the voltage shift between the two curves induced by increasing light intensity. To measure the attenuation versus RMS voltage, I assumed that at high light intensities, the PCL impedance is negligible and therefore the potential drop across the LC layer $(V_{LC}(H))$ equals the voltage applied by the function generator $(V_0(H))$. However, at low light intensities, the PCL impedance is not negligible and the voltage across the LC layer is different $(V_{LC}(L))$ from the total applied voltage to the device ($V_0(L)$). Consequently, decreasing the light intensities is similar to the addition of series impedance. However, for a given phase shift the same potential is dropped across the LC layer at low and high light intensity. At low light intensity, as the PCL impedance is non-negligible, the same phase shift is obtained at higher applied voltages. The attenuation is the ratio between these two voltage values and should be less than one.

$$At\ high\ light\ intensities\ A = \left|\frac{V_{LC}(H)}{V_0(H)}\right| = \left|\frac{Z_{LC}}{Z_{LC} + Z_{PCL}}\right|,$$

$$Z_{PCL} \ll Z_{LC}\ therefore\ \ V_{LC}(H) = V_0(H)$$

$$at\ low\ light\ intensities\ A = \left|\frac{V_{LC}(L)}{V_0(L)}\right| = \left|\frac{Z_{LC}}{Z_{LC} + Z_{PCL}}\right| = \left|\frac{V_0(H)}{V_0(L)}\right| < 1$$

For instance, the curves shift from 1.035V (first maxima at 49 mW/cm^2) at high light intensity, where it is assumed that all the potential is dropped across the LC layer, to 1.125V (first maxima at 0.024 mW/cm^2) at low light intensity. Therefore, $A = 0.92$ but in both cases, only 1.035V is dropped across the LC layer.

The attenuation value (Figure 56) decreases with increasing voltage. This is similar to the case observed with a passive series resistance described in section 5.2.1.1. With increasing the applied voltage to the cell, the LC molecules (with a positive dielectric anisotropy $\varepsilon_\perp - \varepsilon_\parallel > 0$) reorients from a planar ($\varepsilon_\parallel = 5.2, for\ E7$) to a vertical ($\varepsilon_\perp = 19\ for\ E7$) alignment with respect to the substrates. Consequently, with increasing voltages, the relative dielectric constant of the LC layer increases and so does the capacitance of the LC layer at a given voltage above the threshold:

$$C = \frac{\varepsilon_0 \varepsilon_s A}{d}$$

This implies that the impedance of the LC layer, which is assumed to be purely capacitive at these frequencies (10 kHz), decreases with increasing the applied voltage to the LC cell following:

$$|Z_{LC}| = \frac{1}{2\pi f C}$$

Therefore, at low light intensity, when the PCL impedance is not negligible, the attenuation ratio extracted from the CPI curves decreases with applied voltage. This trend is similar to the case described in section 5.2.1.1 on Figure 45. Therefore, the P3HT layer acts as a standard PCL.

As a standard procedure, I generally did several measurements to crosscheck the obtained results and to confirm the reproducibility of the response. Additional CPI measurements were made by changing the light intensity in the opposite direction: For the results shown in Figure 57, the first CPI curve was measured at high intensity (49 mW/cm2, red line) and the subsequent measurements at low light intensity (24 μW/cm2, dark lines).

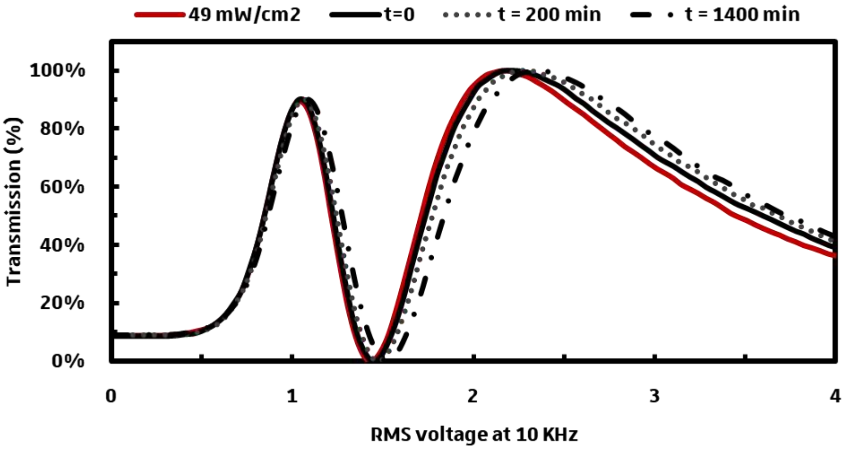

Figure 57: CPI measurement of an ITO/P3HT/E7/PEDOT:PSS/ITO OASLM with a 532 nm laser. The intensity of the first measurement was 49 mW/cm² (red line) and the intensity of the subsequent measurements was 24 μW/cm² (dark lines).

The voltage shift between the first measurement at a high light intensity (red line) and the second measurement immediately after decreasing the light intensity (dark continuous lines) was lower than previously (Figure 58). After keeping the cell under the same low-intensity light illumination conditions for 200 minutes the voltage shift increased, indicating that the resistivity of the PCL has increased again. It took an additional 1000 minutes (dark dashed line) for the PCL to recover its initial resistivity and yield the same optical response as the very first measurement shown in Figure 56.

It appears that upon illumination the conductivity of a P3HT PCL layer increases rapidly, but it needs hours to decrease to its dark value. In the literature, a similar phenomenon has been reported by Kim et al. [106] on a 10 µm P3HT thick diode comprised between gold contacts. Upon light exposure, their devices responded quickly but it took hours to recover the initial dark conductivity when placed in the darkness. They concluded that the persistent photoconductivity might be induced by a slow detrapping process from deep charge traps. It is likely that our observations are a signature of a similar process.

I mentioned before that the gap of the LC cell was thinner than expected. It is most likely that during the cell assembly, the pressure applied on the LC cell was too high, thereby reducing the gap in the centre of the LC cell [107]. Additional LC cells made from the same batch possessed a gap closer to 7.75 µm. The CPI curve of such a cell is depicted in Figure 58 (a).

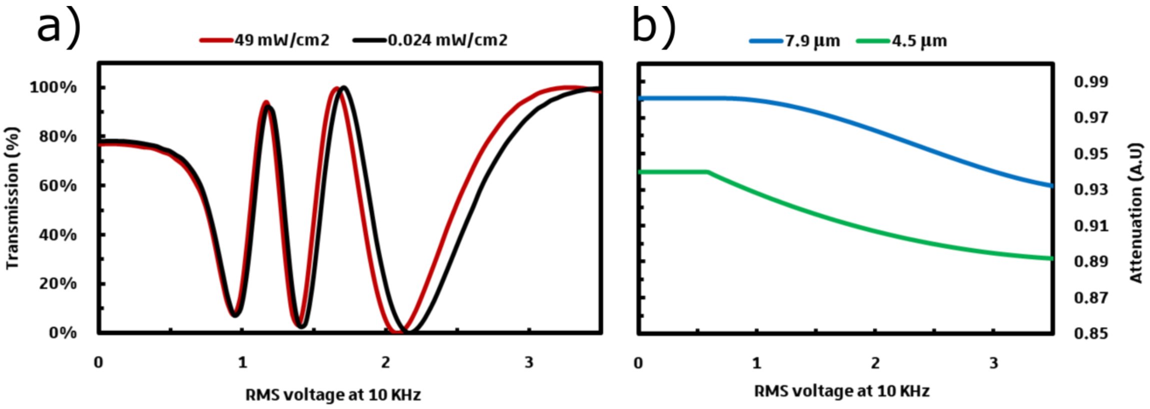

Figure 58: (a) CPI measurement of an OASLM using a P3HT photoconductive layer at two different light intensities (49 mW/cm2 red line and 24 µW/cm2 black line, λ = 532 nm). (b) Voltage attenuation across the LC layer induced by the PCL impedance variation for a gap of 7.6 µm (blue line) and 4.3 µm (green line).

The same experimental conditions were used for both CPI measurements (Figure 56 for the thin (4.3 µm) and Figure 58 (a) the thick samples (7.6 µm). The CPI curve shifts to the left with increasing light intensity, similar to what has been observed for the thinner sample. However, the attenuation induced by the P3HT layer is less pronounced than for the thinner cell. As for the latter, the LC layer was thinner, its impedance was smaller (larger capacitance). Therefore, the voltage attenuation induced by the PCL was more pronounced for the cell with a thin LC layer. Cells with similar gap thicknesses have been used to compare PCL with different P3HT:PCBM weight ratios.

To conclude, it is worth highlighting several observations made on P3HT PCL devices which distinguish them from PVK:C_{60} based devices. First, we do observe a modulation (although rather weak) of the LC layer as a function of light intensity at a frequency of 10 kHz, which is 3 orders of magnitude higher than the usable frequency of the PVK:C_{60} devices [38]. Second, the P3HT layer seems to induce a high pretilt angle, as the threshold voltage is around 0.5V, which reduces the total accessible change in birefringence. We will have to add an interfacial layer between the PCL and the LC in order to obtain a planar alignment (i.e. lower pretilt angle) (see section 4.3.1). Third The P3HT layer acts as a photoconductor, as the attenuation ratio decreases with the voltage applied to the LC cell. Finally, these samples showed a "persistent photoexcitation effect", the P3HT layer needing hours to re-establish its dark conductivity.

In the next experiment, we will use three different P3HT:PCBM blends, with respectively, (1:0.01), (1:0.5) and (1:1) weight ratios. The OASLM structure and the parameters such as the light wavelength (λ = 532 nm) or the frequency (10 kHz) will be kept constant.

6.2 P3HT:PCBM blends

Increasing the PCBM concentration should facilitate the dissociation of excitons and increase the number of free charges. Therefore, we expected a higher conductivity variation leading to a stronger light-induced effect in our OASLMs.

In the first experiment, we used a P3HT:PCBM blend with a (1:0.01) weight ratio as PCL. The light intensity was varied from 0.0018 mW/cm^2 to 49 mW/cm^2. The cell gap was estimated to 6.4 µm (from the CPI curve at the lowest intensity). The CPI curves at 10 kHz are depicted in Figure 59.

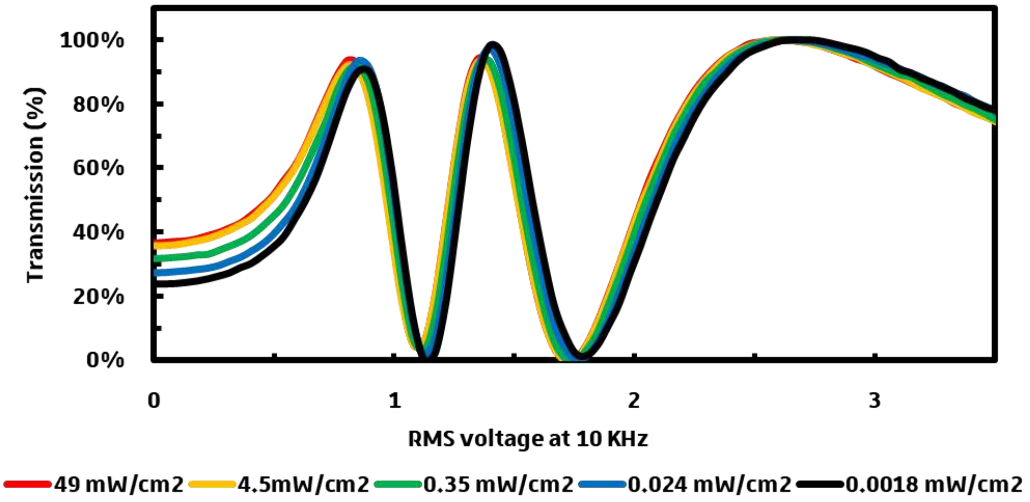

Figure 59: CPI measurement of an ITO/P3HT:PCBM(1:0.01)/E7/PEDOT:PSS/ITO OASLM at different light intensity as specified on the graph (λ = 532 nm).

As observed previously, at 10 kHz the thin P3HT:PCBM (1:0.01) PCL induces a shift to the left of the CPI curves with increasing light intensity. We note however an important difference in the OASLM response at low voltages. The OASLM transmittance is impacted by the light intensity down to zero RMS voltage, pointing out a decreasing birefringence. In other words, the threshold voltage appears to be negligible. This behaviour was not present in the cells including pure P3HT as the PCL. Such a light-induced change in birefringence at 0V cannot be explained in terms of a simple photoconductive layer.

The addition of a small amount of PCBM has thus changed the OASLM response tremendously. In addition, these samples do not display the time-dependent response that was previously attributed to persistent photoconductivity. A priori, two different phenomena may be at the origin of this behaviour: (1) the presence of PCBM may result in a pretilt angle change of the LC molecules at the PCL/LC interface that, for some reason, increases with light intensity, or (2) the PCL layer spontaneously generates of photovoltage under illumination. In other words, it behaves like a photovoltaic layer. Converting a small fraction of incident photon energy into electrical energy would allow the LC molecules to reorient at 0V. It is likely that the high pretilt angle at the LC/PCL interface (see section 4.3.1) facilitates the response of the LC molecules to the photo-voltage.

Both effects are linked to the addition of PCBM. Therefore, with increasing the PCBM concentration, we expected the behaviour at 0V to be more pronounced.

Accordingly, we increased the amount of PCBM in the P3HT:PCBM blend to a (1:0.5) weight ratio. The light intensity was varied from 0.0018 mW/cm² to 49 mW/cm². The corresponding CPI response at 10 kHz is depicted Figure 60. The cell gap was 7.6 µm (estimated from the CPI curve at the lowest intensity).

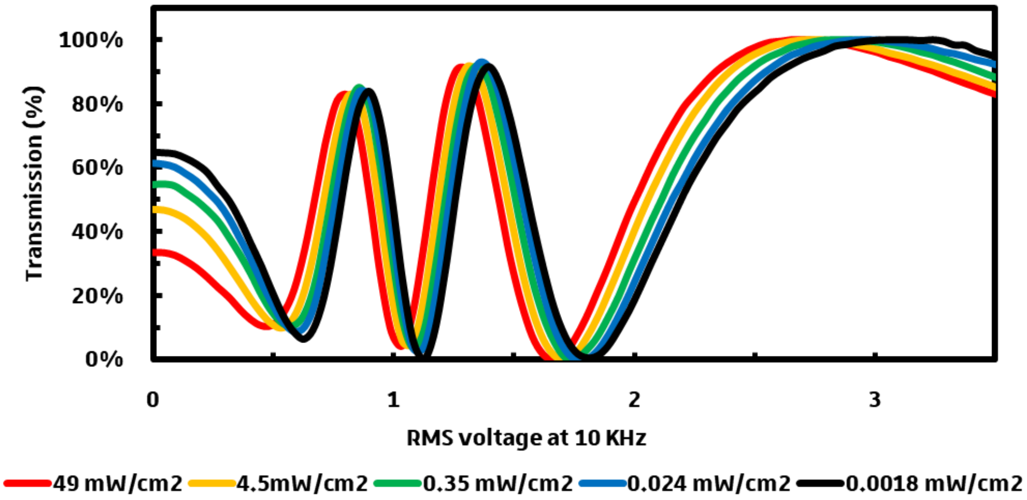

Figure 60: CPI measurement of an ITO/P3HT:PCBM (1:0.5)/E7/PEDOT:PSS/ITO OASLM at different light intensity as specified on the graph (λ = 532 nm).

As expected, the thin P3HT:PCBM (1:0.5) PCL induces a voltage shift to the left which increases with light intensity. Looking at the low voltage part of the curves, we can observe again that there is no threshold voltage. Moreover, the increasing transmission at 0V indicates that the birefringence diminishes with increasing light intensity. Overall, the effect is more pronounced than for the sample with a (1:0.01) P3HT:PCBM weight ratio.

The amount of PCBM was further increased to a (1:1) weight ratio. The CPI response at 10 kHz of this OASLM is depicted Figure 61. The cell gap was 7.3 µm. The same but still more pronounced behaviour than for the previous samples (absence of a threshold voltage, decreasing birefringence with increasing light intensity at 0V) can be observed.

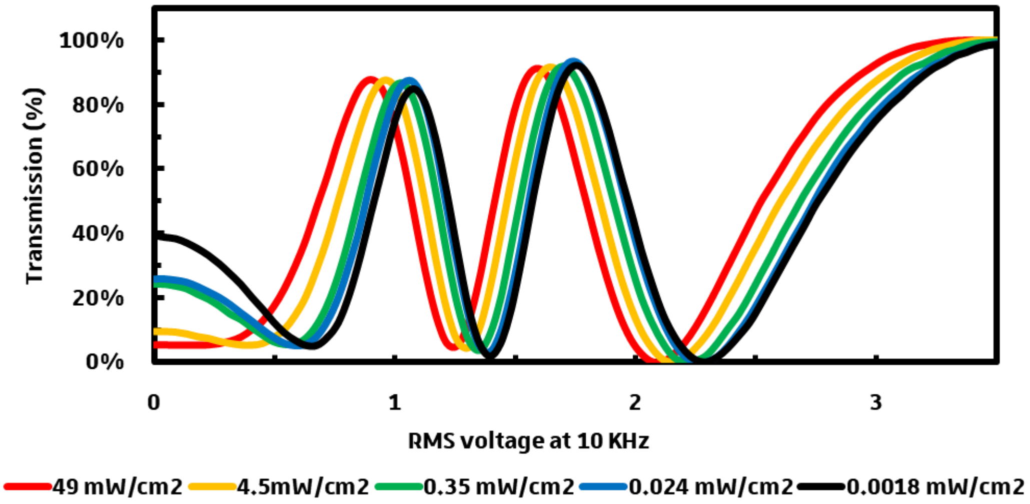

Figure 61: CPI measurement of an ITO/P3HT:PCBM (1:1)/E7/PEDOT:PSS/ITO OASLM at different light intensity as specified on the graph (λ = 532 nm).

It is however not straightforward to differentiate quantitatively the responses obtained with P3HT:PCBM ratios of (1:0.5) and (1:1), by simply comparing both CPI curves. I, therefore, calculated for each device the birefringence at the highest and lowest light intensity as a function of applied voltage, following the method described in section 4.3.1. I had to assume that the birefringence was 0.235 at the lowest light intensity for each case. The difference between the birefringence values at the lowest and the highest light intensity is defined by:

$$\delta\Delta n = \Delta n(0.0018\, mW.cm^{-2}) - \Delta n(49\, mW.cm^{-2})$$

The $\delta\Delta n$ values are plotted as a function of applied voltage in Figure 62 for the four samples.

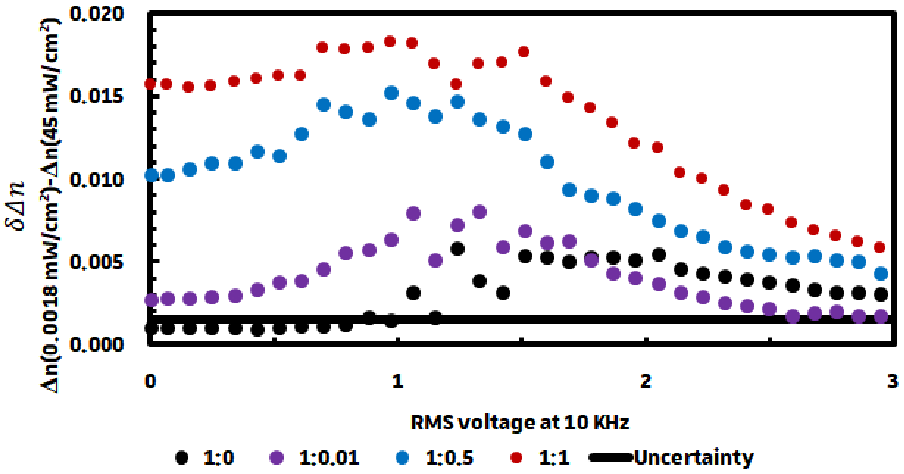

Figure 62: Birefringence difference between the lowest and highest light intensity $\delta\Delta n$ of OASLMs using a P3HT:PCBM photoconductor at different weight ratios, black dot(1:0), purple dot (1:0.1), blue dot (1:0.5) and red dot (1:1). The uncertainty on the total birefringence of the LC cells is indicated by the dark line.

Note that the total birefringence of the LC can vary by 0.0015 at 0V, due to a temperature variation of 1°C (dark line). The measured $\delta\Delta n$ at 0V for the OASLM with a pure P3HT PCL (Dark dot) is below this value. This small variation may thus have been induced merely by a temperature difference of less than 0.7°C. The increase in $\delta\Delta n$ with applied bias is characteristic for an OASLM with a photoconductor, as you need to apply a minimum voltage to the OASLM at least superior to the LC threshold voltage to modify the LC phase shift as a function of light intensity. However, $\delta\Delta n$ reaches only a maximum value of 0.0058 (at 1,24V), 2.5% of the LC total birefringence (0.235), which is too small for most applications.

The P3HT:PCBM blends do not act as a simple photoconductor. At a P3HT:PCBM weight ratio of (1:0.01), (purple dot), the measured $\delta\Delta n$ at 0V is 0.0027. $\delta\Delta n$ increases also with applied bias, as expected for a photoconductor. It is possible that both effects, photovoltage or pretilt angle changes, and photoconductivity contribute to the cell response. The measured maximum $\delta\Delta n$ is slightly higher than the one measured for the pure P3HT cell: 0.008 at 1.1 V, and 3.4% of the total E7 birefringence.

A similar trend is observed for the larger PCBM concentrations. At a weight ratio of (1:0.5), the measured $\delta\Delta n$ is even more important: 0.01 at 0V (4.3% of the total birefringence of E7) and 0.15 at 0.97 V (6.4% of the total birefringence of E7). The best results are obtained with a P3HT:PCBM weight ratio of (1:1). The measured maximum $\delta\Delta n$ reaches 0.016 at 0V (6.8% of the total birefringence of E7) and 0.182 at 1.06 V (7.7% of the total birefringence of E7). It can be noted that $\delta\Delta n$ reaches a maximum then decreases with applied voltage. A possible explanation for this behaviour is given in the appendix.

These results clearly show that the birefringence variation at 0V increases with increasing PCBM concentration, with the highest $\delta\Delta n$ obtained at a P3HT:PCBM weight ratio of (1:1). It is interesting to note that when P3HT:PCBM blends are used as active layer in an organic solar cell, the best power conversion efficiencies are obtained with similar weight ratios. However, it is still possible that the presence of PCBM at the interface with the LC cell induces a photosensitive modification of the pretilt angle. Therefore, further analyses are required to distinguish between both mechanisms.

LCLVs (Liquid Crystal Light Valves) that use a standard photoconductive layer generally show a birefringence variation that decreases *linearly* as a function of light intensity [24]. For comparison, the birefringence dependence on light intensity of the device with a P3HT:PCBM weight ratio of (1:1) is depicted in Figure 63 (a). Also shown is the response, at different applied biases, of an OASLM reported in [24] which uses an inorganic BSO PCL (Figure 63 (b)). The same wavelength (λ = 532 nm) was used in both cases.

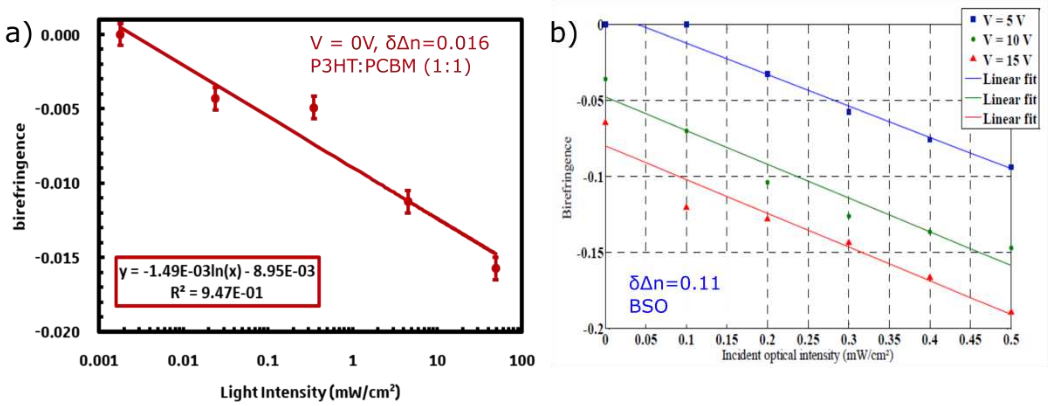

Figure 63: Birefringence variation versus light intensity (λ = 532 nm) of (a) P3HT:PCBM (1:1) LCLV at 0 V_{RMS} and (b) a BSO LCLV at 5, 10 and 15 V. Reproduced from [108]

Importantly, the P3HT:PCBM "PCL" induces a birefringence variation that depends logarithmically on light intensity, whereas BSO PCL shows a linear dependence. This discrepancy corroborates that both devices rely on different physical mechanisms. Moreover, the logarithmic dependence correlates with well-known logarithmic increase in open-circuit voltage delivered by a solar cell with increasing light intensity [109], suggesting that the appearance of a photo-voltage (i.e. equivalent to the open-circuit voltage of a solar cell) in the P3HT:PCBM based OASLM devices is responsible for their responses at 0V.

While the light-induced birefringence change in P3HT:PCBM based OASLMs does not require to apply a voltage, (unlike BSO devices where the best performances occur for an RMS voltage of 5V), the amplitude in birefringence change remains rather small. For the organic "PCL" δΔn = 0.016, which corresponds to only 6.7% of the total birefringence of the LC (E7, Δn = 0.235). To be compared with the BSO showcase: δΔn = 0.11, corresponding to 45% of the total birefringence of their LC (E48, Δn = 0.245 at 20°C [110]).

The results remain nevertheless highly promising as the P3HT:PCBM devices have not been optimized yet. Moreover, the organic OASLMs possess a major advantage compared to a standard inorganic photoconductor, as no external power source is needed. This is similar to devices based on Lithium Niobate "photovoltaic" substrates but has the advantage to be achieved with solution-processed materials.

It is worth mentioning that we checked for the presence of hysteresis in the device response that might be induced by ionic accumulation over time under the “DC photovoltage”. We found that the response was stable. To our knowledge, this phenomenon has never been observed with organic photosensitive materials before. We therefore pushed the investigations further in order to explain this phenomenon.

6.3 Additional measurements

In this section, we will present additional measurements done on our best performing sample (P3HT:PCBM at (1:1) weight ratio) in order to investigate the device stability. For most applications, the long-term stability of the device response is crucial. For instance, LCLVs that rely on "photovoltaic" substrates such as LiNbO3, a transient response of several seconds, that depends on the illumination time, has been reported [51]. It appears that such devices cannot reach a steady state. It is interesting to check how P3HT:PCBM compare to these devices. In addition, it is not totally clear if the birefringence at 0V is at least partly induced by a variation of the LC pretilt angle at the interface LC/PCL interface. We will therefore present additional electrical measurements. These contain features that are characteristic of our OASLM structure and allow us to propose a simple electrical model to extract electrical information from the optical CPI measurements. Next, the diffraction efficiency of the P3HT:PCBM OASLM has been measured to estimate the potential of our OASLM for holographic applications. Finally, a tentative estimation of the pretilt induced by the P3HT:PCBM layer will be presented.

6.3.1 VTF & device stability measurements

VTF measurements were done on the above samples for different P3HT:PCBM blends weight ratios (1:0.01), (1:0.5) and (1:1) at 5 different light intensities (0.0018, 0.024, 0.35, 4.5 and 49 mW/cm^2) and with a wavelength of λ = 532 nm.

The voltage was varied from 0 to 3.5 V_{RMS} with a step of 0.035 V while the frequency was varied from 1 (10 Hz) to 5 (100 kHz) with a LOG_{10} step of 0.1. A colour code is used to depict the average light intensity measured by the photodiode (dark pixel for the lowest intensity and white for the highest intensity). The results are presented in Figure 64 for the device based on a P3HT:PCBM (1:1) PCL that was exposed to a light intensity of 49 (left) and 0.0018 (right) mW/cm^2.

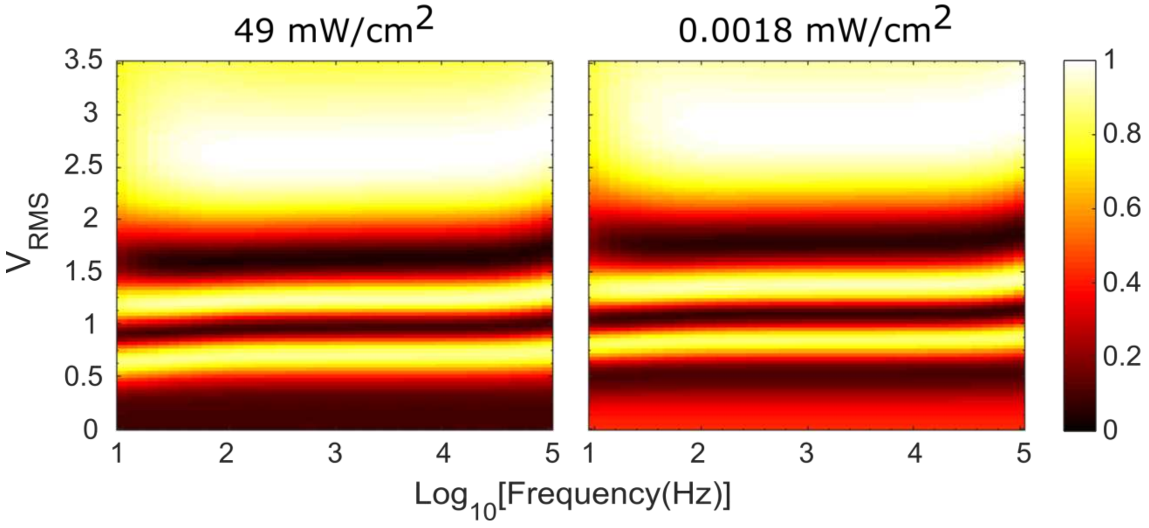

Figure 64: VTF graph showing the frequency dependence of P3HT:PCBM based OASLM with a 1:1 ratio, at a light intensity of 49 mW/cm^2 (left) and 0.0018 mW/cm^2 (right), λ = 532 nm.

The VTF method was designed to follow the threshold voltage variation of a LC cell as a function of frequency, voltage and light intensity, for OASLMs based on a photoconductive layer. If the thin P3HT:PCBM layer behaved as a photoconductor, the threshold voltage should be around 0.97 V (i.e. characteristic for E7). As shown in Figure 66, the threshold voltage is virtually zero at all frequencies (compare colours near 0 V_{RMS} for both light intensities). The total phase shift ($\delta = \frac{2\pi d\Delta n}{\lambda}$, see section 4.3.1) of the LC cell is more important at low light intensity: An RMS voltage close to 0.5~0.6 V_{RMS} needs to be applied to induce the same retardation than the one observed at high light intensity. As this value corresponds to the photovoltage generated by a P3HT:PCBM photovoltaic cell [111], it is a strong evidence that the photovoltaic effect might indeed be at the origin of these changes.

Since the photovoltaic effect appears to be behind the birefringence variation at 0V, we may wonder if it induces accumulation of ions that could lead to hysteresis effects in the device response similar to those observed on P3HT only devices. It is important to point out that each VTF measurement at a given light intensity last 3 hours! The well-defined VTF response is, therefore, a strong indicator of the stability and reproducibility of the device response.

Moreover, several tests were made on different devices using the same layer structure. An example is shown Figure 65. In this case, the cell thickness was estimated to 6.4 µm, and a P3HT:PCBM layer with a (1:0.8) ratio was used for this cell. The light intensity was varied (from 78 mW/cm^2 to 0.016 mW/cm^2). For each light intensity, the voltage was varied from 0 to 4.5 V_{RMS} and then from 4.5 to 0 V_{RMS} at 10 kHz to check the presence of an eventual hysteresis. A temporisation of 3 seconds was set between each measurement point. The total duration of each individual CPI measurement was 10 minutes.

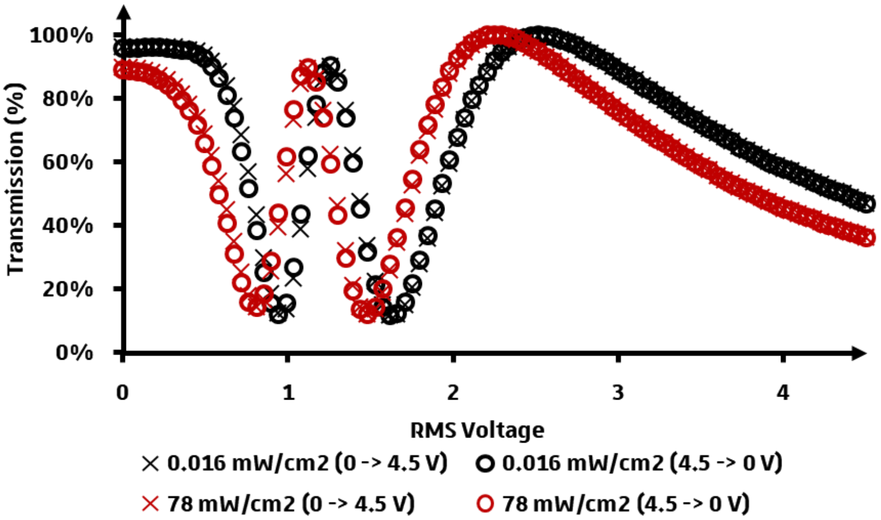

Figure 65: Stability testing of an ITO/P3HT:PCBM/E7/PEDOT:PSS/LC cell.

The first measurement was made at high light intensity and the second at low light intensity. The curves superimpose perfectly, no hysteresis is observed. This confirms that the OASLMs are stable under illumination, under the condition that an external AC bias (rather than DC) is used to address the LC cell.

6.3.2 Electrical behaviour

From the previous, optical, measurements, we found that the high light intensity induces a phase shift that is equivalent to the shift induced by an external AC voltage of 0.5~0.6 V. Since it is likely that this corresponds to a photovoltage produced by the P3HT:PCBM photovoltaic layer, we tried to confirm this observation by additional current-voltage measurements.

In this experiment, the current response of an OASLM using P3HT:PCBM(1:1) blend was monitored. The current was measured versus time using a preamplifier (Model 1211 from DL Instruments). The device was in dark conditions before the laser light was switched on. The results are depicted in Figure 66.

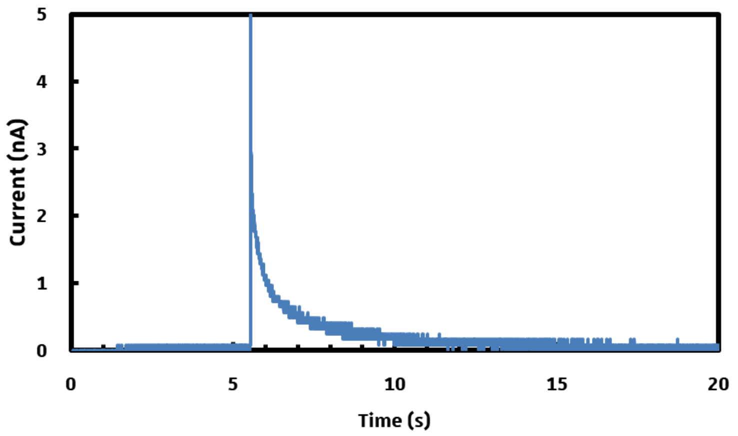

Figure 66: OASLM with a P3HT:PCBM (1:1) photosensitive layer current behaviour before and after the laser light is switched on.

Upon illumination (at t = 5.5 s), we observe a transient current, which decreases over time. The photocurrent never reaches a steady state, which indicates that ions accumulate on at least one interface.

While the transient photocurrent in the absence of an applied voltage confirms that we do have a photovoltaic effect, it does not allow us to measure electrically the open circuit voltage. Therefore, we needed to deduce the photovoltage (called Voc or “open-circuit voltage” below, in analogy with a photovoltaic device) from the optical measurements.

6.3.3 Voc estimation from optical measurements

How can we estimate the DC photovoltage value produced by the P3HT:PCBM layer which causes the reorientation of the LC molecules? In our case, two effects may influence the LC reorientation: the photovoltaic effect and the change in impedance. The CPI curves of a P3HT:PCBM (1:1) device that has been discussed in section 6.2, were obtained at the lowest and highest light intensity (as specified on the graph) are reported again in Figure 67 for clarity. The voltage shift between both CPI curves, which is induced by the increasing light intensity, is specified by green arrows at some particular points.

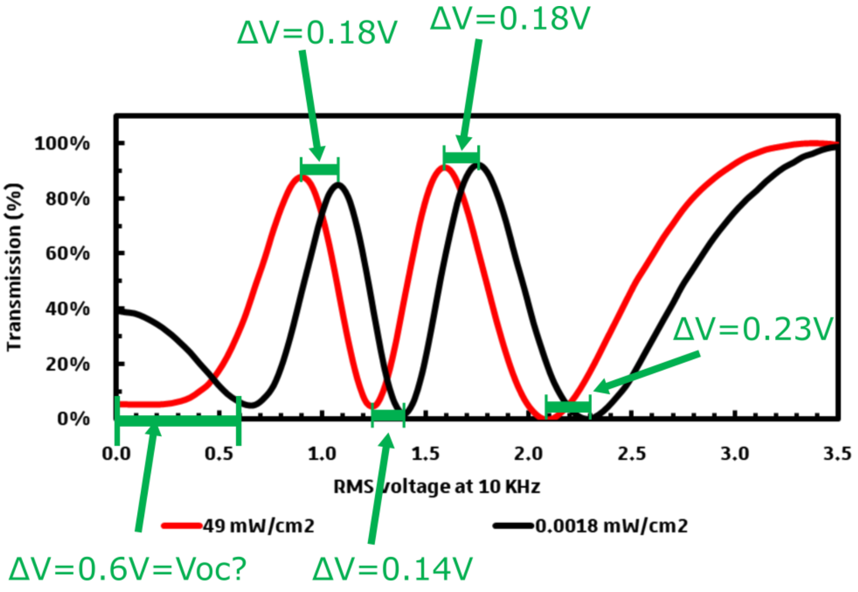

Figure 67: CPI measurement of an ITO/P3HT:PCBM (1:1)/E7/PEDOT:PSS/ITO OASLM at different light intensity as specified on the graph (λ = 532 nm).

We observe different RMS voltage shift (ΔV) values between the two curves of 0.6 V, 0.18 V, 0.14V, 0.18V and finally 0.23V with increasing RMS voltage. However, at 0V, it seems to be close to the photovoltage produced by a P3HT:PCBM photovoltaic cell (ΔV = Voc = 0.6V). To better understand this behaviour, which seems complex at first, one needs to reformulate the observation differently:

"The DC offset (Voc) does not induce a constant shift between the CPI curves as a function of a sinusoidal RMS voltage."

One then becomes aware of a common mistake of first year's students in electronics: The addition of a 1 V DC offset to a sinusoidal voltage of 1 V_{RMS} is 2 V_{RMS} (which is of course false!). This is our starting point, and to explain the observations further, we make the following assumptions:

1. When the LC cell is short-circuited (i.e. at 0V), the photovoltaic layer is in quasi open-circuit conditions as it is "connected" in series with the LC impedance, which is considerably larger than the P3HT:PCBM impedance.
2. All AC and DC potential differences are dropped across the LC layer.
3. An "effective RMS voltage" that leads to the observed shift in CPI curves can be calculated with the following formula:

$$V_{RMS} = \sqrt{{V_{DC}}^2 + \frac{{A_1}^2}{2}}$$

Where V_{DC} is the photo-voltage and A_1, is the amplitude of the AC voltage applied by the function generator. It is important to note that when the amplitude of the applied sinusoidal voltage is very large in front of the photovoltage, we can neglect the small photogenerated DC bias and V_{RMS} is approximately equivalent to the applied sinusoidal voltage:

$$V_{RMS} \approx \frac{A}{\sqrt{2}}$$

In order to estimate the DC voltage, we need a boundary condition or reference value. In the present case, I had to assume that at the lowest light intensity the photogenerated voltage is negligible. At higher light intensity, the total phase shift at 0V decreases. This phase shift is equivalent to the one observed at low light intensity at a higher AC voltage. The corresponding voltage shift (Voc) has been plotted as a function of light intensity for the P3HT:PCBM sample with a (1:1) weight ratio on Figure 68.

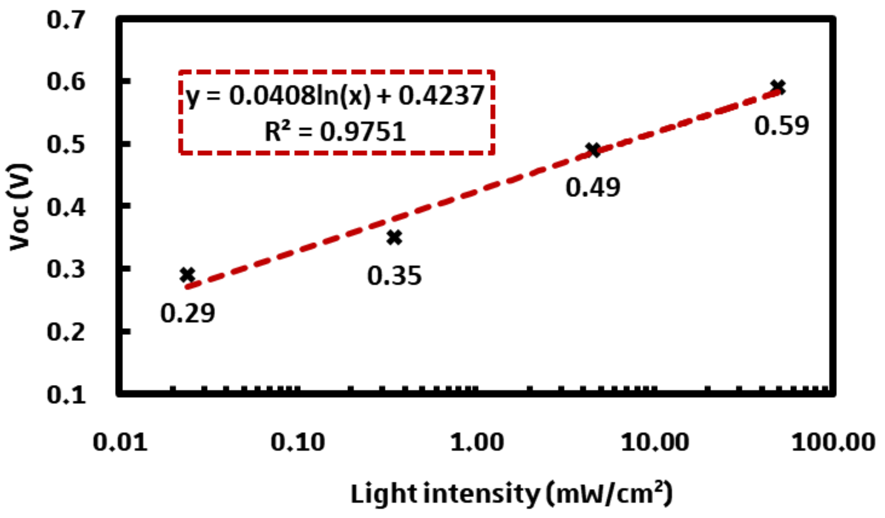

Figure 68: Voltage shift (Voc) as a function of light intensity estimated from the optical measurement.

The measured Voc value varies logarithmically with the light intensity, as would be expected for a photovoltaic device. It also tends to indicate that the photogenerated voltage is mostly dropped across the LC bulk. These Voc values were used to correct the voltage shift induced by the P3HT:PCBM layer upon illumination on the CPI curves, as depicted in Figure 69.

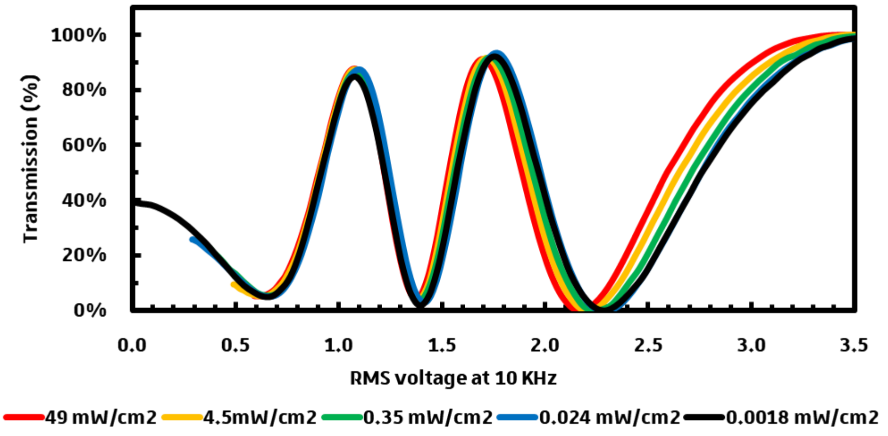

Figure 69: Fitted CPI curves to estimate the photovoltage generated by the photovoltaic layer. OASLM structure: ITO/P3HT:PCBM (1:1)/E7/PEDOT:PSS/ITO

We can observe that the fit is valid in the low voltage part as the CPI curves superpose almost perfectly in this region. However, at higher applied AC bias, the curves do not superpose anymore. It is known that the electrical impedance of a solar cell under open circuit conditions decreases with increasing light intensity [112]. We may therefore expect that an additional light intensity dependent attenuation of the AC voltage is responsible for the poor fit observed at high voltages.

Since the photovoltage is independent of the AC voltage and has already been taken into account, the residual shift in CPI curves with increasing AC voltage can be used to estimate the light-induced voltage attenuation. The attenuation versus voltage curve is obtained by comparing the CPI curves measured at the lowest (0.0018 mW/cm^2) and highest light intensities (49 mW/cm^2) and is depicted in Figure 70.

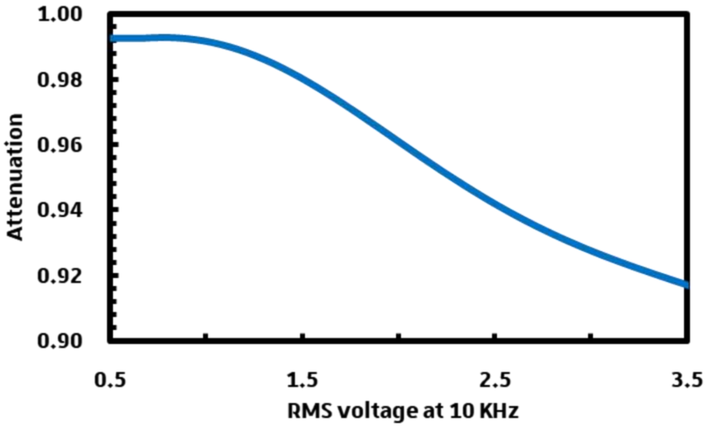

Figure 70: Attenuation induced by the P3HT:PCBM (1:1) at low light intensity layer as a function of applied AC bias (blue line, left).

At 49 mW/cm^2, the impedance of the PCL is negligible. Therefore, all the potential is dropped across the LC layer. On the other hand, at 0.0018 mW/cm^2, the impedance of the PCL is non-negligible and attenuates the voltage drop across the LC layer. As the LC molecules reorient with increasing AC voltage, the impedance of the LC layer decreases. This attenuates even more the voltage drop across the LC layer with increasing AC bias as more potential is dropped across the P3HT:PCBM layer. Therefore, the attenuation value decreases with applied AC bias as shown in Figure 70.

This simple method used above to explain the voltage shifts observed with a P3HT:PCBM layer, indicates that at least two effects modify the shape of the CPI curves upon illumination. First, the photovoltage that increases logarithmically with increasing light intensities. Second, the impedance that decreases with increasing light intensities. In addition, it shows that the photogenerated bias is mainly dropped across the whole LC bulk. Indeed the extracted Voc corresponds to the one of an optimized P3HT:PCBM photovoltaic solar cell. At this stage, it is important to point out that this photovoltage is obtained despite the fact that the structure does necessarily possess the appropriate interfaces to favour charge separation. It is also worth mentioning that the impact of the photovoltage on the birefringence may be dependent on the LC molecule pretilt angle at the PCL/LC interface.

6.3.4 Measurement of the angle of pretilt

It is well known that the tilt angle formed by the LC molecules at the substrate surface strongly influences the electro-optical properties of a LC cell [113]. Therefore, a small pretilt is sometimes desirable to decrease the threshold voltage or shorten the response time of a LC cell. Several methods exist to estimate the pretilt angle of a LC cell such as for instance the crystal rotation method [114], [115]. In addition, it is known that applying a surface treatment with UV exposure or O_2 plasma to the polyimide alignment layers increases the surface polarity and decreases the pretilt angle of LC molecules [116] [117]. It implies that the pretilt angle is strongly related to the surface energy of the material in contact with the LC molecules. Consequently, the contact angle of a drop of water with the alignment substrate is a good indicator for the LC pretilt angle value. Table 2 lists the evolution of the LC pretilt (θ_p) as a function of the surface contact angle with water (θ_a) as reported in reference [117].

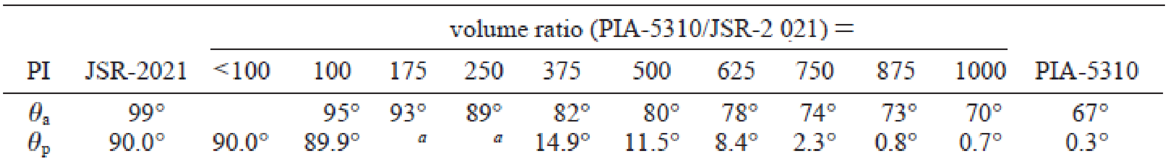

		volume ratio (PIA-5310/JSR-2 021) =										
PI	JSR-2021	<100	100	175	250	375	500	625	750	875	1000	PIA-5310
θ_a	99°		95°	93°	89°	82°	80°	78°	74°	73°	70°	67°
θ_p	90.0°	90.0°	89.9°	[a]	[a]	14.9°	11.5°	8.4°	2.3°	0.8°	0.7°	0.3°

Table 2: Contact angles of water (θ_a) and corresponding Pretilt Angles (θ_p) of liquid crystal (5CB) on the surface prepared from mixing two polyimides: the hydrophilic PIA-5310 and the hydrophobic JSR-2021 at various ratios. Reproduced from [117].

If the contact angle measured with a water droplet increases, the pretilt angle formed between the substrate and the polar liquid crystal should increase as well. We therefore performed contact angle measurements on different types of substrates as a function of light intensity. These measurements were done by Nicolas Zimmermann. His report, which is available in the appendix, leads to the following conclusions:

- PEDOT:PSS (Clevios PH) deposited on ITO displays a low contact angle (<15°) This material is therefore expected to induce a low pretilt angle (near 0°) and a good planar alignment. This has been confirmed by the CPI measurements on a LC cell with PEDOT:PSS as AL on both sides (see section 4.3.1).
- All the P3HT:PCBM layers with the following mass ratios (1:0), (1:0.01), (1:0.5) and (1:1) showed high contact angles (>100°). For this reason, we expect LC molecules to have a high pretilt angle at the P3HT interface. Besides, we do not observe significant variations of the surface contact angle with water as a function of light intensity. We may therefore conclude that the latter mechanism does not contribute to the observed light-induced changes in birefringence.

In addition to the contact angle measurements [114], [115], the crystal rotation method was used by Nina Podoliak at the Southampton University. This method is more precise to determine the pretilt angle of LC cells than the contact angle measurement. A good description of this experimental method is available in Andrew Acreman thesis [118]. Her experimental results and conclusions are given in the appendix. We can summarize the results as follows:

- Cells containing a layer of PEDOT in contact with the LC molecules display small pretilt angle (near 0°).

- The cells containing P3HT:PCBM in contact with the LC molecules displayed high pretilt angle. In addition, for the cell containing P3HT:PCBM at 1:1 ratio, the pretilt angle increases with increasing light intensities.

The latter experiment, which does not rely on the application of a voltage (the ITO plates are disconnected during the measurement), may thus indicate that a pretilt angle variation may still contribute to the electro-optic response of the cell. Such a behaviour might be induced by the presence of soluble fullerene derivative in the PCL. Indeed, it has been reported that fullerene is soluble in the E7 liquid crystal mixture [119] (this observation was done after stirring the E7:PCBM mixture at 100°C.) Therefore, even at room temperature, there might be a risk of partial dissolution of the fullerene derivative into the LC mixture, affecting its behaviour at the PCL/LC interface.

This observation also emphasises the potential interest of adding an interfacial layer between the PCL and the LC layer in order to avoid the risk of an uncontrolled dissolution of PCBM into the LC.

Finally, since three different mechanisms contribute to the LC reorientation: (1) the photovoltage, (2) the impedance variation and (3) the pretilt angle of the LC, it is not possible at this stage to conclude which one of these has the most impact on the cell performances.

6.3.5 Diffraction efficiency

In order to estimate the potential of the P3HT:PCBM (1:1) OASLMs in holographic applications, we measured its diffraction efficiency. In this experiment, a Laser beam (λ = 532 nm, 24 mW/cm^2 each), also referred to as pump beam, is split into two coherent beams that subsequently interfere on the OASLM, as illustrated in Figure 71 and Figure 72. The beam interference creates a sinusoidal light intensity grating on the photoconductor that translates into the refractive index grating (periodic change of the liquid crystal birefringence).

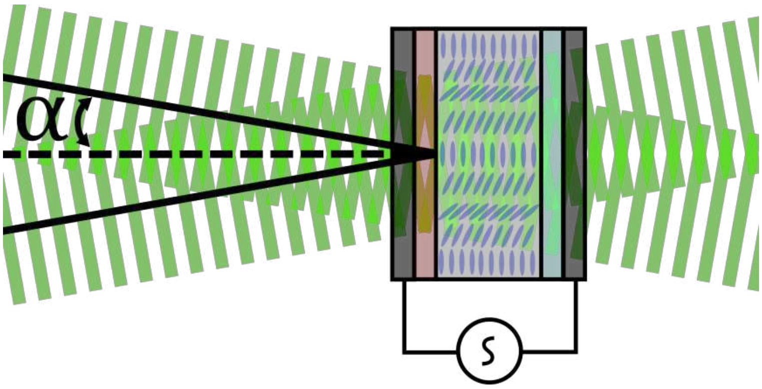

Figure 71: Sinusoidal light intensity grating formation by two lasers beam translated in the OASLM by a sinusoidal refractive index grating.

To change the period Λ of the interference pattern, the angle formed by the two beams can be tuned according to the following:

$$\Lambda = \frac{\lambda}{2\sin(\alpha)}$$

where λ is the pump beam wavelength. The resulting sinusoidal refractive grating is probed using a second laser beam of a different wavelength (λ = 633 nm at 13 mW/cm2), referred to as probe beam. The measurement setup is schematized Figure 72.

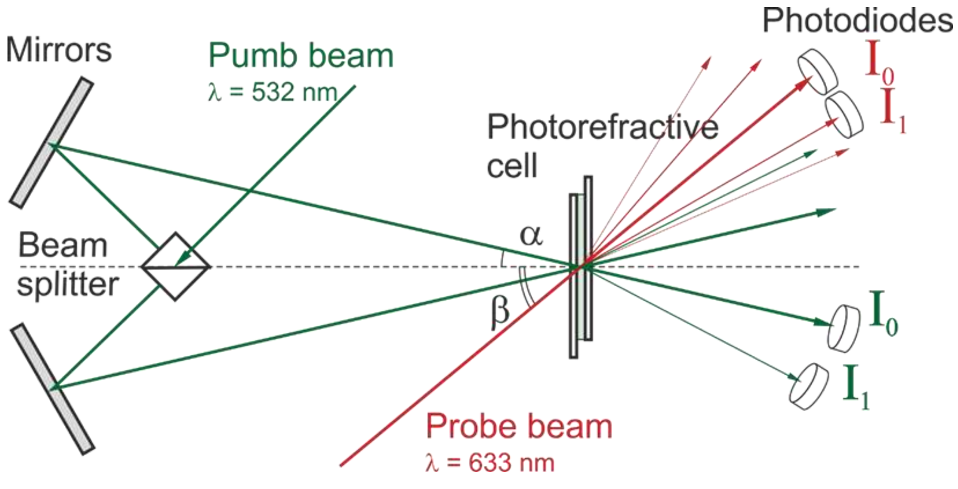

Figure 72: Diffraction efficiency setup

When the probe beam encounters the refractive index grating formed by the pump beam, the light diffracts into several orders. The diffraction efficiency η is defined as follows:

$$\eta = \frac{I_1}{I_0}$$

where $I_{0,1}$ are respectively the intensities of the fundamental and first diffracted order.

This is a simplified description of the experiment and more advanced details on the measurement theory can be found in the following documents [120] [121]. In our experiment, the grating spacing was set to $\Lambda = 9.4\ \mu m$ which is equivalent to a spatial resolution of 106 lp.mm^{-1}.

The measured diffraction efficiency was null when the function generator output was off (OASLM ITO plates disconnected). However once the output of the function generator was set to on (OASLM ITO plates connected but without applying a voltage), the first diffracted order could be measured. The diffraction efficiency versus applied AC voltage (10 kHz) is depicted in Figure 73 for a P3HT:PCBM cell with a (1:1) weight ratio.

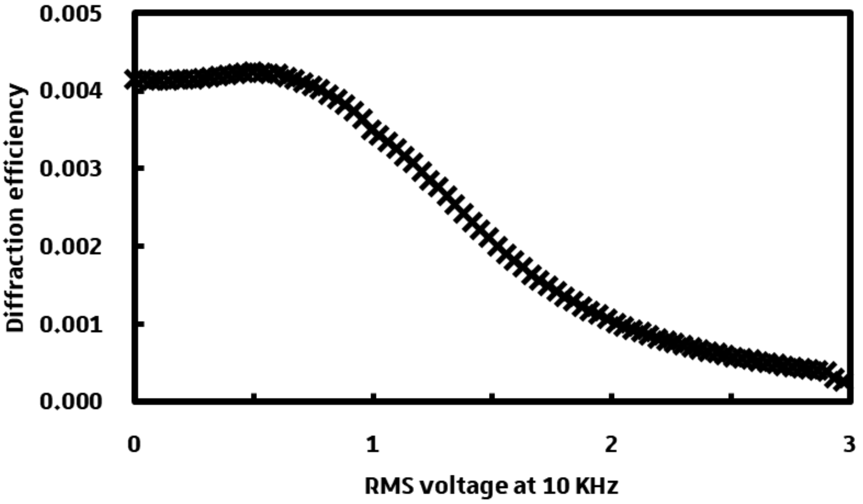

Figure 73: Diffraction efficiency of an ITO/P3HT:PCBM (1:1)/E7/PEDOT:PSS/ITO.

The measured diffraction efficiency at 0V (0.4%) is rather low in comparison to state of the art OASLMs (see chapter 3). It slightly increases with applied AC bias before decreasing at higher voltages.

It is important to note that in this experiment the probe beam (λ = 633 nm, 1.96 eV) is absorbed by the P3HT:PCBM layer (bandgap of 1.9 eV), and may therefore affect the grating induced by the pump beam and decrease the efficiency. Yet, the results obtained on such un-optimized configuration show that our device could achieve a better resolution than most inorganic semiconductors.

6.4 Conclusion

The results obtained on the P3HT:PCBM OASLM structures are encouraging as we showed that these devices can spatially modulate light without applied voltage. The rather low diffraction efficiency and corresponding resolution indicate that the P3HT:PCBM has a higher surface resistivity than inorganic semiconducting crystals. More importantly, the negligible threshold voltage permits to control the cell without externally applied voltage.

Several drawbacks can however be identified which require this structure to be further improved. We do not control the PCL/LC interface and we lack control on important parameters such as the pretilt angle, also fullerene might dissolve in the LC mixture over time. Rubbing the P3HT:PCBM layer might induce anisotropic optoelectronic properties. Finally, the control of the interfaces surely defines the behaviour of the P3HT:PCBM photosensitive layer: photoconductive or photovoltaic. For all those reasons, we chose to deposit an additional PEDOT:PSS layer on top of the P3HT:PCBM layer. As will be shown in the next chapter, such a structural modification affects all the parameters listed above.

7 Impact of interfacial layers

In this section, we used an additional interfacial layer of PEDOT:PSS between the photovoltaic layer and the LC layer. It should decrease the pretilt angle at the PCL/LC interface. We will study two different structures: In the first structure, the P3HT:PCBM layer will be comprised between two ohmic PEDOT:PSS electrodes which should yield a photoconductive OASLM. In the second structure, we will replace the PEDOT:PSS layer at the ITO/P3HT:PCBM interface by a thin PEIE layer in order to enhance the photovoltaic effect.

7.1 PEDOT:PSS as an interfacial layer between the PCL and the LC.

In order to deposit PEDOT:PSS on top of a P3HT:PCBM film, a specific formulation needs to be used. Indeed PEDOT:PSS is an aqueous formulation which cannot be deposited on top of a hydrophobic layer such as P3HT. Therefore, we need to use a specific PEDOT:PSS formulation, such as Clevios™ CPP 105D. When spin-coated on top of P3HT:PCBM, the adhesion and mechanical hardness of this PEDOT:PSS needs to be sufficient to avoid subsequent damages or delamination during the rubbing process.

The surface resistivity of the CPP 105D is rather low with a sheet resistance of $10^4\ \Omega/sq$. This value is four orders of magnitude lower than the surface resistivity of semi-insulating inorganic crystals such as GaAs. Consequently, it will affect negatively the OASLM resolution. Fortunately, the properties of PEDOT:PSS such as adhesion, mechanical hardness and sheet resistance can be adjusted using different formulations as depicted Figure 74.

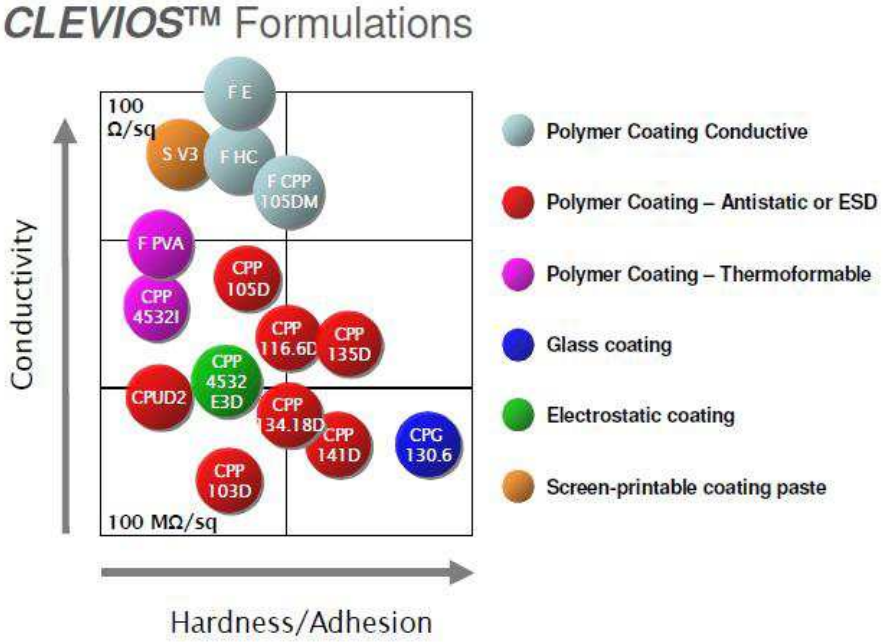

Figure 74: Clevios™ formulations reproduced from [85].

The CPP 105D formulation is mixed with N-Methyl-2-pyrrolidone (NMP), a high boiling point solvent which increases the conductivity and modifies the morphology at the surface. The more hydrophilic and conductive PEDOT tends to segregate to the surface, giving rise to a low resistivity and high contact angle (<53°, see appendix) when deposited on top of the P3HT. LC Cell with the following structures ITO/P3HT:PCBM/CPP 105D display a low pretilt angle (near 0°), as estimated by crystal rotation measurements (see appendix).

To study the impact of this interfacial layer on the OASLM response, the P3HT:PCBM weight ratio was kept constant (1:1). Two different OASLM structures will be used. The first OASLM structure is composed of a P3HT:PCBM layer comprised between two PEDOT:PSS layers. As we will see below, this device behaves as a photoconductor-type OASLM.

In the second type of OASLM, the PCL will be comprised between two electrodes with different work functions: A ITO modified electrode with a thin layer (7 nm) of PEIE (W_F = 3.6 eV [94]) and CPP 105D PEDOT:PSS (WF = 4.7 eV [122]). This device will be called “photovoltaic OASLM” for reasons that will become clear below.

Both structures with a photoconductive layer (PCL) and a photovoltaic layer (PVL) are depicted in Figure 75.

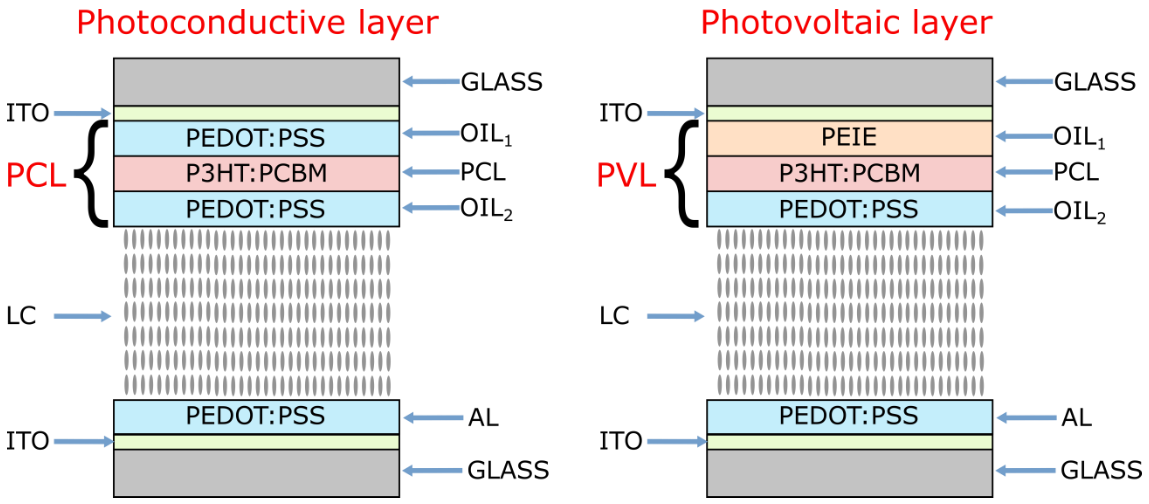

Figure 75: Schematized OASLM structure using a PCL (left) and a PVL (right)

All LC cells were filled with the E7 mixture. PEDOT:PSS is used as the alignment layer on both sides of the LC.

The wavelength of the light used for all the CPI or VTF measurements was 532 nm. The E7 total birefringence (0.235) value is used to deduce the thickness of the different LC cells.

7.2 OASLM with P3HT:PCBM used as photoconductive layer

In this experiment, we used a thin layer of P3HT:PCBM (1:1) sandwiched between two PEDOT:PSS layers. The CPI response of this sample at 10 kHz and at two different light intensity of 0.0045 (dark dot) and 9.9 mW/cm² (red line) is depicted in Figure 76.

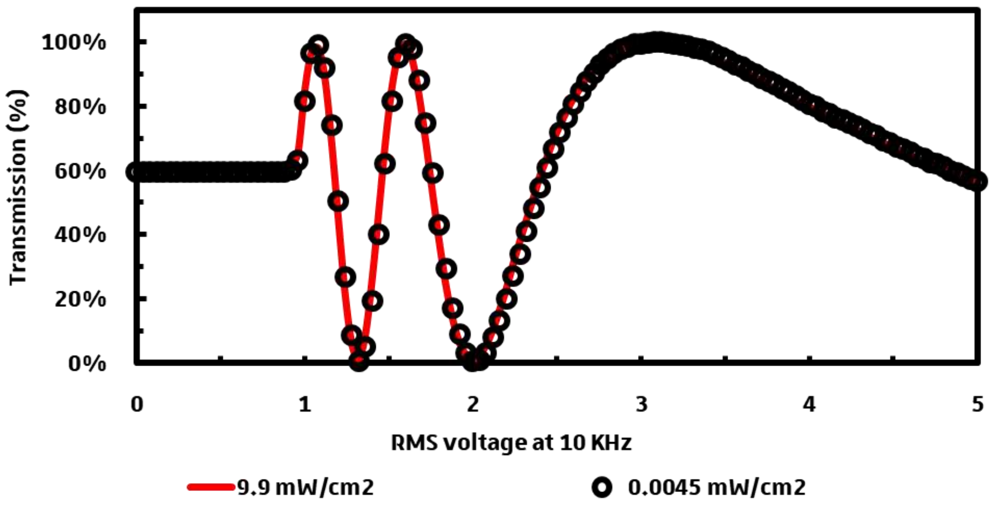

Figure 76: CPI measurement of an ITO/Clevios PH/P3HT:PCBM (1:1)/CPP 105D/E7/ Clevios PH/ITO OASLM at different light intensities as specified on the graph (λ = 532 nm).

The OASLM does not display any variation upon varying light intensity. The threshold voltage is, as expected, close to 1V, which indicates a planar alignment of the LC molecules on both sides thanks to the addition of the more hydrophilic layers.

The absence of a light-induced shift in the CPI response suggests that the thin organic film comprised between both PEDOT:PSS layers (which behave as ohmic contacts, see below) does not induce any modification of the LC birefringence under illumination. At this point, I would like to point out that the ohmic nature of the contacts may strongly affect the dark conductivity of the organic blends, as recently reported by Blom et al. [123] To better understand the impact of ohmic contacts, I will present shortly below an investigation of the photoconductivity P3HT:PCBM with different interface layers.

7.2.1 Photoconductivity of P3HT:PCBM

When a thin P3HT:PCBM layer is comprised between ohmic contacts, also referred as symmetrical structure, an ohmic behaviour should be observed at least at low voltage, when the dielectric relaxation time is shorter than the transit time of injected charges (i.e. before space charge may build up). In other words, the current-voltage characteristic should follow Ohm's law (U = RI) at low voltage. If the charge carrier density is sufficiently low and if, the charge generation by absorbed light is efficient. The device should behave as a photoconductor (high dark resistance and with increasing light intensity decreasing resistance).

To investigate the photoconducting properties of P3HT:PCBM blends, films with different polymer/fullerene weight ratios were comprised between two ohmic contacts : glass/ITO/PEDOT:PSS was used as substrate and bottom electrode, while a bilayer of molybdenum oxide (MoO_3) and 120 nm thick silver layer was evaporated on top and served as the second electrode. The photoconductor area was set to 9 mm^2 by the shadow mask. It should be noted that I did not use PEDOT:PSS as the top layer as this would not allow me to control easily the device area.

The current vs voltage (I-V) curves were measured under dark conditions and at 100 mW/cm^2 illumination (AM 1.5). The sample showing the highest relative change in resistance ($\frac{\Delta R}{R_0}$) was obtained with a 100 nm thick P3HT:PCBM (1:0.01) layer and is displayed in Figure 77.

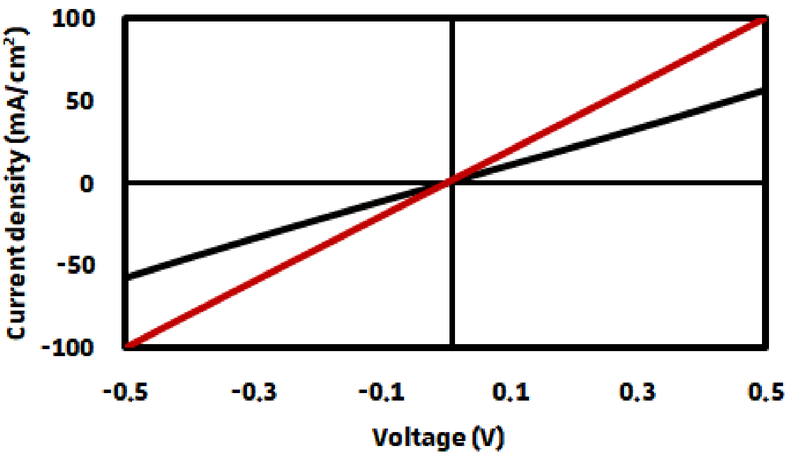

Figure 77: I-V measurements of an ITO/PEDOT:PSS/P3HT:PCBM(1:0.01)/MoO3/Ag, under dark conditions(dark slope) and one sun illumination (AM 1.5, red slope).

The resistance increases from 55 Ω, under illumination, up to 94 Ω under darkness $\frac{\Delta R}{R_0} = 40\,\%$. The corresponding surface resistance of the PCL under illumination ($R_{PCL,Light}$) and dark conditions ($R_{PCL,Dark}$) are $R_{PCL,Dark} = 8.5\,\Omega.cm^2$ *and* $R_{PCL,Light} = 4.5\,\Omega.cm^2$. If this PCL were put in series with the LC cell whose surface is equal to 3.6 cm², the PCL series impedances values would be respectively $R_{PCL,Dark} = 2.4\,\Omega$ *and* $R_{PCL,Light} = 1.4\,\Omega$. Such a small difference in series resistance is clearly insufficient to influence the potential distribution across the OASLM device and can therefore not be probed optically. For the other samples at different P3HT:PCBM weight ratios, the order of magnitude of the dark resistance is between 40 and 100 Ω. This leads us to the following question. Why is the dark resistance value of P3HT:PCBM PCL so low?

Obviously, the background charge carrier density is too high. The latter value can be probed with the same devices by driving them into the “space-charge-limited current” (SCLC) regime. Indeed, with increasing voltage, the number of carriers injected at the electrodes becomes significantly higher than the intrinsic carrier density. Consequently, the injected charges can no more be screened by the background conductivity. In such a case, the current is space charge limited and follows the Mott-Gurney law [124]. SCLC measurement technique was set-up by Sadiara Fall [125] It allows to extract the charge carrier mobility and the background carrier density from the IV curves. The mobility extraction procedure is described in the appendix.

I used the SCLC technique to estimate the charge carrier density and hole mobility in P3HT layers as a function of the semiconductor layer thickness.

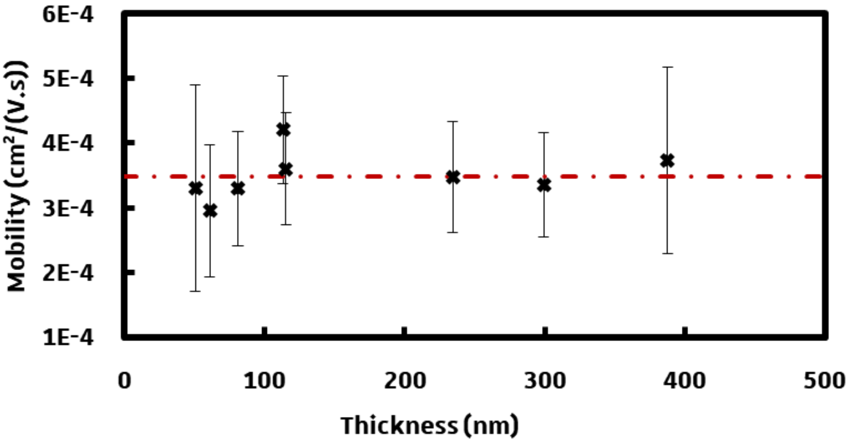

Figure 78: P3HT mobility (SCLC) as a function of thickness

As expected, the measured hole mobilities of P3HT, which is depicted in Figure 78 (dark cross), does not vary as a function of film thicknesses. The average hole mobility (red dashed line) is $\mu_h = 3.5 \times 10^{-4} cm^2.V^{-1}s^{-1}$. These values were then used to deduce the charge carrier density (dark cross) as a function of thickness from the ohmic part of the SCLC curves (see Figure 79).

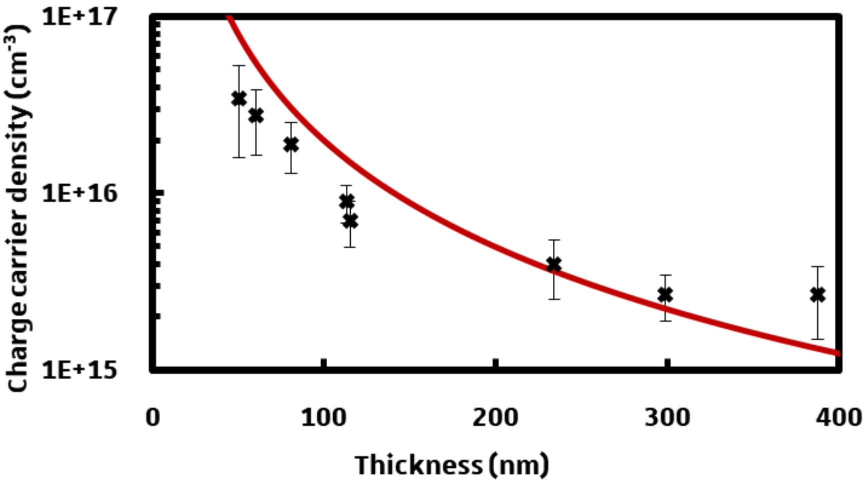

Figure 79: Charge carrier density deduced from SCLC ohmic part. Experimental data points (dark cross) and theoretical charge carrier density $p_0 = \frac{4\pi^2 kT\varepsilon}{q^2L^2}$ *[123] (red line)*

We can observe that the charge carrier density is thickness dependent. This effect is well-known and has been extensively discussed in the literature [126]. It is the outcome of charge carrier diffusion from the ohmic contact into the semiconductor. More recently, Blom et al. [127] derived the effective density of accumulated charge carriers p_0 due to charge carrier injection from ohmic contacts [123]. They found that:

$$p_0 = \frac{4\pi^2 kT\varepsilon}{q^2 L^2}$$

This equation is compared in Figure 79 (red line) with our experimental results. Although the fit is not perfect, both results follow the same trend and can be used as a guide to estimate the thickness beyond which the charge carrier density is controlled by charge diffusion from the contacts rather than by the concentration of (background) dopants. The latter should be equal to the charge carrier density observed for the highest film thicknesses, where the impact of charge diffusion levels out.

The experimental results shown in Figure 79 indicate further that background-doping density of P3HT is significant (around $2x10^{15}$ charges.cm^{-3}). It is in particular six orders of magnitude higher than Semi-insulating GaAs [128]. In other words, pristine P3HT has a low dark resistance and will not be a good photoconductor.

In semiconductors the number of free charge carrier is thermally activated, however, due to the low dielectric constant of organic materials, the fraction of ionized dopant should be significantly less than unity. Organic semiconductors are therefore less sensitive to dopants, which implies that with apparent doping density of $2 \times 10^{15}\ charges.cm^{-3}$ at room temperature, the actual number of impurities is probably some orders of magnitude higher [129]. N-type dopants such as Cobaltocene ($CoCp_2$) have been used to compensate p-type P3HT, in order to decrease its dark conductivity [130]. However, for films as thin as 100 nm, the ohmic-contact induced doping is difficult to avoid, making such a structure inappropriate for photoconductive OASLM devices.

7.3 Selection of appropriates interfaces

Unlike inorganic crystals, there is no Semi-insulating (i.e. with a low charge density) P3HT available on the market. Further processing steps are required to control the doping density [130]. In addition, as pointed out above, the charge carrier density is also controlled by the contact at the interface. High work function electrodes such as PEDOT:PSS increase the apparent hole density in P3HT due to electron transfer from P3HT to PEDOT:PSS. Even by compensating p-type P3HT to decrease its charge carrier density and diminish the impact of charge carrier diffusion from the contacts, a thick layer that affects the device transparency would be required.

On the other hand, electrodes with low work function such as calcium (Ca) induce an electron transfer from Ca to p-type P3HT [131]. We can make an analogy with the well-known Schottky barrier [31] used to increase the photosensitivity of ZnO NPs photodiodes. Comprising the P3HT:PCBM (1:001) layer between symmetrical low work function metals may be a possible way to decrease the hole density in the PCL layer.

The I-V curves of a 370 nm thick P3HT:PCBM (1:0.01) diode comprised between two aluminium contacts (ITO/Al(14 nm)/P3HT:PCBM/Al(120 nm), measured under dark conditions (dark line) and at 100 mW/cm^2 illumination (AM 1.5) (red line), are shown in Figure 80.

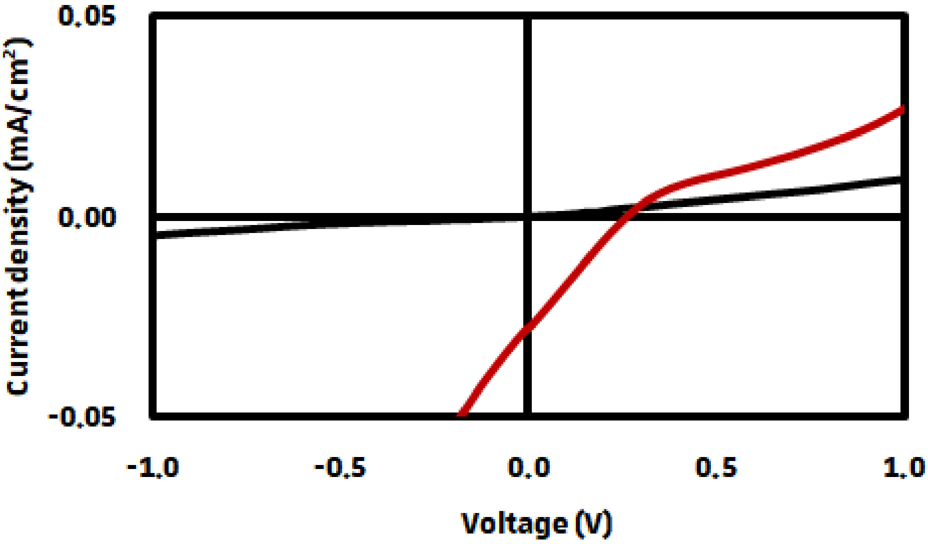

Figure 80: Dark (dark line) and light (100 mW/cm2 AM 1.5, red line) current vs voltage curve of a P3HT:PCBM (1:0.01) diode (9 mm²) comprised between aluminium contacts.

We observed that the dark current decreases by 5 orders of magnitude (taking into account the thickness variation) relative to the device with ohmic contacts. However, under illumination, the behaviour is non-linear, non-symmetric and includes a short-circuit current and an open-circuit voltage. The latter two parameters point out that photo-induced charge can be separated. A possible origin of this effect may be the existence of dissymmetric contact properties. Indeed the bottom Al electrode may have been oxidized before the deposition of the organic layer (even though this step was done in a N_2 filled glove box with a background O_2 concentration of the order of a ppm).

As a matter of fact, the “photosensitivity” of a P3HT:PCBM layer can be enhanced dramatically if it is comprised between dissymmetric contacts that act as selective electrodes for electrons and holes. In such a case, the free charges carriers can be separated without applying an external bias. As a result, an electric current flows and a photovoltage appear across the P3HT:PCBM layer. The maximum photovoltage is achieved under open circuit conditions (i.e. when no current is flowing). It has been shown that the V_{OC} depends on the electrochemical properties of the D and A materials [132]. Higher V_{OC} can be achieved for instance by pairing P3HT with indene-C60 bisadduct (ICBA, $V_{OC} = 0.84V$ [133]) instead of

PCBM (V_{OC} = 0.62 V). The layer sequence ITO/PEIE/bulk heterojunction/MoO3/Ag) has been extensively used to build organic photovoltaic cells. A typical J-V curve of such a P3HT:PCBM solar cell is depicted in Figure 81 under darkness (dark line) and under 100 mW/cm^2 illumination (AM 1.5) (red line). A similar structure will be used below to build a "photovoltaic OASLM", with the exception that the MoO3/Ag bilayer is replaced by a PEDOT:PSS layer. Both layers are appropriate for collecting holes that are photo-generated in the bulk heterojunction under illumination.

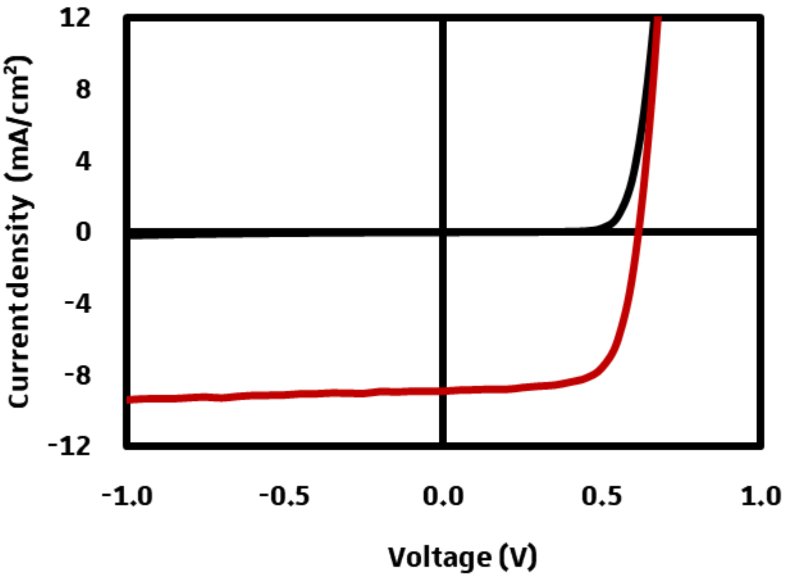

Figure 81: Dark (dark line) and light (100 mW/cm^2 AM 1.5, red line) current vs voltage curve of a P3HT:PCBM (1:1) diode (12 mm2) comprised between ITO modified PEIE (7 nm) and MoO3 (7 nm)/Ag (120 nm). Voc = 0.615 V, J_{SC} = 8.9 mA/cm^2, FF = 70% and η = 3.8 %.

To conclude, the dark conductivity of a 100 nm thick P3HT:PCBM film comprised between ohmic contacts (i.e. high WF conductors) is increased significantly by charge diffusion from the contacts. Using low work function contacts reduces this effect, although we could not produce a symmetric device. In the end, the layer sequence that provides the best photosensitivity is the one corresponding to a photovoltaic cell. With that in mind, a layer sequence composed of dissymmetric electrodes (for instance a low WF material/bulk heterojunction/high WF material) would be a better option. With the first models of OASLM discussed in section 6, we showed the occurrence of a photogenerated DC bias that could be used to control the LC layer orientation in a reproducible manner. The non-symmetric layer sequence used in these devices (i.e. ITO/BHJ/LC) was sufficient for spontaneous charge separation. However, the photovoltaic effect can still be optimized by inserting additional interfacial layers, such as a thin PEDOT:PSS layer between the BHJ and the LC and a PEIE between ITO and the BHJ. The top PEDOT:PSS layer should also improve the LC alignment and avoid damaging the photosensitive layer during the rubbing process.

7.4 OASLM with P3HT:PCBM used as photovoltaic layer.

In the following experiments, we substituted the PEDOT:PSS layer located between ITO and P3HT:PCBM (1:1) by a thin (~7 nm) PEIE layer and kept the top PEDOT:PSS layer as the alignment layer. The CPI response of such an OASLM measured at an AC frequency of 100 Hz is depicted in Figure 82. The LC gap thickness was approximately 7.3 µm. A green laser (λ = 532 nm) was used as light source and its intensity varied from 0.17 mW/cm² to 89 mW/cm².

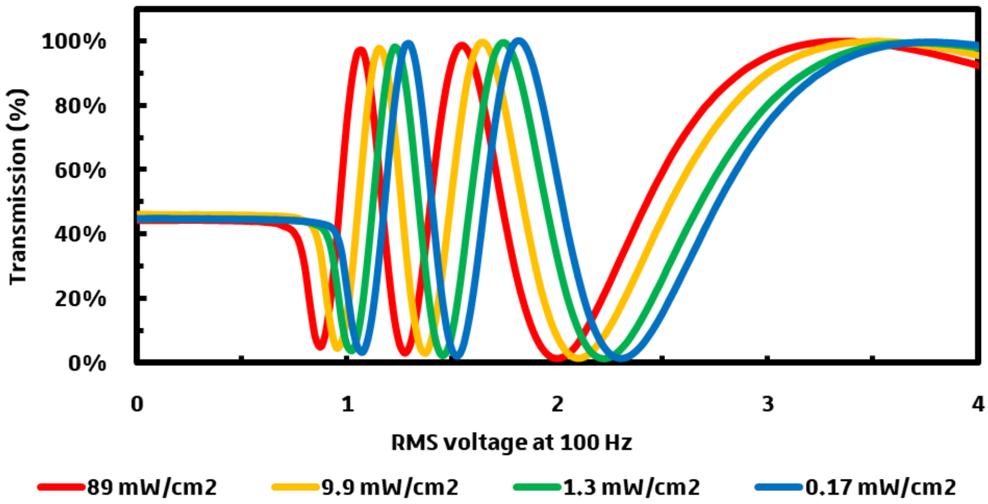

Figure 82: CPI measurement of an ITO/PEIE/P3HT:PCBM(1:1)/CPP 105D/E7/PEDOT:PSS/ITO OASLM at different light intensity as specified on the graph (λ = 532 nm).

The cell response is seen to vary as a function of light intensity. All curves shift to the left with increasing light intensity. Additionally, the curves display a marked threshold voltage, which decreases with increasing light intensities. At 89 mW/cm², the threshold voltage is lower than the value measured on an OASLM using a photoconductor structure (symmetric interfacial layers).

These observations are however not sufficient to demonstrate that a photovoltaic effect induces the birefringence change. The weak threshold voltage change may eventually be an outcome of the P3HT:PCBM photoconductivity. If this would be the case, we would expect the difference in voltage drop across the LC layer between low and high light intensity, to decrease with increasing AC voltage. Indeed, as the LC molecules reorient, its impedance decreases (see section 5.2.1.1). However, as pictured in Figure 83 that superposes the low and high-intensity CPI curves, the attenuation increases (see section 5.2.1.1) with applied voltage. This would indicate that with increasing AC voltage, the LC layer impedance increases, therefore less potential is dropped across the P3HT:PCBM photoconductor and more potential across the LC layer, which is absurd.

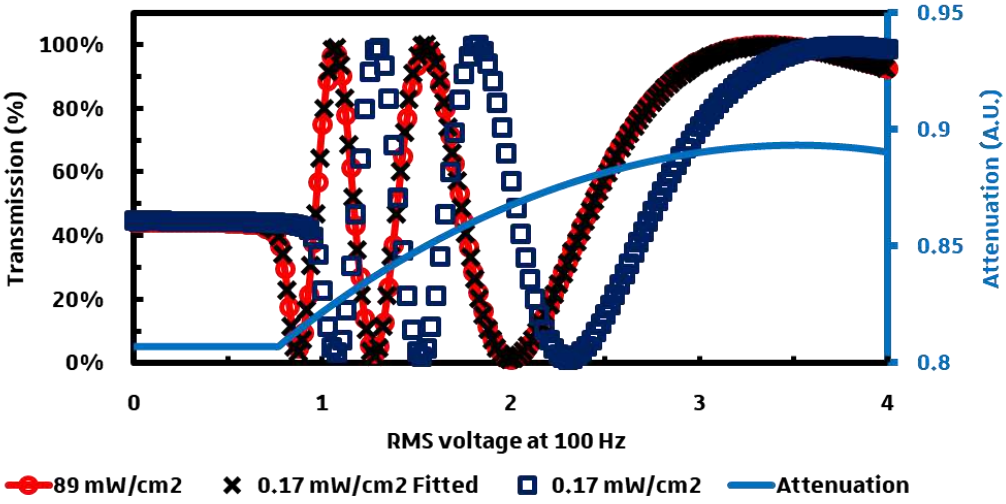

Figure 83: CPI measurement of an ITO/PEIE/P3HT:PCBM(1:1)/CPP 105D/E7/PEDOT:PSS/ITO OASLM at two different light intensity (89 mW/cm² red line and 0.17 mW/cm² blue square, λ = 532 nm). The attenuation value increases with applied voltage (blue line). The low light intensity curve is superposed to the high light intensity curve using the attenuation curve (dark cross).

On the other hand, the method developed in section 6.3.3 to estimate optically the DC voltage generated by the BHL layer can be used as well in the present case. The first step is to estimate the effective photovoltage that is dropped across the LC layer using the following equation:

$$V_{RMS} = \sqrt{{V_{DC}}^2 + \frac{A^2}{2}}$$

To determine V_{DC} the high-intensity curve is shifted by V_{RMS} so that it overlaps with the low-intensity curve (for which V_{DC} is assumed to be negligible). The results are depicted in Figure 84, the high-intensity CPI curves (red line, red circle) was corrected to make both curves overlap in the low voltage region. A dark line depicts the pristine experimental results of the CPI curve at the lowest light intensity used as a reference.

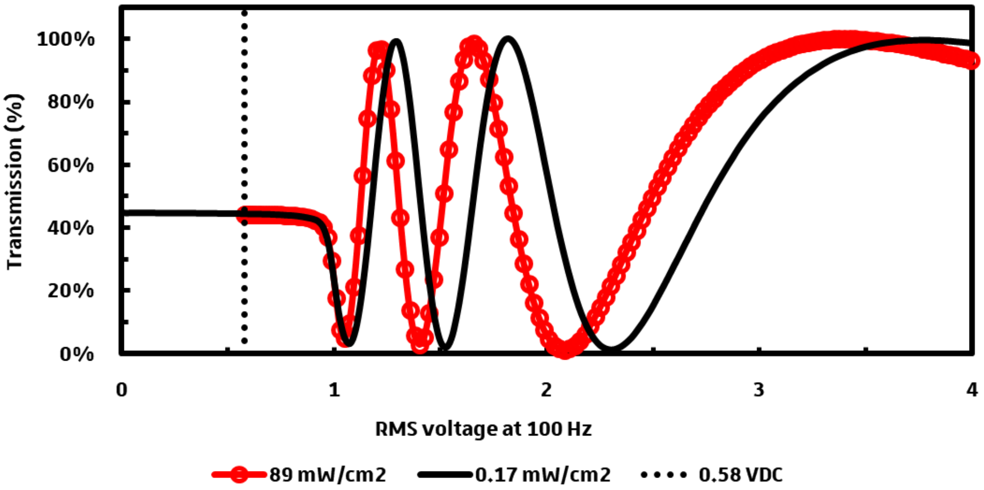

Figure 84: Estimated photovoltage deduce from the optical measurements of an ITO/PEIE/P3HT:PCBM(1:1)/CPP 105D/E7/PEDOT:PSS/ITO OASLM.

The corresponding DC voltage induced by the PV layer is estimated to 0.58 V, which is close to the open circuit voltage that we could expect from a P3HT:PCBM photovoltaic cell. Again, the difference at higher applied AC voltage can be explained by the additional impedance variation of the photovoltaic layer.

Both, the good agreement between the DC voltage and the open-circuit voltage of a related solar cell as well as inconsistent voltage drop discussed above, corroborate the conclusion that the P3HT:PCBM layer behaves as a photovoltaic device. However, unlike the OASLM without interfacial layers discussed in the previous section, we do not observe any birefringence variation at 0 V. To get a better understanding of the origin of this discrepancy, additional electrical measurements have been performed.

7.5 Electrical measurements

7.5.1 Current versus time measurements

In this experiment, the current delivered by the "photovoltaic" OASLM based on a P3HT:PCBM(1:1) blend was monitored. The current was measured versus time using a preamplifier (Model 1211 from DL Instruments). The device was in the dark conditions before the laser light was switched on (λ = 532 nm at 89 mW/cm^2). The results are displayed in Figure 85.

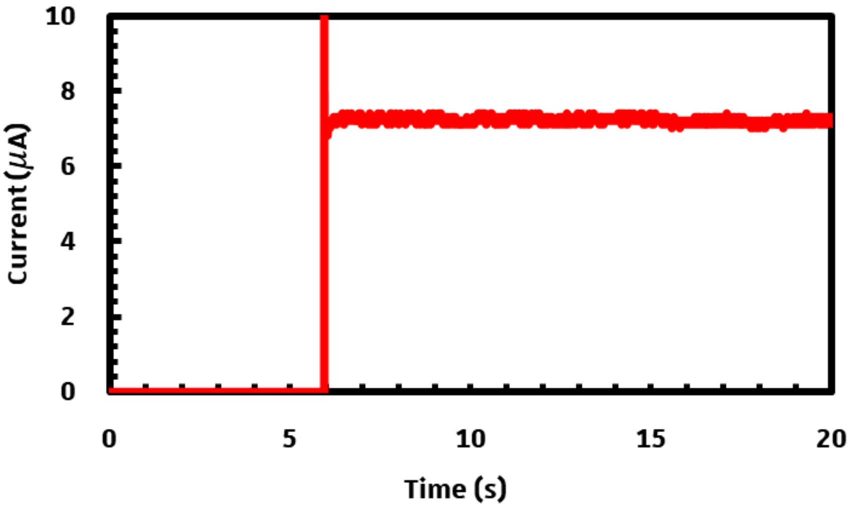

Figure 85: Current behaviour of an OASLM with a P3HT:PCBM (1:1) photovoltaic layer before and after the laser light is switched on.

Unlike the previous samples (without interfacial layers), the photocurrent quickly reached a stationary value after the laser light was switched on (5.5 s). (The sample using a structure without interfacial layers showed a transient photoresponse).

The existence of a stationary photocurrent indicates that no space charge does build up at the interfaces (due for instance to ion accumulation). Said differently, the total charge current density is constant through all the layers of the device according to the charge conservation law. This result therefore suggests that a charge transfer reaction takes place at the interface between the LC and the photovoltaic layers. We may compare this behaviour the well-known electrochemical operation of a dye-sensitized solar cell. The chemical reaction occurring at the interface remains unknown since many different ions, which could participate to the charge transfer, exist at trace amounts in the LC material. A non-exhaustive list of inorganic ions that contribute to the LC cells conductivity includes: Na^+, $NH4^+$, $Mg2^+$, K^+, $Ca2^+$, Zn^{2+},... [29]. It is also possible that the PCL and PEDOT:PSS layers led to an ionic contamination of the LC layer. The PEDOT:PSS matrix contains sulfonate groups and sodium counter-ions which could participate in a redox reaction.

An analogy can be made with the PEDOT:PSS electrochromic properties [88], [134]. In an electrochromic device, an electrolyte is comprised between two PEDOT:PSS layers that serve as a counter and working electrodes. When a voltage is applied across the electrodes, a redox reaction occurs in which a negatively biased electrode is reduced (dark blue state) while the positively biased electrode results in an oxidized and transparent pixel electrode.

Figure 86 depicts the OASLM structure when the ITO electrodes are disconnected. Upon illumination, the electrons accumulate respectively across the PEIE modified electrodes while the holes accumulate across the PEDOT:PSS electrodes. When the circuit is closed, the photovoltaic layers serves as a source of voltage to provide energy to the electrochemical reaction.

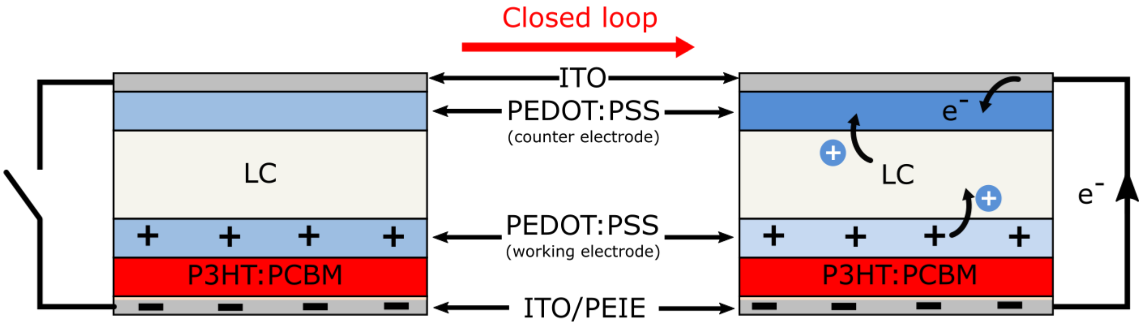

Figure 86: Schematic of a photovoltaic OASLM with the following structure: ITO/PEIE/P3HT:PCBM(1:1)/E7/PEDOT:PSS/ITO open circuit (left) and short circuit conditions (right)

The PEDOT:PSS layer at the interface between P3HT:PCBM and the LC layer, which is highly oxidized (due to an accumulation of photo-generated holes), can be reduced by a redox couple present in the LC layer. This is equivalent to a positive charge transfer from the PEDOT:PSS to the LC layer. On the opposite electrode, the photo-generated electrons accumulate in the PEDOT:PSS layer (only when the circuit is closed). The PEDOT:PSS layer is therefore in a more reduced state and can, in turn, be oxidized by the neighbouring redox couple. This mechanism may explain the stable DC photocurrent obtained and permit to avoid the accumulation of ions at the LC interfaces.

7.5.2 Current vs voltage measurements

The current vs voltage measurements were made with a new similar cell using the same photovoltaic layer structure. The CPI response of this OASLM measured at an AC frequency of 1 kHz is depicted in Figure 87. The green (λ = 532 nm) laser light intensities were varied from 0.17 mW/cm^2 to 89 mW/cm^2. The LC gap thickness was approximately 7.5 µm.

A transimpedance amplifier (TIA) circuit was used to measure the I-V characteristics: The OASLM electrode on the P3HT:PCBM side was connected to the inverting input (virtual ground) of the operational amplifier (Model 1211 from DL Instruments), while the other electrode was connected to the function generator as depicted in Figure 88.

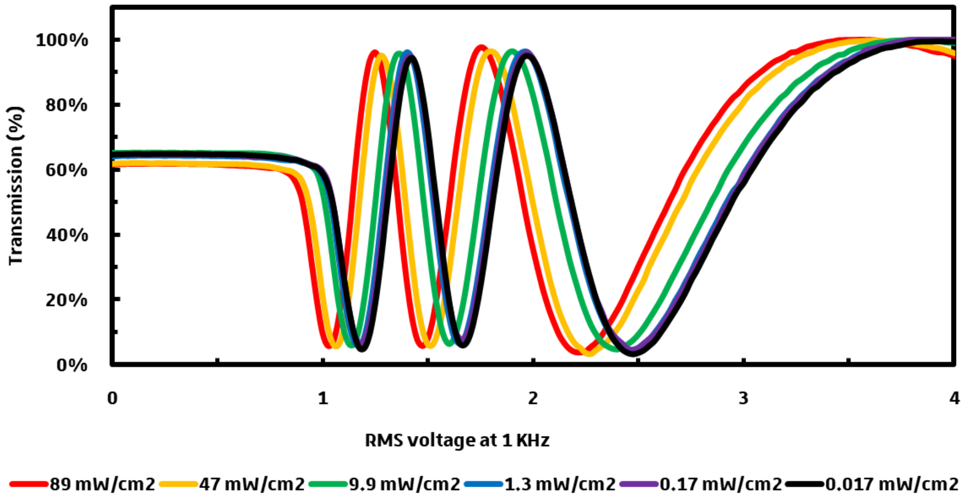

Figure 87: CPI measurement of a ITO/PEIE/P3HT:PCBM(1:1)/CPP 105D/E7/PEDOT:PSS/ITO OASLM at different light intensity as specified on the graph (λ = 532 nm)

We notice that, unlike the previous example, a slight decrease in transmittance occurs at 0V upon increasing the light intensity. It indicates that the birefringence decreases with light intensity, from 0.235 at 0.017 mW/cm^2 down to 0.2338 at 89 mW/cm^2. It is possible that this difference of 0.0012 was induced by the laser light heating the sample. Indeed, a temperature change of less than 1°C is sufficient to yield such a birefringence change.

The current vs voltage curves measured on this OASLM are shown Figure 88. The experimental conditions (light intensities, laser wavelength and laser probe location on the cell…) were the same during the electrical and optical measurements. However, the optical characterizations were made prior to the I-V measurements.

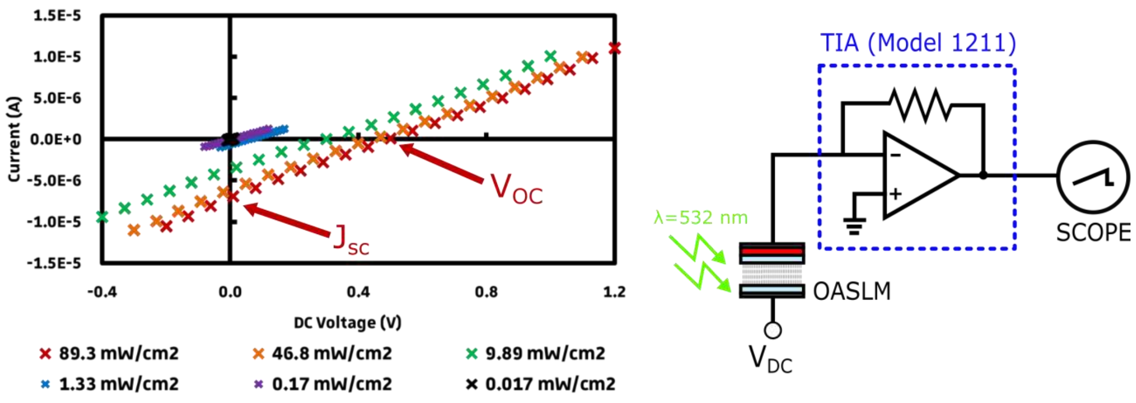

Figure 88: Current vs voltage measurement of an ITO/PEIE/P3HT:PCBM(1:1)/CPP 105D/E7/PEDOT:PSS/ITO OASLM at different light intensity as specified on the graph (left) and electrical circuit (right).

All I-V curves are linear and display the existence of a short-circuit current Isc (at 0V) and an open-circuit voltage Voc (at zero current). The linear shape leads to a fill-factor (defined as the maximum power delivered by the device divided by Isc x Voc) of 25%. Such an I-V characteristic is typical for a photodiode connected in series with a large resistance. The parameters of the photovoltaic OASLM, open circuit voltage (V_{oc}), photocurrent (I_{sc}) series and parallel resistance (R_s & R_p) are depicted as a function of light intensity on Table 3. Note that no hysteresis was observed in these voltage regions.

P_{LIGHT} (mW/cm^2) at 532 nm	Voc (V)	Isc (A)	Rs = Rp (Ω)
89.3	0.491	7.27E-06	67568
46.8	0.443	6.37E-06	69589
9.89	0.287	3.84E-06	74738
1.33	0.065	7.11E-07	90827
0.17	0.014	1.51E-07	93545
0.017	0.001	1.61E-08	91743

Table 3: Characteristics of the photovoltaic OASLM

The maximum electrically measured open circuit voltage was estimated to 0.49V. This is somewhat lower than what we would expect from a P3HT:PCBM photovoltaic cell.

It is important to note that these measurements were done while only a small area of the device (i.e. equivalent to the laser beam size) is exposed to light.

Changing the beam spot size with a diaphragm changes the I-V characteristics. By decreasing the size of the illuminated surface, the measured Voc diminishes. However, the opposite should have been observed by considering that the laser pulse shape is Gaussian. As the light intensity is stronger in the centre of the beam, the measured Voc should have been higher or at least similar. It remained an open question.

The procedure described in the previous section (§ 6.3.3) allowed me to estimate also the photovoltage optically, using CPI measurements. The fitted CPI curves are depicted in Figure 89.

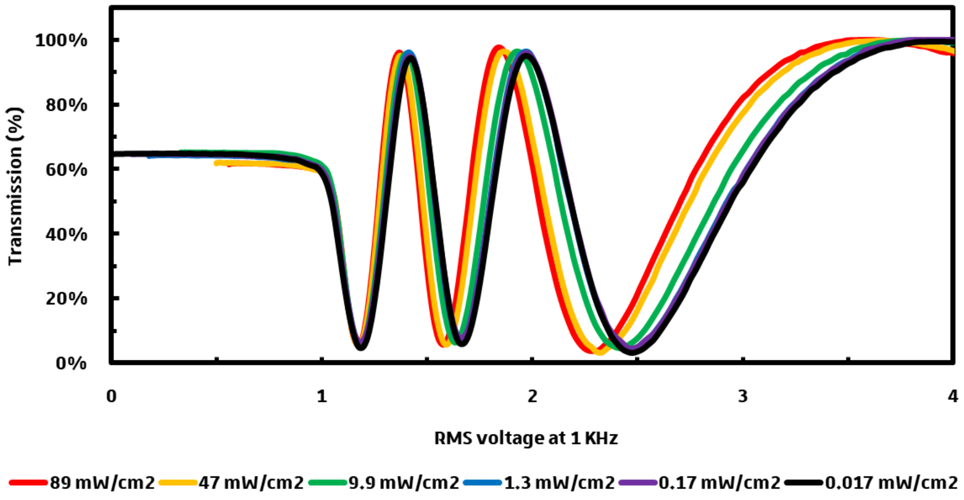

Figure 89: Fitted CPI curve of an ITO/PEIE/P3HT:PCBM(1:1)/CPP 105D/E7/PEDOT:PSS/ITO OASLM at different light intensity as specified on the graph (λ = 532 nm)

The open circuit values estimated optically (red cross) and electrically (dark cross) are compared in Figure 90.

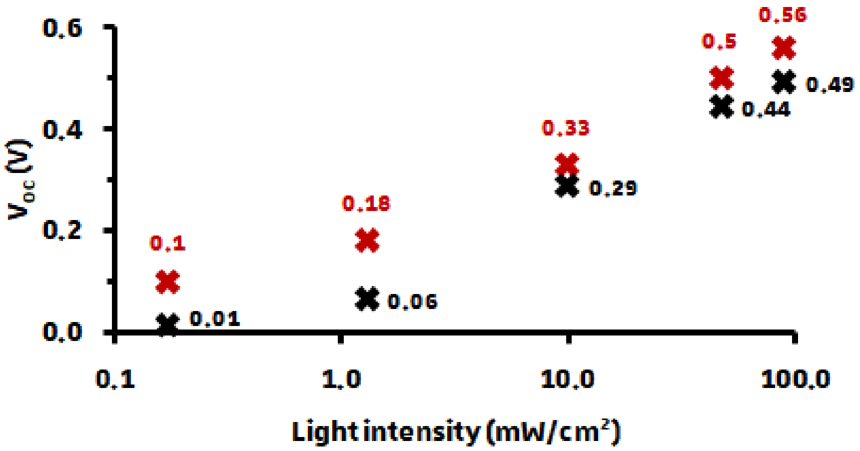

Figure 90: Open circuit voltage estimated electrically (black cross) and optically (red cross)

The Voc values estimated optically were systematically higher than the Voc values measured electrically. The minimum deviation of 10% between both measurements methods is significant. A first guess would be that this discrepancy originates from the impedance variation of the photovoltaic layers. However, this turns out to be impossible since a 100 nm thick P3HT:PCBM layer induces a negligible voltage attenuation (see section 5.2.3).

Moreover, it is important to remind that only a small area of the LC cell is illuminated by the laser during the above experiments. Yet, the electrical measurements do not give any insight into the spatial distribution of the potential. Nevertheless, once the photogenerated charges accumulate at their respective electrodes, the lateral electric fields make the charge drift towards the dark regions. In a sense, due to the thin film conductivity, non-illuminated areas may contribute to the measured open circuit voltage. In the case of a photovoltaic OASLM, lateral charge drifts not only induce a photoconductivity change in the dark areas but it also induces a DC bias across the LC molecules in the dark areas.

7.5.3 Impact of surface resistivity in PV OASLMs

In this section, we will use a simple electrical DC model to simulate the impact of surface resistivity on the OASLM electrical behaviour. The objective is not to develop an accurate electrical model, but it should rather be seen as a tool to understand the impact of surface resistivity on the electrical characteristics of a photovoltaic OASLM. In addition, even a simple model can indicate which technological parameter needs to be modified in order to improve a feature such as the spatial resolution.

A photovoltaic OASLM can be divided into several sub-cells. One sub-cell is composed of an idealized solar cell (diode D) in series with a large series resistor (RLC) that represents the LC resistance. Each sub-cell is linked to its neighbour sub-cells via a resistor (Rs), which symbolizes the lateral charge transport. A higher resistance implies a decrease of the lateral charge transport. Only one sub-cell is illuminated, this is simulated by the presence of a current source connected in parallel with the illuminated sub-cell (cell n°5 in the centre of the circuit). Rs can be seen as the surface, or sheet resistance of the PEDOT:PSS layer. We will change its value to observe its impact on the measured current-voltage curve and the effective voltage drop across the LC layer. As a reference, the curves corresponding to a homogeneous illumination are depicted by a dotted line.

The diode model depicted Figure 91 uses an idealized silicon diode model. The sheet resistance varies from 10 Ω to 10 MΩ. As we are not interested by the transient response of the system but its steady state, the capacitors are not taken into account, and they will be treated as open circuits.

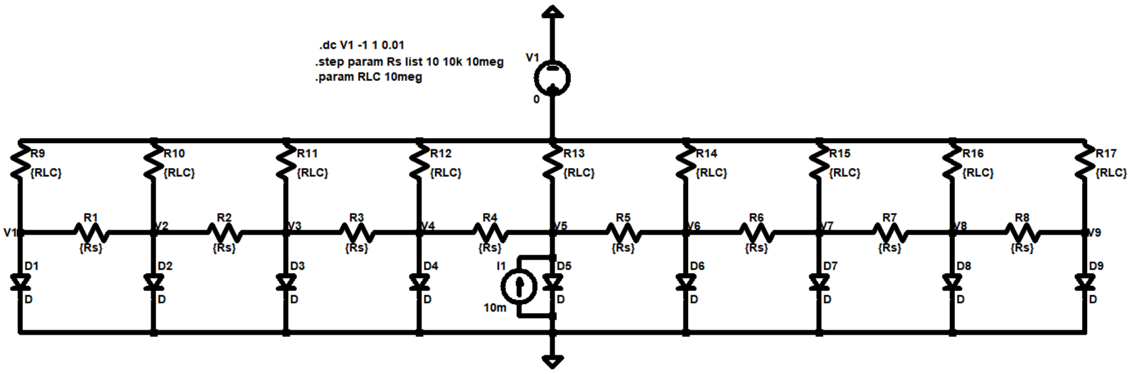

```
.dc V1 -1 1 0.01
.step param Rs list 10 10k 10meg
.param RLC 10meg
```

Figure 91: PV-OASLM model with RLC the Liquid crystal series resistance (10 MΩ), Rs the surface resistance (10Ω, 10kΩ and 10MΩ)

The potential across each diode, when the circuit is shorted (V = 0), is depicted in Figure 92 (a). Then the voltage source V_1 (see Figure 91) was varied and the respective I-V curves are plotted in Figure 92 (b).

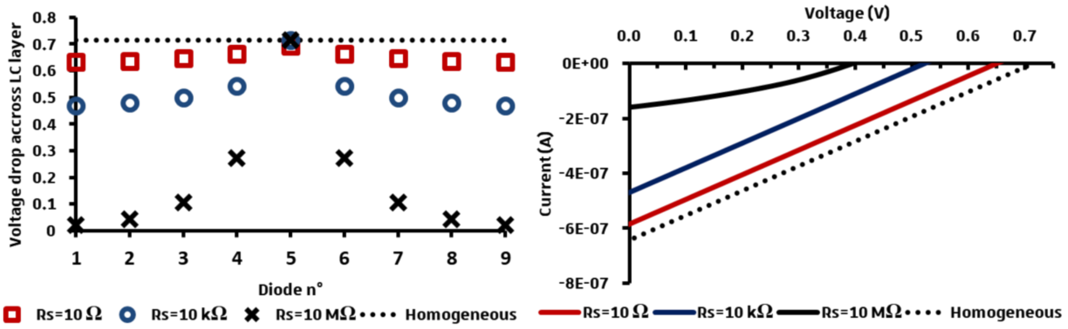

Figure 92: (a) Voltage drop across each layer as a function of diode location and sheet resistance value as specified on the graph. (b) Respective current vs voltage curve of the whole structure as a function of sheet resistance value as specified on the graph. Case of idealized silicon diodes

Independently of the Rs value, homogeneous illuminations yield the same current-voltage curves and identical potential across each diode. However, when only one diode is illuminated, the shape of the current-voltage curve depends on the sheet resistance value. Therefore, it explains the observed Voc diminution with the decrease of the illumination area (section 7.5.2).

We can observe that with decreasing Rs, the effective voltage drop spreads over the neighbouring diodes. This is an undesirable property since we want to obtain PV-OASLMs with a good lateral resolution. The current-voltage curves on Figure 92 (b) show that the electrically measured open circuit voltage will be different from the local potential across each diode. In the illuminated area, the local Voc is always higher than the electrically measured Voc and the difference between the two values depends on the surface resistivity value. This confirms that in our case, it is more accurate to rely on optical measurements rather than on electrical measurement in order to deduce the local DC voltage drop across the LC layer.

However, the performances of organic diodes are different from the performances of idealized silicon diode. The main differences are the ideality factor affecting the curve slope when the open circuit voltage is plotted against the photocurrent (or light intensity).

The open circuit voltage versus photocurrent for two different examples is shown in Figure 93. The blue curve represents an idealized photodiode with a logarithmic variation of the open circuit voltage as a function of light intensity with its slope equal to:

$$\frac{kT}{q} = 0.0259\ \mathrm{V}$$

with the Boltzmann's constant $k = 1.38065 \times 10^{-23}\, J.K^{-1}$, the temperature $T = 300°K$ and the elementary charge $q = 1.602 \times 10^{-19} C$. The non-ideal silicon diode has a slope of 0.0452, with n =1.752 (red line).

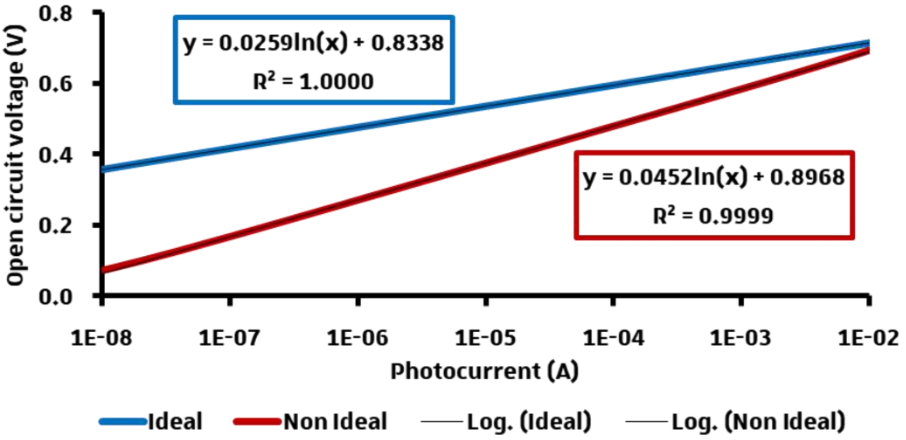

Figure 93: Open circuit voltage vs photocurrent as a function of diode ideality. Ideal silicon diode (blue curve), silicon diode with n = 1.752 (red line)

Using these non-ideal diodes in our model will not change the trend of the previous simulation. However, due to higher charge recombination (i.e. non-ideality of the diode), the potential will be less pronounced in the neighbouring non-illuminated photodiodes. Consequently, the potential drop across the LC layer in the non-illuminated areas is reduced as depicted Figure 94.

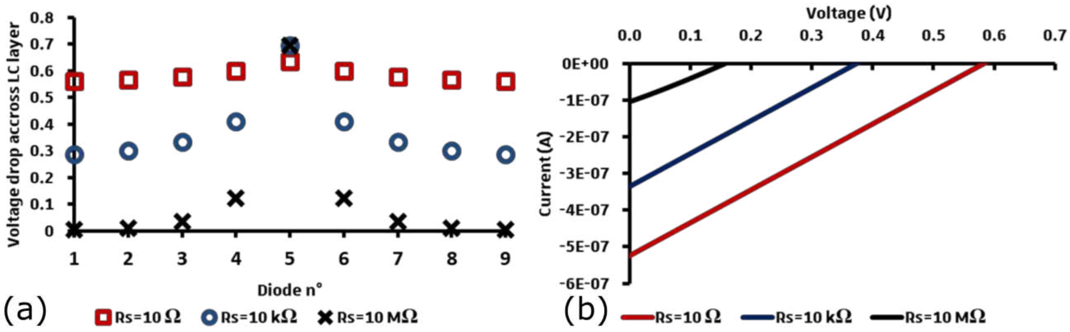

Figure 94: (a) Voltage drop across each layer as a function of diode location and sheet resistance value as specified on the graph. (b) Respective current vs voltage curve of the whole structure as a function of sheet resistance value as specified on the graph. Diode with an ideality factor of n = 1.752

Increasing the ideality factor decreases the measured potential across the non-illuminated area. Therefore, it could be interesting to use a photovoltaic material with an ideality factor higher than unity.

In this section, we have shown that we should be careful with the electrical current vs voltage measurements of such devices. Despite the fact that it clearly demonstrates that the OASLM has a photovoltaic behaviour, it also highlights the need of an optical model to estimate the effective voltage dropped across the LC layer as a function of light intensity. In addition, the electrical model depicted above shows potential routes towards improved lateral resolution of photovoltaic OASLMs that need to be verified experimentally.

7.6 Conclusion

In this chapter, we have demonstrated that it was possible to improve the LC alignment by inserting a 100 nm thick PEDOT:PSS layer between the P3HT:PCBM layer and the LC layer. OASLMs that uses a thin P3HT:PCBM layer comprised between high work function electrodes (PCL) displayed poor performances. Charge diffusion from the ohmic contacts increased the dark conductivity, which decreases the photosensitivity. An efficient way to keep a thin layer and obtain a significant variation of the LC response as a function of light intensity is to use the photovoltaic effect. However, compared to the previous samples with a large pretilt angle at the LC/P3HT:PCBM interface we have lost the LC modulation at 0V.

In order to achieve a LC modulation at 0V induced by light only, the open circuit voltage needs to be higher than the threshold voltage. Further improvements can be achieved using liquid crystalline materials whose threshold voltage is lower than that of E7. This can be seen as the basic design rule of photovoltaic OASLMs. However, with the current structure, the spatial resolution is reduced due to the low resistivity of the PEDOT:PSS layer.

In addition, it has been shown that the surface resistivity influences the current vs voltage measurements and an optical fitting method needs to be used to estimate the effective DC voltage drop across the LC layer. In the final chapter, we will present some routes that may improve photovoltaic OASLMs performances and new application opportunities offered by this original device structure.

8 Conclusions & perspectives

The initial goal of my PhD project was to design organic OASLM devices based on photoconductive organic layers. This objective evolved continuously during the thesis, as it appeared feasible to use the photovoltaic effect produced by the organic bulk heterojunction to control the LC molecules orientation without the necessity to apply an external voltage. In that regard, this work lays down the basic principles of a new type of OASLM.

The first devices were built and characterized following the procedures developed previously by the group of Professor Kaczmarek from the University of Southampton. However, different organic semiconducting molecules were used, namely the electron-donor P3HT polymer and the electron-acceptor PCBM fullerene derivative. The unexpected and distinctive response of OASLMs using such blends led us to the conclusion that a photovoltaic effect might contribute to the LC reorientation. Despite the fact that ionic accumulation should have cancelled the photogenerated DC voltage, the devices were surprisingly stable.

Following this observation, we deepened our understanding by carrying experiments and simulations to explain the electro-optical behaviour of this new type of device. As the transient photocurrent renders an electrical measure of the Voc impossible. We estimated this important value optically. We measured the contact angle of our sample to explain the large pretilt angle, which underlies the absence of threshold voltage.

The crystal rotation methods confirmed our observations, furthermore they indicated that in some cases the pretilt can increase with increasing light intensity. Additional features such as the measured diffraction efficiency at 0V have highlighted the potential of this OASLM. However, several issues such as the uncontrolled LC pretilt angle, the potential damage induced during rubbing and the possible fullerene dissolution pushed us towards another device structure.

Through interface engineering, it was possible to control both the photoresponse and the LC layer properties. Even if we did not succeed to design a photoconductive OASLM via this method, it yielded promising results for the photovoltaic type device. The unanticipated stable photocurrent confirmed that the direction we took was good. The work presented here permits to see more clearly the principles of photovoltaic OASLMs. However, the last device type does not operate at zero voltage because the low pretilt angle makes the LC threshold superior to the photovoltage. In addition, the high conductivity PEDOT:PSS we used makes it unsuitable for application requiring high spatial resolution. Even though, we presented potential solutions, such as using a LC with a lower threshold voltage or using a more resistive PEDOT:PSS, some of them need still to be tested.

Admittedly, much is still to be done to deepen our understanding of photovoltaic OASLMs. For instance, we did not identify clearly the mechanisms who explain the stable photocurrent. Moreover, this mechanism might affect the performances of photovoltaic OASLM such as the spatial resolution or LC modulation due to an ionic flow. In addition, the long-term stability as not been tested yet and remains unknown.

On the other hand, there are a lot of opportunities to improve the device performances by selecting other organic semiconductors, liquid crystals, interfacial layers, etc. Voltage free OASLMs may be achieved using organic blends that are able to generate higher open circuit voltages. Such devices would be interesting as they could be more easily incorporated in compact systems than inorganic crystals such as $LiNbO_3$. Organic materials are less costly to produce, easily processable and more bendable. However, if we want to incorporate these devices in measurements systems, we need to improve their spatial resolution.

We can imagine using photovoltaic OASLMSs to develop energy autonomous devices whose transparency is modulated by the intensity of incident light. The current state of the art SiC LCLVs (see section 3.1.2) need both, voltage and light to operate. Moreover, for such applications, the spatial resolution is less important. However, it is crucial to optimize the maximum open-circuit voltage and device transparency.

Following these ideas, we applied for a patent in 2017 and started a project funded by Conectus to explore possible large-scale applications of this new technology. Thus, the work started with this thesis will continue.

9 Résumé de la thèse en français

9.1 Introduction

Cette thèse, réalisée à l'Université de Strasbourg sous la direction du professeur Thomas Heiser, est consacrée au développement de Modulateurs de lumière à commande optique composés d'une couche photovoltaïque organique. Ces travaux ont été menés en collaboration avec l'équipe dirigée par Malgosia Kaczmarek de l'Université de Southampton et ont été financés par un programme franco-britannique, géré conjointement par la DGA et la DSTL.

Les valves optiques (LV) et les modulateurs de lumière à commande optique (OASLMs), font partie des technologies bien établies. Les dispositifs actuels combinent des matériaux photoconducteurs inorganiques (arséniure de gallium (AsGa) [13], silicium cristallin [14] ou amorphe [15]) avec une couche de cristaux liquides. Bien que fiables, ils sont limités à un fonctionnement en réflexion du fait de la forte absorption du silicium dans le spectre visible. La résolution spatiale de tels dispositifs est limitée pour ce type de photoconducteur par la diffusion des porteurs de charge, dont la mobilité est intrinsèquement élevée. De plus, les coûts de production de ces technologies demeurent élevés.

Pour toutes ces raisons, les semi-conducteurs organiques [16], [17] peuvent rivaliser avec leurs homologues inorganiques dans cette application. Le dépôt des couches photosensibles organiques peut s'effectuer par voie humide ou par sublimation sous vide ce qui permet d'envisager des dispositifs de grande surface à bas coût. La sensibilité spectrale des matériaux organiques peut être ajustée (grâce à l’ingénierie moléculaire) et limitée à une fenêtre spectrale étroite. De plus, pour les semi-conducteurs organiques, la mobilité des porteurs de charge est typiquement inférieure d’un facteur 1000 comparées à celle du silicium amorphe. Cela limite la diffusion latérale des charges et devrait améliorer la résolution spatiale du dispositif.

Au cours de mon projet de thèse, j'ai cherché à intégrer une nouvelle classe de semi-conducteurs organiques dans un OASLM pour étudier et comprendre les phénomènes physiques sous-jacents afin d'optimiser les performances du dispositif.

9.1.1 Principe de fonctionnement

On utilise les propriétés de biréfringence des cristaux liquides pour modifier la polarisation de la lumière traversant l'OASLM. La biréfringence (Δn) de ce milieu est fonction de l'orientation des molécules. Elle est maximale lorsque les molécules sont orientées parallèlement au substrat et tend vers zéro lorsque les molécules sont orientées perpendiculairement par rapport au substrat.

On contrôle l'orientation moléculaire, donc la biréfringence, lorsqu'un champ électrique est appliqué au dispositif. Le champ appliqué aux bornes du cristal liquide peut être modulé grâce à un photoconducteur qui sert de photorésistance variable. La chute de potentiel aux bornes des cristaux liquides, donc leur orientation, est alors fonction de l'intensité de l'éclairement ainsi que de la longueur d'onde choisie. Ce principe est illustré Figure 95.

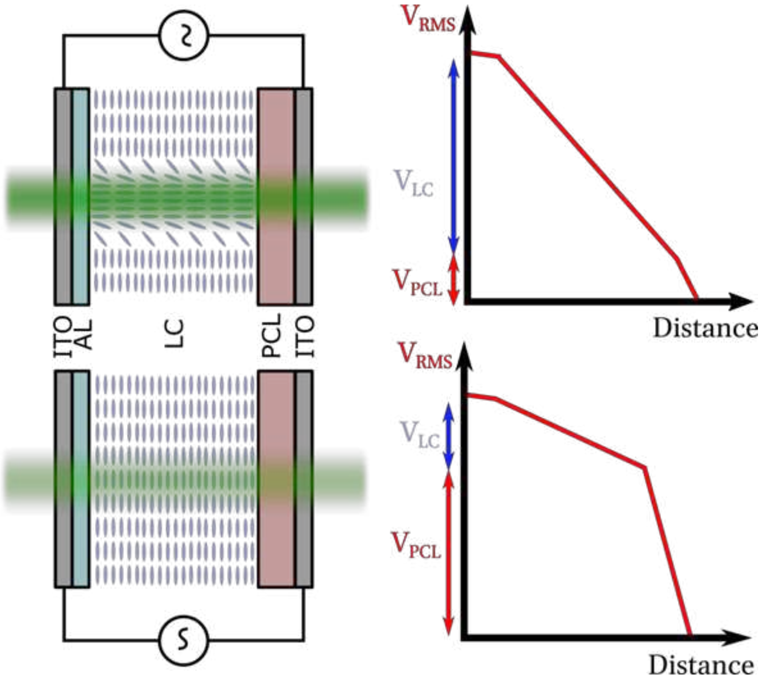

Figure 95 : Schéma de principe d'un OASLM

Un OASLM est composé d'une couche de cristal liquide (LC) comprise entre deux lames de verre conductrice (ITO). Un photoconducteur (PCL) est déposé sur l'une des lames de verre ITO. Une couche d'alignement (AL) est déposée sur le second verre ITO. Ce type de dispositif peut être envisagé dans des applications comme les limiteurs optiques, pour la protection d'appareils sensible [23], les vitres intelligentes ou encore en holographie adaptative [13].

Nous avons choisi le mélange P3HT:PCBM pour démarrer notre étude, un matériau qui a longtemps été une "référence" dans le développement de dispositifs photovoltaïques organiques.

9.2 Méthodes

Dans cette section, nous allons décrire de façon succincte la méthodologie adoptée pour étudier la réponse d'OASLMs utilisant le P3HT:PCBM comme couche photosensible. Nous nous sommes appuyés sur l'expertise de l'équipe de Southampton pour la fabrication et la caractérisation optique en matière d'OASLMs. L'équipe Strasbourgeoise, a apporté ses compétences en matière de contrôle des propriétés optoélectroniques d'un mélange donneur accepteur tel que le P3HT:PCBM. Les propriétés des matériaux photosensibles organiques en couche minces sont affectées par le ratio massique du mélange donneur/accepteur et la nature des électrodes aux interfaces. La conception des OASLMs a donc été étudiée en prenant en compte ces différents paramètres.

9.2.1 Conception des OASLMs

Dans ce paragraphe, nous allons présenter la structure générale des OASLMs mis en place au début du projet. Le schéma présenté Figure 96 rappelle les différents éléments formant le dispositif étudié.

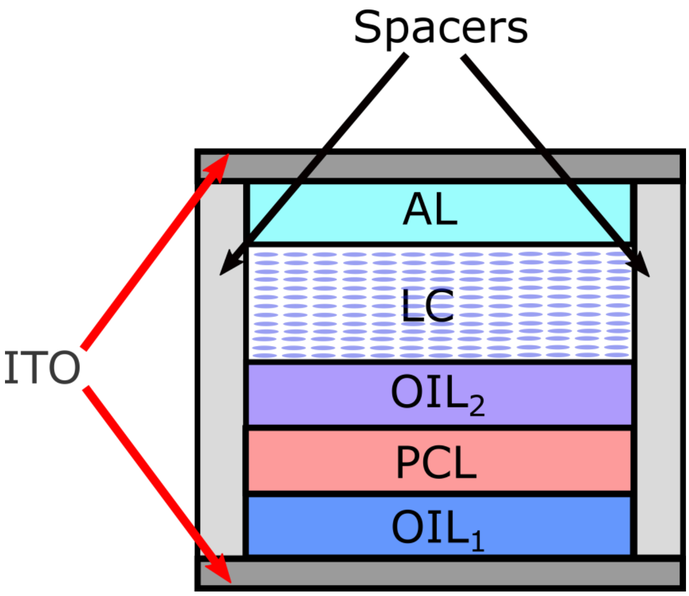

Figure 96 : Structure des OASLMs avec une couche photosensible organique.

La couche de cristaux liquides (LC) est comprise entre deux électrodes (ITO) qui sont maintenues à une distance de 7.75 µm grâce à des espaceurs (Spacers). Sur l'une des électrodes, un matériau servant de couche d'alignement (AL) a été déposé. Sur l'autre électrode, la partie photosensible est une structure en multicouches composée d'une première couche d'interface optionnelle (OIL_1), du mélange donneur accepteur (PCL) et d'une dernière couche d'interface optionnelle (OIL_2). Différents modèles d'OASLMs ont été réalisés en suivant ce schéma de conception.

9.2.2 Caractérisation électro-optique des OASLMs

La biréfringence d'un dispositif à cristaux liquides peut être obtenue en fonction de la tension appliquée, par une simple mesure entre deux polariseurs croisés (CPI) [97] schématisé Figure 97.

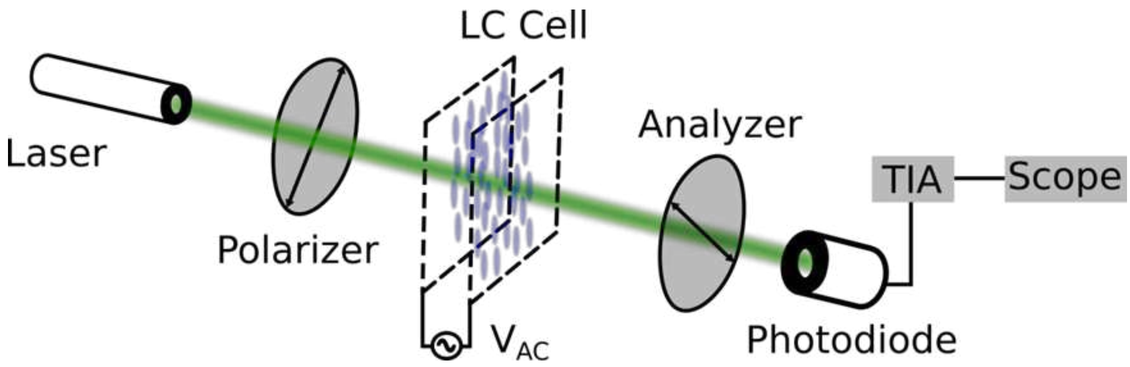

Figure 97 : Mesure de la biréfringence d'une cellule à cristaux liquides

Un faisceau monochromatique (λ = 532 nm) issu d'un laser est polarisé linéairement avant de traverser la cellule à cristaux liquides (LC Cell). La cellule à cristaux liquides induit une différence de phase entre les deux composantes du faisceau lumineux polarisé et en sortie de la cellule, la lumière est polarisée elliptiquement. Un second polariseur linéaire (Analyzer) permet de convertir l'état de polarisation en sortie de la cellule en une variation d'intensité lumineuse, elle-même convertie en une variation de courant par une photodiode utilisant un amplificateur à transimpédance (TIA).

L'estimation des performances des OASLMs est obtenue en répétant cette mesure à différentes intensités lumineuses, et/ou à différentes fréquences (VTF) [82].

9.3 Résultats importants

Dans ce paragraphe, nous discuterons des résultats importants qui ont montré que la réponse électro-optique de nos OASLMs ne pouvait s'expliquer par une simple variation de conductivité de la couche photosensible en fonction de l'éclairement.

Les premiers dispositifs que nous avons fabriqués utilisaient une structure proche de celle utilisée à Southampton pour réaliser des OASLMs. Ce n'est que dans un second temps que nous avons joué sur les couches d'interfaces afin de modifier la réponse électro-optique de nos dispositifs.

9.3.1 OASLMs avec une couche P3HT:PCBM

Afin de comparer les performances du P3HT:PCBM au PVK:C_{60}, nous avons utilisé la structure suivante : ITO/P3HT:PCBM (1:1) (PCL)/E7 (LC)/ PEDOT:PSS (E7)/ITO. La réponse (CPI) de ce type de dispositif est montrée Figure 98. La cellule est contrôlée par une tension sinusoïdale de 10 kHz, la longueur d'onde est de 532 nm et l'intensité lumineuse a été variée de 0.0018 à 49 mW/cm^2.

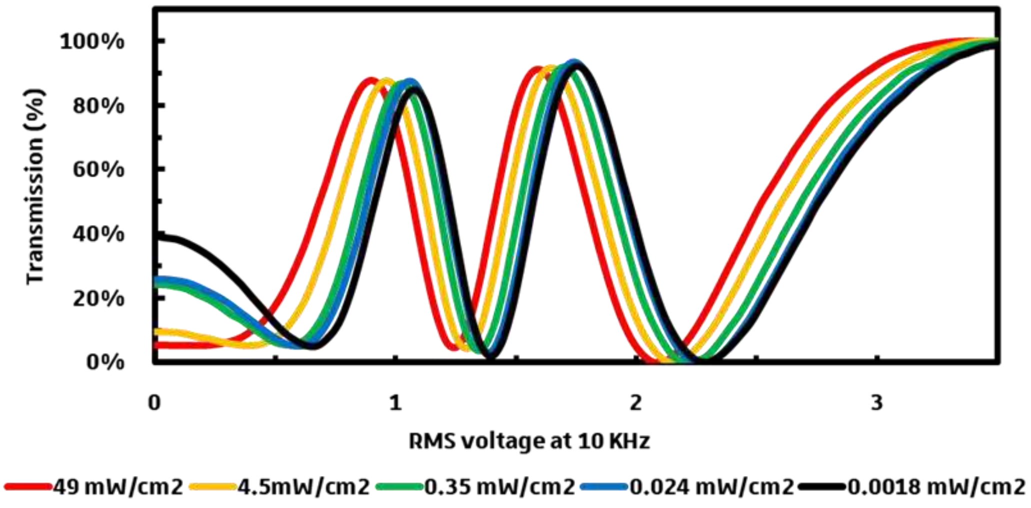

Figure 98 : Mesure CPI d'un OASLM utilisant une couche de P3HT:PCBM (1:1)

Nous avons pu constater qu'en utilisant le P3HT:PCBM comme couche photosensible et d'alignement, la réponse des cristaux liquides était bien fonction de l'intensité lumineuse. Par contre, les cristaux liquides se réorientaient sans tension appliquée à 0V en fonction de l'intensité lumineuse seule. Cet effet ne peut s'expliquer par une simple variation de l'impédance de notre couche photosensible en fonction de l'intensité de l'éclairement. Dès lors nous avons émis l'hypothèse qu'une phototension générée par notre couche P3HT:PCBM était à l'origine de cette variation de biréfringence à 0V. Des mesures complémentaires ont été réalisées entre les deux laboratoires pour confirmer cette hypothèse de départ.

La variation de tension et de biréfringence à 0V de ce type de dispositif (Figure 99) varie de manière logarithmique en fonction de l'intensité lumineuse.

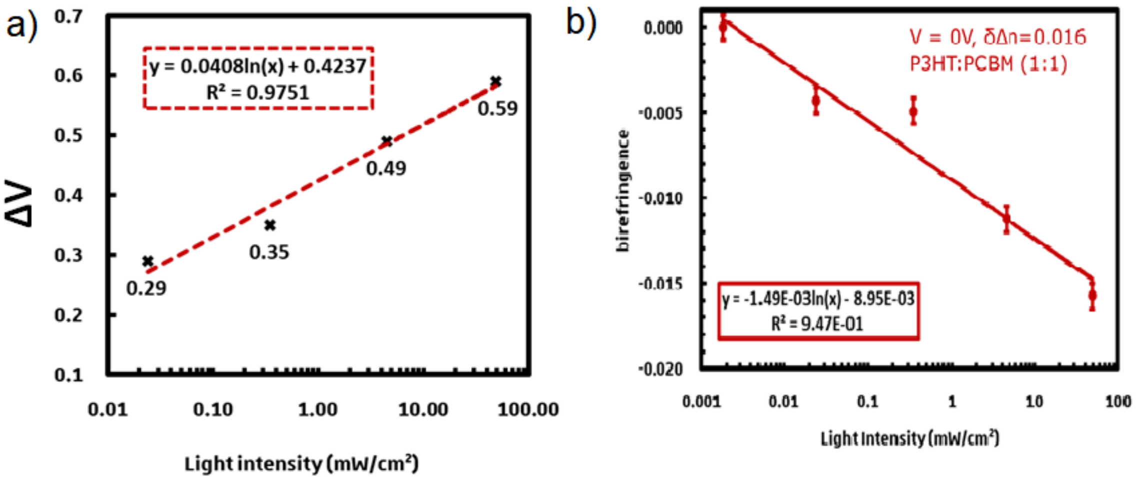

Figure 99 : Variation de tension et de biréfringence à 0 V

De plus, il a aussi été montré par des mesures d'efficacité de diffraction qu'il était possible de moduler spatialement l'orientation des cristaux liquides avec une résolution de 106 lp.mm^{-1} sans tension appliquée.

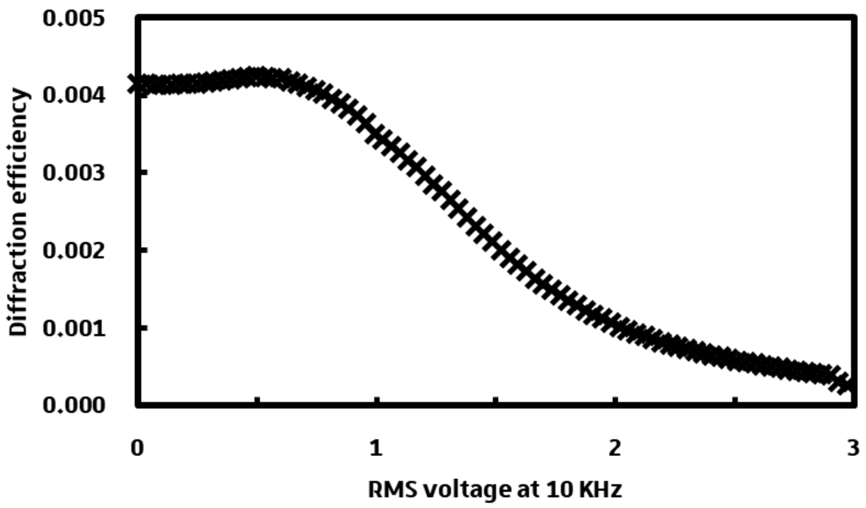

Figure 100 : Mesure de l'efficacité de diffraction d'un OASLM utilisant la structure suivante ITO/P3HT:PCBM (1:1)/E7/PEDOT:PSS/ITO.

Bien que la structure utilisée soit intéressante d'un point de vue scientifique et démontre que l'on peut contrôler la biréfringence d'un OASLM en fonction de l'intensité lumineuse seule, plusieurs inconvénients ont été identifiés. D'une part, la réorientation des cristaux liquides à 0V montre une absence de contrôle de l'orientation des cristaux liquides à l'interface avec le PCL. De plus, le traitement mécanique utilisé pour contrôler l'alignement des cristaux liquides pouvait endommager le PCL.

L'ajout de couche d'interfaces pouvait nous permettre de répondre à ces différentes problématiques et d'en apprendre plus sur le principe de fonctionnement de ces nouveaux dispositifs.

9.3.2 Optimisation des couches d'interfaces

Nous avons utilisé une couche de PEDOT:PSS à l'interface PCL/LC (OIL_2) afin de nous permettre d'obtenir un alignement planaire de la couche de CL. En modifiant la nature de l'interface ITO/PCL (OIL_1), nous avons pu modifier la réponse de notre couche photosensible. Si les deux couches d'interfaces sont de même nature, en utilisant du PEDOT:PSS à l'interface ITO/PCL nous nous attendions à obtenir une réponse purement photoconductrice. Par contre, en utilisant du PEIE à l'interface ITO/PCL, nous devrions renforcer l'effet photovoltaïque.

Les mesures CPI des structures photoconductrices n'ont montré aucune variation de la réponse des OASLMs en fonction de l'intensité lumineuse (Figure 101).

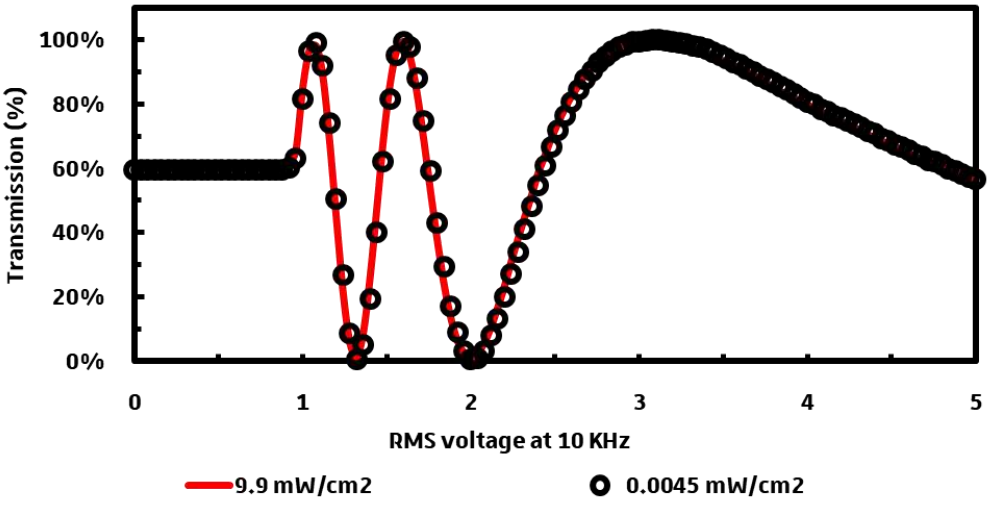

Figure 101 : Mesure CPI d'un OASLM ITO/Clevios PH/P3HT:PCBM (1:1)/CPP 105D/E7/ Clevios PH/ITO

Nous avons pu expliquer ce phénomène du fait de la présence de contacts ohmiques qui provoquent une augmentation de la conductivité d'obscurité au sein du matériau semi-conducteur [123].

Par contre, la structure photovoltaïque utilisant la structure suivante: ITO/PEIE (OIL_1)/P3HT:PCBM (PCL)/PEDOT:PSS (OIL_2)/E7 (LC)/PEDOT:PSS (AL) /ITO montrait une variation significative de la réponse optique en fonction de l'intensité lumineuse (voir Figure 102). La cellule est contrôlée par une tension sinusoïdale de 100 Hz, la longueur d'onde est de 532 nm et l'intensité lumineuse a été variée de 0.17 à 89 mW/cm^2.

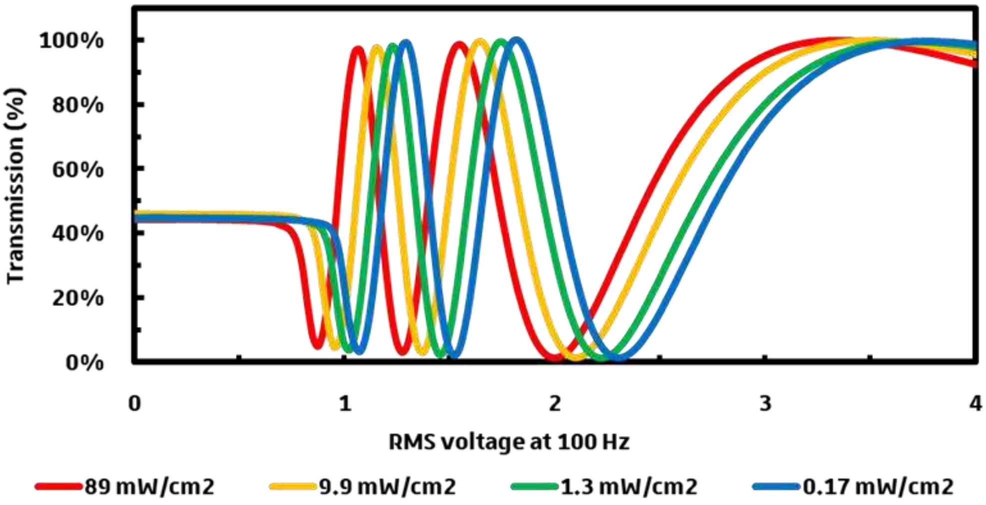

Figure 102 : Mesure CPI d'un OASLM utilisant une multicouche photovoltaïque PEIE/P3HT:PCBM (1:1)/PEDOT:PSS

En utilisant des contacts dissymétriques (avec des travaux de sorties différents), on obtient une variation de la réponse des OASLMs en fonction de l'intensité lumineuse. Du fait de l'alignement planaire des cristaux liquides, la phototension générée n'est pas suffisante pour réorienter les CLs sans tension appliquée. Néanmoins, la réponse électro-optique ne pouvait s'expliquer que par la présence d'une phototension DC qui se retrouvait aux bornes de la couche de cristaux liquides. De plus, ce genre de structure donne lieu à un photocourant stable qui permet de mesurer les caractéristiques courant-tension et donc de quantifier électriquement la phototension générée.

Grâce à ces différents dispositifs, nous avons pu développer les prémisses d'un modèle pour estimer la tension photogénérée par la couche photovoltaïque ainsi que sa variation d'impédance à partir des courbes CPI. De nombreuses améliorations sont envisageables afin d'optimiser la réponse électro-optique de ces dispositifs en fonction de l'application visée. Afin d'améliorer la transparence, il est nécessaire d'utiliser des semi-conducteurs à large bande interdite (> 3eV). Enfin des cristaux liquides à plus faible tension de seuil peuvent être utilisés afin d'obtenir une variation de biréfringence fonction de la seule intensité lumineuse.

9.4 Conclusion générale

Dans le cadre de cette thèse, nous avons étudié de manière approfondie la réponse d'OASLMs utilisant un mélange P3HT:PCBM comme couche photoconductrice. Cet objectif a évolué au cours de la thèse, car il nous apparaissait possible d'utiliser la phototension générée par l'hétérojonction volumique organique pour contrôler l'orientation des cristaux liquides sans alimentation extérieure. De ce point de vue, ce travail décrit les principes de base d'un nouveau type d'OASLM.

Les premiers dispositifs ont été fabriqués et caractérisés en suivant les méthodes développées par le groupe du professeur Kaczmarek de l'Université de Southampton. Cependant, les molécules organiques semi-conductrices utilisées étaient différentes, à savoir le P3HT (donneur d'électrons) et le PCBM (accepteur d'électrons). La réponse inattendue des OASLMs utilisant ce type de mélange est typique d'un système photovoltaïque et montre que la phototension générée contribue à l'orientation des molécules de cristaux liquides. Les dispositifs étaient étonnamment stables, malgré le fait que l'accumulation ionique aurait dû écranter le champ électrique DC photogénéré.

A la suite de ces observations, nous avons approfondi notre compréhension du phénomène en menant des expériences et des simulations complémentaires pour expliquer le comportement de ce nouveau type de dispositif. Nous avons estimé la phototension générée à partir de mesure électro-optique (CPI). L'absence de tension de seuil des dispositifs a été expliquée par un large "pretilt" à l'interface entre le P3HT:PCBM et le cristal liquide. L'efficacité de diffraction obtenue à 0V a mis en évidence le potentiel de ces OASLMs pour des applications liées à l'holographie. Des problèmes ont aussi été mis en évidence comme les dommages potentiels induits durant le brossage de notre couche photosensible et la possible dissolution des fullerènes dans le cristal liquide. Nous avons donc envisagé une structure alternative à ce premier type de dispositif.

Grâce à l'ingénierie des interfaces, nous avons pu contrôler la réponse électro-optique du dispositif qui a donné des résultats prometteurs comme un photocourant stable. Cependant, les dispositifs intégrant les couches d'interfaces ne permettent pas de fonctionner sans tension appliquée. En outre la faible résistivité du PEDOT:PSS utilisé augmente fortement la conductivité à la surface du PCL, diminuant de fait la résolution spatiale de ce type de dispositif. Des solutions potentielles, telles que l'utilisation d'un cristal liquide à plus faible tension de seuil et l'emploi d'un PEDOT:PSS plus résistif doivent encore être testées.

Il reste encore beaucoup à faire pour approfondir notre compréhension des OASLMs photovoltaïques. Par exemple, nous n'avons pas identifié les mécanismes expliquant la stabilité de nos dispositifs en DC. En outre, la stabilité à long terme n'a pas encore été testée et reste inconnue.

Par contre, il existe de nombreuses possibilités d'améliorer les performances des dispositifs en sélectionnant d'autres semi-conducteurs organiques, cristaux liquides, couches d'interfaces, etc... Des OASLMs autonomes peuvent être obtenus en utilisant d'autres mélanges donneur/accepteur capables de générer des tensions de circuit ouvert plus élevée. De tels dispositifs seraient intéressants, ils pourraient être plus facilement incorporés dans des systèmes compacts, car les matériaux organiques sont moins coûteux à produire, plus facile à mettre en œuvre, flexibles et ne requièrent aucune autre source d'alimentation que la lumière qui les traverse. Cependant, si nous voulons intégrer ces dispositifs dans des systèmes de mesure, nous devons améliorer leur résolution spatiale.

On peut imaginer utiliser des OASLMS photovoltaïques pour développer des dispositifs autonomes en énergie dont la transparence est modulée uniquement par l'intensité de la lumière incidente. De plus, pour de telles applications, la résolution spatiale est moins importante. Cependant, il sera crucial d'optimiser la tension générée par la couche photovoltaïque ainsi que sa transparence.

9.5 Contributions scientifiques

9.5.1 Contributions par affiches

Aweke, F., Le Normand, F., Antoni, F., Muller, D., Lévêque, P., **Regrettier, T.**, Zafeiratos, S., Cojocaru, C. « Graphene on Diamond-like carbone (DLC) as transparent electrodes », présenté au 23ème congrès de la Société Française de Physique, Strasbourg, 2015.

T. Regrettier, T. Heiser, M. Kaczmarek, et M. Proctor, « Optically addressed spatial light modulators (OASLM) using a P3HT:PCBM blend as photoconductive layer. », présenté à Science et Technologie des Systèmes pi-Conjugués (SPIC), Angers, 2015.

9.5.2 Brevet

Regrettier, Thomas, Thomas Heiser, and Malgosia Kaczmarek. n.d. LIQUID CRYSTAL SPATIAL LIGHT MODULATOR, filed August 17, 2017.

9.5.3 Publication

Bennett, T., Proctor, M., Forster, J., Perivolari, E., Podoliak, N., Sugden, M., Kirke, R., **Regrettier, T.**, Heiser, T., Kaczmarek, M., D'Alessandro, G., 2017. Wide area mapping of liquid crystal devices with passive and active command layers. Applied Optics 56, 9050. doi:10.1364/AO.56.009050

BIBLIOGRAPHY AND APPENDIX CONTENT

Bibliography

[1] B. Geffroy, P. le Roy, and C. Prat, ‘Organic light-emitting diode (OLED) technology: materials, devices and display technologies’, *Polym. Int.*, vol. 55, no. 6, pp. 572–582, Jun. 2006.

[2] M. Faraday, *Experimental researches in electricity*, vol. 1, 3 vols. London: Richard and John-Edward Taylor, 1849.

[3] M. F. Wohler, ‘Artificial formation of urea’, *Philos. Mag.*, vol. 4, no. 22, pp. 309–310, Oct. 1828.

[4] F. So, J. Kido, and P. Burrows, ‘Organic Light-Emitting Devices for Solid-State Lighting’, *MRS Bull.*, vol. 33, no. 7, pp. 663–669, 2008.

[5] M. A. Green, K. Emery, Y. Hishikawa, W. Warta, and E. D. Dunlop, ‘Solar cell efficiency tables (Version 45): Solar cell efficiency tables’, *Prog. Photovolt. Res. Appl.*, vol. 23, no. 1, pp. 1–9, Jan. 2015.

[6] G. Horowitz, *Organic Field-Effect Transistors*, vol. 10. 1998.

[7] T. N. Jackson, ‘Organic Semiconductors: Beyond Moore’s Law’, *Nat Mater*, vol. 4, no. 8, pp. 581–582, août 2005.

[8] T. Riedl *et al.*, ‘Tunable organic thin-film laser pumped by an inorganic violet diode laser’, *Appl. Phys. Lett.*, vol. 88, no. 24, p. 241116, Jun. 2006.

[9] A. Hamidi-Sakr *et al.*, ‘A Versatile Method to Fabricate Highly In-Plane Aligned Conducting Polymer Films with Anisotropic Charge Transport and Thermoelectric Properties: The Key Role of Alkyl Side Chain Layers on the Doping Mechanism’, *Adv. Funct. Mater.*, vol. 27, no. 25, p. 1700173–n/a, juillet 2017.

[10] S. Sanvito and V. A. Dediu, ‘News from the organic arena’, vol. 7, p. 696, Nov. 2012.

[11] P. Lienerth, ‘Elaboration and characterization of field-effect transistors based on organic molecular wires for chemical sensing applications’, Université de Strasbourg, 2014.

[12] P. K. Shrestha, Y. T. Chun, and D. Chu, ‘A high-resolution optically addressed spatial light modulator based on ZnO nanoparticles’, *Light Sci. Appl.*, vol. 4, no. 3, p. e259, Mar. 2015.

[13] A. Peigné *et al.*, ‘Adaptive holographic interferometer at 1.55 µm based on optically addressed spatial light modulator’, *Opt. Lett.*, vol. 40, no. 23, p. 5482, Dec. 2015.

[14] U. Efron, J. Grinberg, P. O. Braatz, M. J. Little, P. G. Reif, and R. N. Schwartz, 'The silicon liquid-crystal light valve', *J. Appl. Phys.*, vol. 57, no. 4, pp. 1356–1368, Feb. 1985.

[15] W. Li, C. T. Kuo, and G. Moddel, 'High-speed optically-addressed spatial light modulator', *IEEE Trans. Electron Devices*, vol. 35, no. 12, pp. 2447–2448, décembre 1988.

[16] M. Kaczmarek, A. Dyadyusha, S. Slussarenko, and I. C. Khoo, 'The role of surface charge field in two-beam coupling in liquid crystal cells with photoconducting polymer layers', *J. Appl. Phys.*, vol. 96, no. 5, pp. 2616–2623, 2004.

[17] A. Dyadyusha, M. Kaczmarek, and G. Gilchrist, 'Surface Screening Layers and Dynamics of Energy Transfer in Photosensitive Polymer-Liquid Crystal Structures', *Mol. Cryst. Liq. Cryst.*, vol. 446, no. 1, pp. 261–272, Apr. 2006.

[18] K. M. Johnson, D. J. McKnight, and I. Underwood, 'Smart spatial light modulators using liquid crystals on silicon', *IEEE J. Quantum Electron.*, vol. 29, no. 2, pp. 699–714, Feb. 1993.

[19] G. Moddel, K. M. Johnson, W. Li, R. A. Rice, L. A. Pagano-Stauffer, and M. A. Handschy, 'High-speed binary optically addressed spatial light modulator', *Appl. Phys. Lett.*, vol. 55, no. 6, pp. 537–539, Aug. 1989.

[20] Y. Ooi and T. Hara, 'Spatial light modulating devices utilizing electro-optic crystal', mai 1990.

[21] K. A. Bauchert, S. A. Serati, G. D. Sharp, and D. J. McKnight, 'Complex phase/amplitude spatial light modulator advances and use in a multispectral optical correlator', *Opt. Pattern Recognit. VIII*, vol. 3073, pp. 170–177, 1997.

[22] W. A. Crossland and T. M. Coker, 'Image display system', Nov-2003.

[23] C. D. Burgess, 'Optically addressed light valve comprising two photoconducting layers placed on each side of an electro-optical modulator', mai-2012.

[24] A. Peigné, 'Holographie adaptative pour la réalisation de capteurs à fibres optiques de très grande sensibilité: application à la détection d'ondes acoustiques sous-marines', Université Nice Sophia Antipolis, 2016.

[25] K. Choi, H. Song, H. Lee, Y. Choi, J. Bae, and S. Han, *Apparatus and method for holography 3-dimensional display*. 2015.

[26] J. Hoogboom, T. Rasing, A. E. Rowan, and R. J. M. Nolte, 'LCD alignment layers. Controlling nematic domain properties', *J Mater Chem*, vol. 16, no. 14, pp. 1305–1314, 2006.

[27] M. Schadt and W. Helfrich, ‘VOLTAGE-DEPENDENT OPTICAL ACTIVITY OF A TWISTED NEMATIC LIQUID CRYSTAL’, *Appl. Phys. Lett.*, vol. 18, no. 4, pp. 127–128, février 1971.

[28] P. J. Bos and K. R. Koehler/beran, ‘The pi-Cell: A Fast Liquid-Crystal Optical-Switching Device’, *Mol. Cryst. Liq. Cryst.*, vol. 113, no. 1, pp. 329–339, 1984.

[29] Y. Garbovskiy and I. Glushchenko, ‘Nano-Objects and Ions in Liquid Crystals: Ion Trapping Effect and Related Phenomena’, *Crystals*, vol. 5, no. 4, pp. 501–533, Nov. 2015.

[30] S. H. Perlmutter, D. Doroski, and G. Moddel, ‘Degradation of liquid crystal device performance due to selective adsorption of ions’, *Appl. Phys. Lett.*, vol. 69, no. 9, pp. 1182–1184, Aug. 1996.

[31] S. M. Sze, *Physics of Semiconductor Devices*. John Wiley & Sons, 1981.

[32] L. Wang and G. Moddel, ‘Effects of charge spreading on resolution of optically addressed spatial light modulators’, *Opt Lett*, vol. 19, no. 23, pp. 2033–2035, décembre 1994.

[33] J. Czochralski, ‘Ein neues Verfahren zur Messung der Kristallisationsgeschwindigkeit der Metalle’, *Zeitschrift für Physikalische Chemie*, 01-Nov-1918.

[34] J.-L. Brédas, D. Beljonne, V. Coropceanu, and J. Cornil, ‘Charge-Transfer and Energy-Transfer Processes in π-Conjugated Oligomers and Polymers: A Molecular Picture’, *Chem. Rev.*, vol. 104, no. 11, pp. 4971–5004, Nov. 2004.

[35] A. K. Ghosh and T. Feng, ‘Merocyanine organic solar cells’, *J. Appl. Phys.*, vol. 49, no. 12, pp. 5982–5989, Dec. 1978.

[36] G. Yu, J. Gao, J. C. Hummelen, F. Wudl, and A. J. Heeger, ‘Polymer Photovoltaic Cells: Enhanced Efficiencies via a Network of Internal Donor-Acceptor Heterojunctions’, *Science*, vol. 270, no. 5243, p. 1789, décembre 1995.

[37] P. M. Borsenberger, *Organic Photoreceptors for Xerography*. Taylor & Francis, 1998.

[38] M. Proctor *et al.*, ‘Light-activated modulation and coupling in integrated polymer–liquid crystal systems’, *J. Opt. Soc. Am. B*, vol. 31, no. 12, p. 3144, Dec. 2014.

[39] M. D. Sturge, ‘Optical Absorption of Gallium Arsenide between 0.6 and 2.75 eV’, *Phys Rev*, vol. 127, no. 3, pp. 768–773, août 1962.

[40] B. Dischler and U. Kaufmann, ‘Photo response of the EL2 absorption band and of the As+Ga ESR signal in GaAs’, *Rev. Phys. Appl.*, vol. 23, no. 5, pp. 779–791, 1988.

[41] P. T. B. Shaffer, ‘A review of the structure of silicon carbide’, *Acta Crystallogr. Sect. B*, vol. 25, no. 3, pp. 477–488, Mar. 1969.

[42] W. J. Choyke, D. R. Hamilton, and L. Patrick, ‘Optical Properties of Cubic SiC: Luminescence of Nitrogen-Exciton Complexes, and Interband Absorption’, *Phys Rev*, vol. 133, no. 4A, pp. A1163–A1166, février 1964.

[43] W. C. Mitchel *et al.*, ‘Fermi level control and deep levels in semi-insulating 4H–SiC’, *J. Appl. Phys.*, vol. 86, no. 9, pp. 5040–5044, Nov. 1999.

[44] J. R. Jenny *et al.*, ‘On the compensation mechanism in high-resistivity 6H–SiC doped with vanadium’, *J. Appl. Phys.*, vol. 78, no. 6, pp. 3839–3842, Sep. 1995.

[45] H. M. Hobgood *et al.*, ‘Semi-insulating 6H–SiC grown by physical vapor transport’, *Appl. Phys. Lett.*, vol. 66, no. 11, pp. 1364–1366, Mar. 1995.

[46] J. Schneider *et al.*, ‘Infrared spectra and electron spin resonance of vanadium deep level impurities in silicon carbide’, *Appl. Phys. Lett.*, vol. 56, no. 12, pp. 1184–1186, Mar. 1990.

[47] S. A. Reshanov and V. P. Rastegaev, ‘Photoconductivity of semi-insulating SiC: 〈V,Al〉 ’, *Diam. Relat. Mater.*, vol. 10, no. 11, pp. 2035–2038, 2001.

[48] J. S. Sullivan and J. R. Stanley, ‘6H-SiC Photoconductive Switches Triggered at Below Bandgap Wavelengths’, in *Conference Record of the 2006 Twenty-Seventh International Power Modulator Symposium*, 2006, pp. 215–218.

[49] C. D. Burgess, ‘Optically addressed light valve’, 03-Sep-2013.

[50] J. L. Carns, G. Cook, M. A. Saleh, S. V. Serak, N. V. Tabiryan, and D. R. Evans, ‘Self-activated liquid-crystal cells with photovoltaic substrates’, *Opt. Lett.*, vol. 31, no. 7, pp. 993–995, 2006.

[51] L. Lucchetti, K. Kushnir, A. Zaltron, and F. Simoni, ‘Liquid crystal cells based on photovoltaic substrates’, *J. Eur. Opt. Soc.-Rapid Publ.*, vol. 11, 2016.

[52] K. Buse, ‘Light-induced charge transport processes in photorefractive crystals I: Models and experimental methods’, *Appl. Phys. B*, vol. 64, no. 3, pp. 273–291, Mar. 1997.

[53] A. M. Glass, D. von der Linde, and T. J. Negran, ‘High-voltage bulk photovoltaic effect and the photorefractive process in LiNbO3’, *Appl. Phys. Lett.*, vol. 25, no. 4, pp. 233–235, août 1974.

[54] L. Lucchetti *et al.*, ‘Light-induced electric field generated by photovoltaic substrates investigated through liquid crystal reorientation’, *Opt. Mater.*, vol. 73, pp. 64–69, Nov. 2017.

[55] L. Lucchetti, K. Kushnir, A. Zaltron, and F. Simoni, ‘Light controlled phase shifter for optofluidics’, *Opt. Lett.*, vol. 41, no. 2, p. 333, Jan. 2016.

[56] R. C. Chittick, J. H. Alexander, and H. F. Sterling, ‘The Preparation and Properties of Amorphous Silicon’, *J Electrochem Soc*, vol. 116, no. 1, pp. 77–81, 1969.

[57] Y.-Y. Chang *et al.*, ‘Revisiting of a silane explosion in a photovoltaic fabrication plant’, *Process Saf. Prog.*, vol. 26, no. 2, pp. 155–158, Jun. 2007.

[58] J. Liang, E. A. Schiff, S. Guha, B. Yan, and J. Yang, ‘Hole-mobility limit of amorphous silicon solar cells’, *Appl. Phys. Lett.*, vol. 88, no. 6, p. 063512, Feb. 2006.

[59] S. R. OVSHINSKY and A. MADAN, ‘A new amorphous silicon-based alloy for electronic applications’, *Nature*, vol. 276, no. 5687, pp. 482–484, Nov. 1978.

[60] P. R. Ashley and J. H. Davis, ‘Amorphous silicon photoconductor in a liquid crystal spatial light modulator’, *Appl Opt*, vol. 26, no. 2, pp. 241–246, Jan. 1987.

[61] Jan Grinberg *et al.*, ‘A New Real-Time Non-Coherent to Coherent Light Image Converter The Hybrid Field Effect Liquid Crystal Light Valve’, vol. 14, pp. 143217-14–1, 1975.

[62] Y. Igasaki, N. Yoshida, and H. Toyoda, *Spatial light modulation device with a reflection type spatial light modulator and method*. 2003.

[63] S. Fukushima, T. Kurokawa, and M. Ohno, ‘Real-time hologram construction and reconstruction using a high-resolution spatial light modulator’, *Appl. Phys. Lett.*, vol. 58, no. 8, pp. 787–789, Feb. 1991.

[64] L.-J. Meng and M. P. dos Santos, ‘Direct current reactive magnetron sputtered zinc oxide thin films —the effect of the sputtering pressure’, *Thin Solid Films*, vol. 250, no. 1, pp. 26–32, 1994.

[65] A. Janotti and C. G. Van de Walle, ‘Fundamentals of zinc oxide as a semiconductor’, *Rep. Prog. Phys.*, vol. 72, no. 12, p. 126501, Dec. 2009.

[66] R. Al Asmar, G. Ferblantier, F. Mailly, P. Gall-Borrut, and A. Foucaran, ‘Effect of annealing on the electrical and optical properties of electron beam evaporated ZnO thin films’, *Thin Solid Films*, vol. 473, no. 1, pp. 49–53, Feb. 2005.

[67] G. Ferblantier, ‘Etude et réalisation de capteurs d’humidité : Capteur à détection optique, capteur piézoélectrique à base de couche d’oxyde de zinc’, 2004.

[68] Y. Jin, J. Wang, B. Sun, J. C. Blakesley, and N. C. Greenham, ‘Solution-Processed Ultraviolet Photodetectors Based on Colloidal ZnO Nanoparticles’, *Nano Lett.*, vol. 8, no. 6, pp. 1649–1653, Jun. 2008.

[69] D. L. White and M. Feldman, ‘Liquid-crystal light valves’, *Electron. Lett.*, vol. 6, no. 26, pp. 837–839, Dec. 1970.

[70] M. Brinkmann, ‘Structure and morphology control in thin films of regioregular poly(3-hexylthiophene)’, *J. Polym. Sci. Part B Polym. Phys.*, vol. 49, no. 17, pp. 1218–1233, Sep. 2011.

[71] V. Skrypnychuk *et al.*, ‘Ultrahigh Mobility in an Organic Semiconductor by Vertical Chain Alignment’, *Adv. Mater.*, vol. 28, no. 12, pp. 2359–2366, Mar. 2016.

[72] J. Kido, H. Shionoya, and K. Nagai, ‘Single-layer white light-emitting organic electroluminescent devices based on dye-dispersed poly(*N* -vinylcarbazole)’, *Appl. Phys. Lett.*, vol. 67, no. 16, pp. 2281–2283, Oct. 1995.

[73] A. J. Heeger, S. Kivelson, J. R. Schrieffer, and W.-P. Su, ‘Solitons in conducting polymers’, *Rev. Mod. Phys.*, vol. 60, no. 3, pp. 781–850, juillet 1988.

[74] W. J. D. Beenken *et al.*, ‘Sub-bandgap absorption in organic solar cells: experiment and theory’, *Phys. Chem. Chem. Phys.*, vol. 15, no. 39, p. 16494, 2013.

[75] L. Goris *et al.*, ‘Absorption phenomena in organic thin films for solar cell applications investigated by photothermal deflection spectroscopy’, *J. Mater. Sci.*, vol. 40, no. 6, pp. 1413–1418, 2005.

[76] N. Collings, T. D. Wilkinson, A. Jeziorska, A. B. Davey, B. Movaghar, and W. A. Crossland, ‘Charge-injecting layers for liquid crystal light valves’, 2004, p. 421.

[77] W. D. Gill, ‘Drift mobilities in amorphous charge-transfer complexes of trinitrofluorenone and poly- *n* -vinylcarbazole’, *J. Appl. Phys.*, vol. 43, no. 12, pp. 5033–5040, Dec. 1972.

[78] Y. Wang, ‘Photoconductivity of fullerene-doped polymers’, *Nature*, vol. 356, no. 6370, pp. 585–587, avril 1992.

[79] H. Ono and N. Kawatsuki, ‘Orientational holographic grating observed in liquid crystals sandwiched with photoconductive polymer films’, *Appl. Phys. Lett.*, vol. 71, no. 9, p. 1162, 1997.

[80] F. Yao, Y. Pei, Y. Zhang, J. Zhang, C. Hou, and X. Sun, ‘High-resolution photorefractive gratings in nematic liquid crystals sandwiched with photoconductive polymer film’, *Appl. Phys. B*, vol. 92, no. 4, pp. 573–576, Sep. 2008.

[81] H. Seiberle and M. Schadt, ‘LC-Conductivity and Cell Parameters; Their Influence on Twisted Nematic and Supertwisted Nematic Liquid Crystal Displays’, *Mol. Cryst. Liq. Cryst. Sci. Technol. Sect. Mol. Cryst. Liq. Cryst.*, vol. 239, no. 1, pp. 229–244, Jan. 1994.

[82] J. Bateman, M. Proctor, O. Buchnev, N. Podoliak, G. D'Alessandro, and M. Kaczmarek, 'Voltage transfer function as an optical method to characterize electrical properties of liquid crystal devices', *Opt. Lett.*, vol. 39, no. 13, pp. 3756–3759, Jul. 2014.

[83] J. Rivnay *et al.*, 'Structural control of mixed ionic and electronic transport in conducting polymers', *Nat. Commun.*, vol. 7, p. 11287, Apr. 2016.

[84] F. Jonas, G. Heywang, and W. Schmidtberg, 'Solid electrolytes, and electrolyte capacitors containing same', 4,910,645, 20-Mar-1990.

[85] R. Lubianez, 'lubianez.pdf', presented at the 22nd international vacuum web coating conference & AIMCAL fall technical conference, Myrtle Beach, South Carolina, 2008.

[86] L. Scherr, D. A. Ogden, A. W. Mead, N. Spritz, and A. L. Rubin, 'Management of Hyperkalemia with a Cation-Exchange Resin', *N. Engl. J. Med.*, vol. 264, no. 3, pp. 115–119, Jan. 1961.

[87] I. Gualandi, M. Marzocchi, A. Achilli, D. Cavedale, A. Bonfiglio, and B. Fraboni, 'Textile Organic Electrochemical Transistors as a Platform for Wearable Biosensors', *Sci. Rep.*, vol. 6, no. 1, Dec. 2016.

[88] J. Kawahara, P. A. Ersman, I. Engquist, and M. Berggren, 'Improving the color switch contrast in PEDOT:PSS-based electrochromic displays', *Org. Electron.*, vol. 13, no. 3, pp. 469–474, Mar. 2012.

[89] G. Tarabella *et al.*, 'New Opportunities for Organic Electronics and Bioelectronics: Ions in Action', *ChemInform*, vol. 44, no. 27, p. no-no, Jul. 2013.

[90] T.-R. Chou, S.-H. Chen, Y.-T. Chiang, Y.-T. Lin, and C.-Y. Chao, 'Highly conductive PEDOT:PSS films by post-treatment with dimethyl sulfoxide for ITO-free liquid crystal display', *J Mater Chem C*, vol. 3, no. 15, pp. 3760–3766, 2015.

[91] J. C. Rivière, 'THE WORK FUNCTION OF GOLD', *Appl. Phys. Lett.*, vol. 8, no. 7, pp. 172–172, Apr. 1966.

[92] E. E. Huber and C. T. Kirk, 'Work function changes due to the chemisorption of water and oxygen on aluminum', *Surf. Sci.*, vol. 5, no. 4, pp. 447–465, 1966.

[93] R. Lewis and R. Gomer, 'Adsorption of hydrogen on platinum', *Surf. Sci.*, vol. 17, no. 2, pp. 333–345, 1969.

[94] Y. Zhou *et al.*, 'A Universal Method to Produce Low-Work Function Electrodes for Organic Electronics', *Science*, vol. 336, no. 6079, pp. 327–332, Apr. 2012.

[95] H. Kang *et al.*, ‘Simplified Tandem Polymer Solar Cells with an Ideal Self-Organized Recombination Layer’, *Adv. Mater.*, vol. 27, no. 8, pp. 1408–1413, Feb. 2015.

[96] M. Schadt, ‘Liquid crystal materials and liquid crystal displays’, *Annu. Rev. Mater. Sci.*, vol. 27, no. 1, pp. 305–379, 1997.

[97] S.-T. Wu, U. Efron, and L. D. Hess, ‘Birefringence measurements of liquid crystals’, *Appl. Opt.*, vol. 23, no. 21, pp. 3911–3915, 1984.

[98] F. S. Yeung, Y. W. Li, and H.-S. Kwok, ‘Pi-cell liquid crystal displays at arbitrary pretilt angles’, *Appl. Phys. Lett.*, vol. 88, no. 4, p. 041108, Jan. 2006.

[99] C.-J. Hsu, B.-L. Chen, and C.-Y. Huang, ‘Controlling liquid crystal pretilt angle with photocurable prepolymer and vertically aligned substrate’, *Opt. Express*, vol. 24, no. 2, p. 1463, Jan. 2016.

[100] M. Schadt and P. Gerber, ‘Class specific physical properties of liquid crystals and correlations with molecular structure and static electrooptical performance in twist cells’, *Z. Für Naturforschung A*, vol. 37, no. 2, pp. 165–178, 1982.

[101] M. Schadt, ‘Dielectric Heating and Relaxations in Nematic Liquid Crystals’, *Mol. Cryst. Liq. Cryst.*, vol. 66, no. 1, pp. 319–336, Apr. 1981.

[102] S. Murakami and H. Naito, ‘Electrode and interface polarizations in nematic liquid crystal cells’, *Jpn. J. Appl. Phys.*, vol. 36, no. 4R, p. 2222, 1997.

[103] P. Pingel, R. Schwarzl, and D. Neher, ‘Effect of molecular p-doping on hole density and mobility in poly (3-hexylthiophene)’, *Appl. Phys. Lett.*, vol. 100, no. 14, p. 143303, 2012.

[104] C. G. Shuttle, A. Maurano, R. Hamilton, B. O’Regan, J. C. de Mello, and J. R. Durrant, ‘Charge extraction analysis of charge carrier densities in a polythiophene/fullerene solar cell: Analysis of the origin of the device dark current’, *Appl. Phys. Lett.*, vol. 93, no. 18, p. 183501, 2008.

[105] C. G. Shuttle *et al.*, ‘Experimental determination of the rate law for charge carrier decay in a polythiophene: Fullerene solar cell’, *Appl. Phys. Lett.*, vol. 92, no. 9, p. 093311, 2008.

[106] C. H. Kim *et al.*, ‘Persistent photoexcitation effect on the poly (3-hexylthiophene) film: Impedance measurement and modeling’, *Synth. Met.*, vol. 162, no. 5, pp. 460–465, 2012.

[107] T. Bennett *et al.*, ‘Wide area mapping of liquid crystal devices with passive and active command layers’, *Appl. Opt.*, vol. 56, no. 32, p. 9050, Nov. 2017.

[108] A. Peigné, U. Bortolozzo, S. Residori, S. Molin, D. Dolfi, and J.-P. Huignard, ‘Voltage controlled adaptive holographic interferometer using liquid crystals’, 2014, p. 90040J.

[109] A. Chelouche, G. Magnifouet, A. Al Ahmad, N. Leclerc, T. Heiser, and P. Lévêque, ‘Disentangling energetic and charge-carrier dynamic influences on the open-circuit voltage in bulk-heterojunction solar-cells’, *J. Appl. Phys.*, vol. 120, no. 22, p. 225501, Dec. 2016.

[110] J. Li, G. Baird, Y.-H. Lin, H. Ren, and S.-T. Wu, ‘Refractive-index matching between liquid crystals and photopolymers’, *J. Soc. Inf. Disp.*, vol. 13, no. 12, p. 1017, 2005.

[111]P. Schilinsky, C. Waldauf, and C. J. Brabec, ‘Recombination and loss analysis in polythiophene based bulk heterojunction photodetectors’, *Appl. Phys. Lett.*, vol. 81, no. 20, pp. 3885–3887, Nov. 2002.

[112] G. Garcia-Belmonte, P. P. Boix, J. Bisquert, M. Sessolo, and H. J. Bolink, ‘Simultaneous determination of carrier lifetime and electron density-of-states in P3HT:PCBM organic solar cells under illumination by impedance spectroscopy’, *Sol. Energy Mater. Sol. Cells*, vol. 94, no. 2, pp. 366–375, Feb. 2010.

[113] M. Schadt, H. Seiberle, and A. Schuster, ‘Optical patterning of multi-domain liquid-crystal displays with wide viewing angles’, *Nature*, vol. 381, no. 6579, pp. 212–215, mai 1996.

[114] G. Baur, V. Wittwer, and D. W. Berreman, ‘Determination of the tilt angles at surfaces of substrates in liquid crystal cells’, *Phys. Lett. A*, vol. 56, no. 2, pp. 142–144, 1976.

[115] F. Nakano, M. Isogai, and M. Sato, ‘Simple Method of Determining Liquid Crystal Tilt-Bias Angle’, *Jpn. J. Appl. Phys.*, vol. 19, no. 10, p. 2013, 1980.

[116] K.-W. Lee, A. Lien, J. H. Stathis, and S.-H. Paek, ‘Control and Modification of Nematic Liquid Crystal Pretilt Angles on Polyimides’, *Jpn. J. Appl. Phys.*, vol. 36, no. 61, pp. 3591–3597, Jun. 1997.

[117] D.-R. Chiou, L.-J. Chen, and C.-D. Lee, ‘Pretilt Angle of Liquid Crystals and Liquid-Crystal Alignment on Microgrooved Polyimide Surfaces Fabricated by Soft Embossing Method’, *Langmuir*, vol. 22, no. 22, pp. 9403–9408, Oct. 2006.

[118] A. Acreman, ‘Gold nanoparticle liquid crystal composites: synthesis, characterisation and optical nonlinearities’, University of Southampton, 2015.

[119] A. Denisov and J.-L. De Bougrenet De La Tocnaye, ‘Soluble fullerene derivative in liquid crystal: polymer composites and their impact on

photorefractive grating efficiency and resolution', *Appl. Opt.*, vol. 48, no. 10, pp. 1926–1931, Mar. 2009.

[120] M. Proctor, 'Fabrication and characterization of hybrid liquid crystal devices', University of Southampton, 2015.

[121] W. R. Klein and B. D. Cook, 'Unified Approach to Ultrasonic Light Diffraction', *IEEE Trans. Sonics Ultrason.*, vol. 14, no. 3, pp. 123–134, Jul. 1967.

[122] M. Glatthaar *et al.*, 'Organic solar cells using inverted layer sequence', *Thin Solid Films*, vol. 491, no. 1–2, pp. 298–300, Nov. 2005.

[123] G. A. H. Wetzelaer and P. W. M. Blom, 'Ohmic current in organic metal-insulator-metal diodes revisited', *Phys. Rev. B*, vol. 89, no. 24, Jun. 2014.

[124] M. A. Lampert and P. Mark, *Current injection in solids*. Academic Press, 1970.

[125] F. Sadiara, 'Etude du transport de charges dans les polymères semi-conducteurs à faible bande interdite et de son impact sur les performances photovoltaïques', Université de Strasbourg, 2013.

[126] G. Horowitz, D. Fichou, Xuezhou Peng, and P. Delannoy, 'Evidence for a linear low-voltage space-charge-limited current in organic thin films. Film thickness and temperature dependence in alpha-conjugated sexithienyl', *J. Phys.*, vol. 51, no. 13, pp. 1489–1499, 1990.

[127] J. G. Simmons, 'Theory of metallic contacts on high resistivity solids—I. Shallow traps', *J. Phys. Chem. Solids*, vol. 32, no. 8, pp. 1987–1999, 1971.

[128] L. N. Alyabyeva, E. S. Zhukova, M. A. Belkin, and B. P. Gorshunov, 'Dielectric properties of semi-insulating Fe-doped InP in the terahertz spectral region', *Sci. Rep.*, vol. 7, no. 1, Dec. 2017.

[129] A. W. Hains, Z. Liang, M. A. Woodhouse, and B. A. Gregg, 'Molecular Semiconductors in Organic Photovoltaic Cells', *Chem. Rev.*, vol. 110, no. 11, pp. 6689–6735, Nov. 2010.

[130] Z. Liang and B. A. Gregg, 'Compensating Poly(3-hexylthiophene) Reveals Its Doping Density and Its Strong Exciton Quenching by Free Carriers', *Adv. Mater.*, vol. 24, no. 24, pp. 3258–3262, Jun. 2012.

[131] W.-H. Tseng *et al.*, 'Investigations of efficiency improvements in poly(3-hexylthiophene) based organic solar cells using calcium cathodes', *Sol. Energy Mater. Sol. Cells*, vol. 95, no. 12, pp. 3424–3427, Dec. 2011.

[132] M. C. Scharber *et al.*, 'Design Rules for Donors in Bulk-Heterojunction Solar Cells—Towards 10 % Energy-Conversion Efficiency', *Adv. Mater.*, vol. 18, no. 6, pp. 789–794, Mar. 2006.

[133] G. Zhao, Y. He, and Y. Li, ‘6.5% Efficiency of Polymer Solar Cells Based on poly(3-hexylthiophene) and Indene-C60 Bisadduct by Device Optimization’, *Adv. Mater.*, vol. 22, no. 39, pp. 4355–4358, Oct. 2010.

[134] S. Fabiano *et al.*, ‘Ferroelectric polarization induces electronic nonlinearity in ion-doped conducting polymers’, *Sci. Adv.*, vol. 3, no. 6, juin 2017.

[135] J. Li, C.-H. Wen, S. Gauza, R. Lu, and S.-T. Wu, ‘Refractive Indices of Liquid Crystals for Display Applications’, *J. Disp. Technol.*, vol. 1, no. 1, pp. 51–61, Sep. 2005.

List of tables

List of figures

Structure of organic semiconductors

C_{60}: Buckminsterfullerene

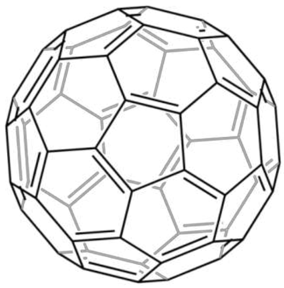

H_2PC: Metal-free Phthalocyanine ($(C_8H_4N_2)_4H_2$)

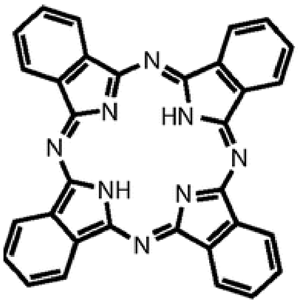

MDMO-PPV: Poly[2-methoxy-5-(3′,7′-dimethyloctyloxy)-1,4-phenylenevinylene] ($(C_{19}H_{28}O_2)_n$)

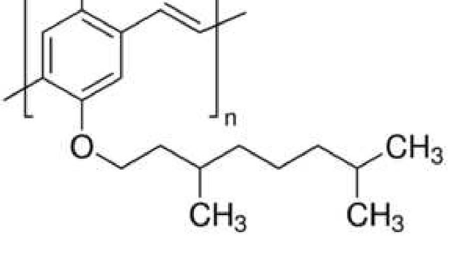

PVK: Poly(9-vinylcarbazole) ($(C_{14}H_{11}N)_n$)

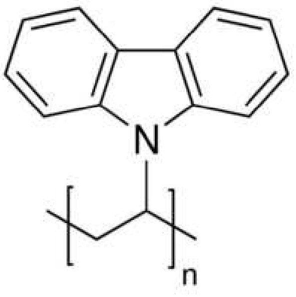

TNF: 2,4,7-trinitro-9-fluorenone ($C_{13}H_5N_3O_7$)

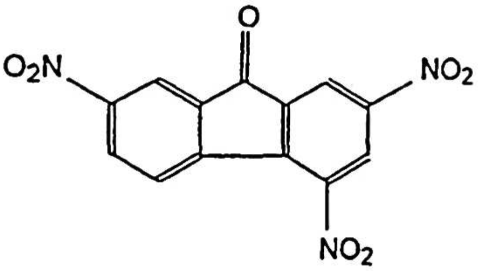

Birefringence of E7

TABLE VI

MEASURED REFRACTIVE INDICES (n_e AND n_o) OF E7 AT $\lambda = 450$, 486, 546, 589, 633, AND 656 nm AT DIFFERENT TEMPERATURE

T	λ (nm)											
	450		486		546		589		633		656	
(°C)	n_e	n_o	n_e	n_o	n_e	n_o	n_e	n_o	n_e	n_o	n_e	n_o
15	1.817	1.5435	1.7921	1.536	1.7664	1.5273	1.7542	1.523	1.7446	1.5197	1.7407	1.5179
20	1.8084	1.5431	1.7847	1.5357	1.7589	1.5269	1.7466	1.5227	1.7378	1.5188	1.7338	1.5177
25	1.8005	1.5424	1.7763	1.5353	1.7512	1.5268	1.7394	1.5225	1.7305	1.5189	1.7263	1.5176
30	1.7909	1.543	1.7679	1.5357	1.7433	1.5271	1.7317	1.5226	1.7229	1.5189	1.719	1.5177
35	1.7811	1.5448	1.7581	1.5369	1.7344	1.5277	1.7231	1.5231	1.7142	1.5191	1.7102	1.5179
40	1.7695	1.547	1.7472	1.5383	1.7237	1.5287	1.7124	1.5239	1.7037	1.5205	1.7001	1.5189
45	1.7549	1.5491	1.7333	1.5406	1.7109	1.5308	1.7001	1.5261	1.6919	1.5221	1.6882	1.5206
50	1.7355	1.5538	1.7154	1.5449	1.6941	1.535	1.6837	1.5299	1.6761	1.526	1.6721	1.5246
55	1.6936	1.569	1.6779	1.5588	1.6601	1.5479	1.6511	1.5428	1.644	1.5377	1.6405	1.5353

Figure 1: Refractive indices (n_e and n_O) of E7 at various wavelength and temperature reproduced from [135]

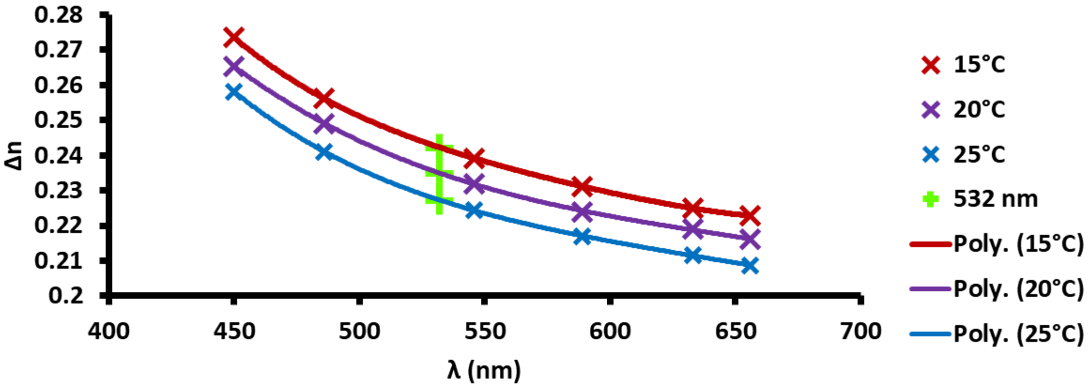

Figure 2: Birefringence of E7 as a function of wavelength at 15°C, 20°C and 25°C using values from [135]

Birefringence of E7

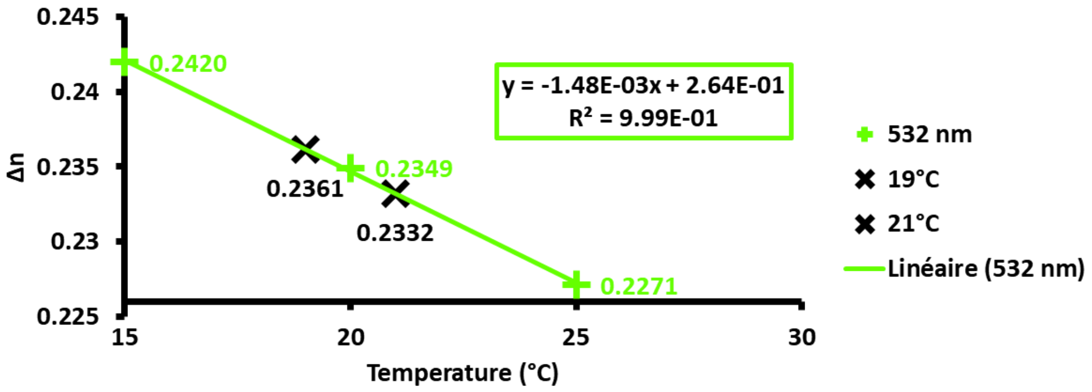

Figure 3: Birefringence of E7 at λ = 532 nm as a function of temperature at 15°C, 20°C and 25°C.

An uncertainty of +/- 1°C corresponds to a variation of birefringence of 0.003.

Electrical model for lateral diffusion

LTSpice XVII(x64) was used to model the impact of surface resistivity on OASLM resolution. A 1V small signal analysis is made at 0.1 Hz and 100 kHz. The electrical parameters for semi-Insulating GaAs are taken from AXT specifications. The model is shown in Figure 1 and all the parameters used for the simulations are given in Table 1.

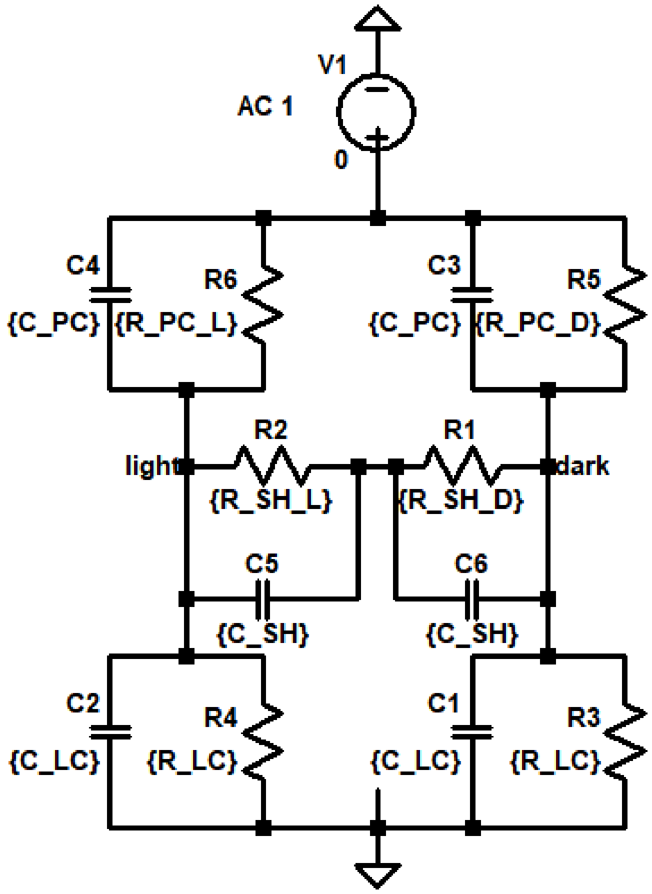

Figure 1: Spice model used to simulate the impact of surface resistivity on OASLM resolution.

Surface (m^2)	C_{PCL}	R_{PCL}	R_{PCL}(D)	C_S	R_S(DARK)	R_S(LIGHT)	C_{LC}	R_{LC}
	C_PC	R_PC_L	R_PC_D	C_SH	R_SH_D	R_SH_L	C_LC	R_LC
1.00E-08	3.26E-15	3.50E+07	3.50E+10	4.00E-14	2.86E+09	2.86E+06	5.94E-14	7.75E+10
2.50E-09	8.16E-16	1.40E+08	1.40E+11	4.00E-14	2.86E+09	2.86E+06	1.49E-14	3.10E+11
1.00E-10	3.26E-17	3.50E+09	3.50E+12	4.00E-14	2.86E+09	2.86E+06	5.94E-16	7.75E+12

Table 1: Parameters used for the simulation

Trend of $\delta\Delta n$ with increasing voltages

In this section, we will observe the impact of thin and thick PCLs on the trend of the $\delta\Delta$n curves.

In section 5.2.1.1, we extracted the capacitance variation of the LC layer comprised between two PEDOT:PSS alignment layers as a function of applied voltage at a frequency of 3162 Hz. At this frequency, it was assumed that most of the potential was dropped across the LC layer. The capacitance values as a function of voltage and the respective CPI curve of the LC cell are depicted in Figure 1.

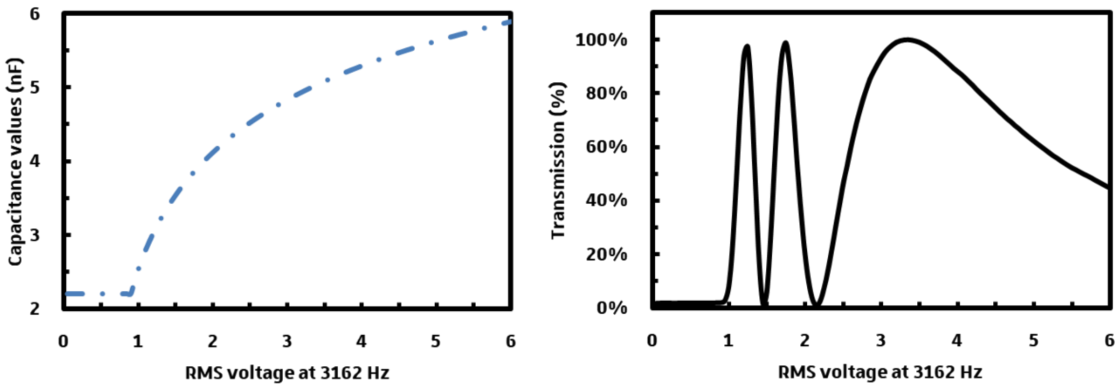

Figure 1: Capacitance values of the LC cell as a function of applied bias at 3162 Hz.

In this frequency region, it is admitted that the LC cell behaviour is purely capacitive as its parallel impedance is very large (see section 5.1). Therefore, we can compute the impact of a thin (200 nm) and a thick (20 μm) P3HT:PCBM layer impedance variation, assuming that there is no photovoltaic effect. The photoconductor impedance (Z_{PCL}) is a parallel RC circuit composed of R_{LC} and C_{LC}. We will assume a perfect photoconductor: at very low light intensities $R_{LC} = \infty$ (open circuit) and at high light intensities R_{LC} is equivalent to a short circuit.

Therefore, at high light intensities, the attenuation is equal to one. At low light intensities, the attenuation is less than unity and needs to be recalculated as a function of voltage as we have a series capacitance (C_{PCL}) in series with the LC cell capacitance (C_{LC}) (which is function of applied voltage). The attenuation equals ($A = \frac{C_{PCL}}{C_{PCL}+C_{LC}}$). We will assume the following values for the PCL (Surface of 3.6 cm^2, relative dielectric constant of 3.6, 3 different thicknesses (t_{PCL} = 200 nm (C_{PCL} = 57 nF), t_{PCL} = 2 µm (C_{PCL} = 5.7 nF) and t_{PCL} = 20 µm (C_{PCL} = 0.57 nF))).

The attenuation (A) as a function of voltage and the CPI curves at the lowest (dark dotted line ($V_{LC} = \frac{V}{A}$)) and highest light intensities (dark continuous line ($V_{LC} = V$)) are depicted in Figure 2 on the left for a PCL thickness of 200 nm (a), 2 μm (b) and 20 μm (c). On the right side of Figure 2, the birefringence has been recalculated for each curve and is plotted as a function of voltage at low (dark dotted line) and high (dark continuous line) light intensities. δΔn is depicted on the right versus voltage (red curve) and a blue square indicate its maximum.

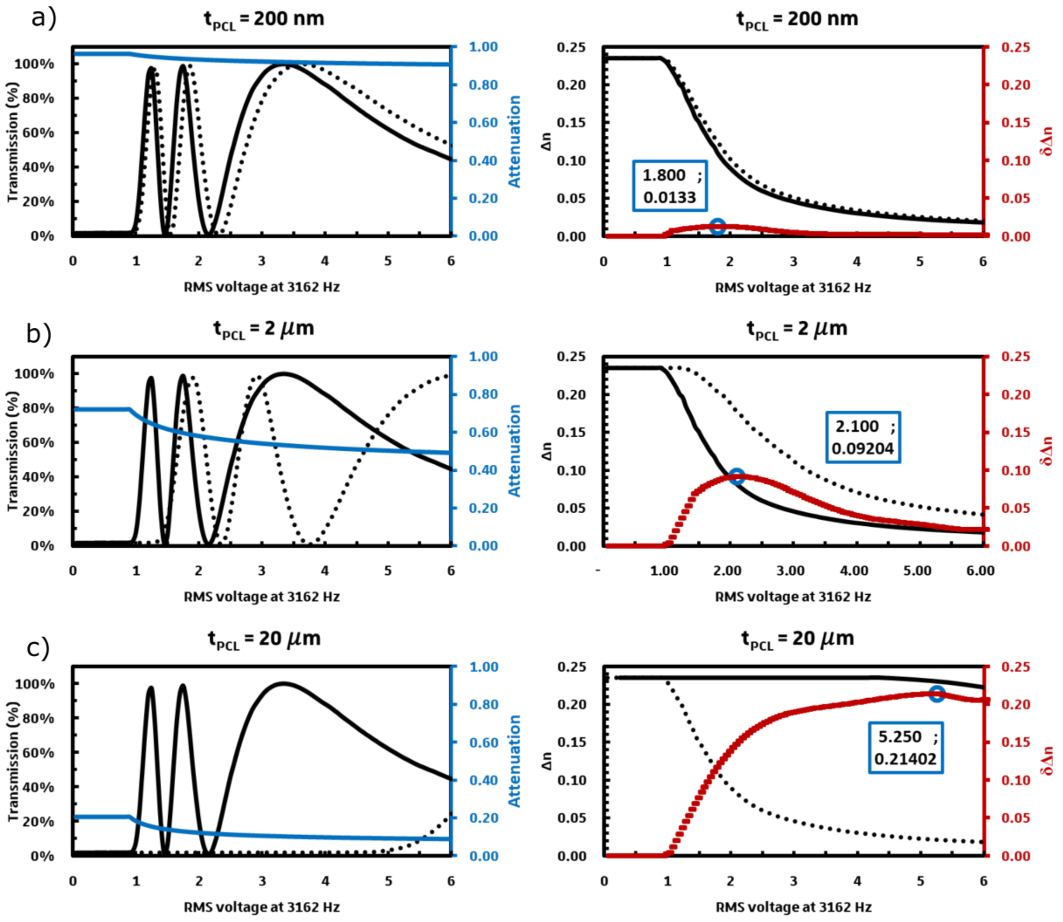

Figure 2: (Left) Attenuation as a function of applied voltage used to calculate the attenuated CPI curves (dark dotted line). (Right) Respective Δn values for each curves and magnitude of δΔn as a function of applied voltage.

Trend of $\delta\Delta n$ with increasing voltages

The trend of $\delta\Delta n$ is the following: it should increase and attain a maximum before decreasing. Its magnitude depends on the PCL thickness, as the thickness of the PCL layer increases, its impedance increases and therefore the LC modulation increases. A consequence of this is that the maximum $\delta\Delta n$ shifts towards higher voltages as the thickness of the PCL increases.

This short study is valid for E7 and the same trend should be observed for an OASLM using a LC with a positive dielectric anisotropy and a PCL. However, using a photovoltaic layer, assuming no threshold voltage a negligible photoconductivity variation $\delta\Delta n$ should be at its maximum around 0V then decrease.

Crystal rotation method

1. *Crystal rotation measurements at low intensity*

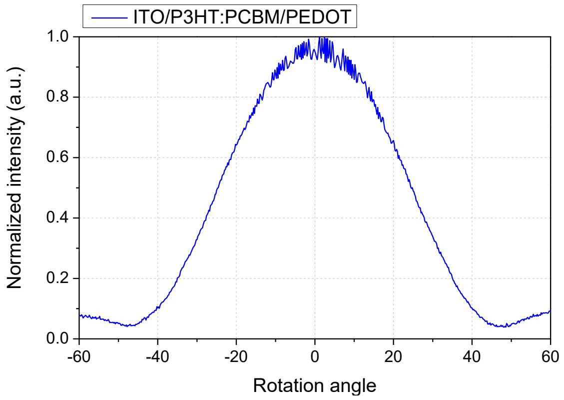

Figure 1: ITO/P3HT:PCBM/PEDOT/ LC / PEDOT cell

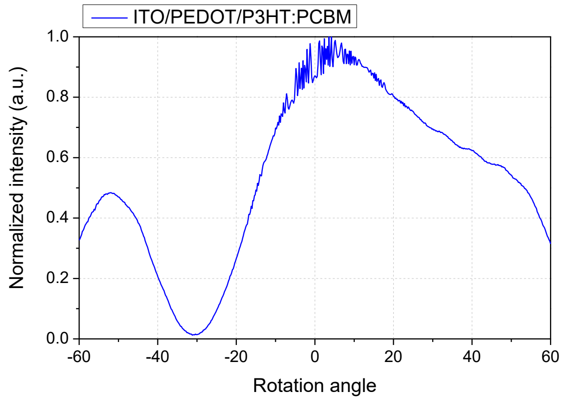

Figure 2: ITO/ PEDOT /P3HT:PCBM/ LC / PEDOT cell

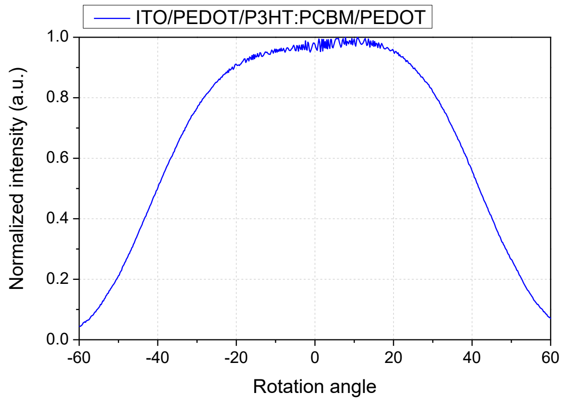

Figure 3: ITO/ PEDOT /P3HT:PCBM/PEDOT/ LC / PEDOT cell

Conclusions:

- Cells containing a layer of PEDOT in contact with the LC show good planar alignment with a small pretilt angle (almost symmetric crystal rotation curves)
- Cells having a layer of P3HT:PCBM in contact with the LC have high pretilt (highly asymmetric crystal rotation curve)

2. *Crystal rotation measurements at different light intensities*

Measurements for different light intensities were done without removing the cell from the holder (the same spot on the cell was probed). The intensity of the probe beam increases between the measurements.

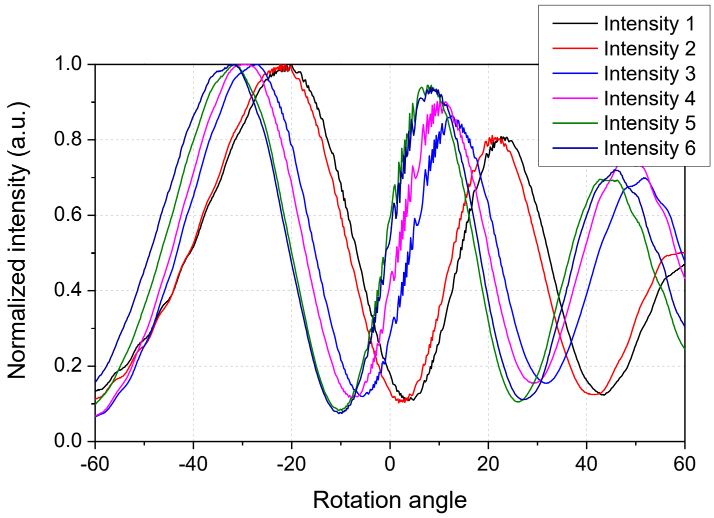

Figure 4: ITO/P3HT:PCBM (1:1)/E7/PEDOT:PSS/ITO cell

	Beam power
Intensity 1	< a few µW
Intensity 2	~14 µW
Intensity 3	370 µW
Intensity 4	778 µW
Intensity 5	6.75 mW
Intensity 6	14 mW

The cell was probe with the lowest intensity beam again after a few hours resting in the dark. The curve is very similar to the initial one.

3. Simulated response of crystal rotation measurements

Simulated response of crystal rotation measurements assuming the following boundary conditions for each alignment layer:

1. *LC pretilt angle of 0° one AL*
2. *Increasing pretilt angle on the other AL*

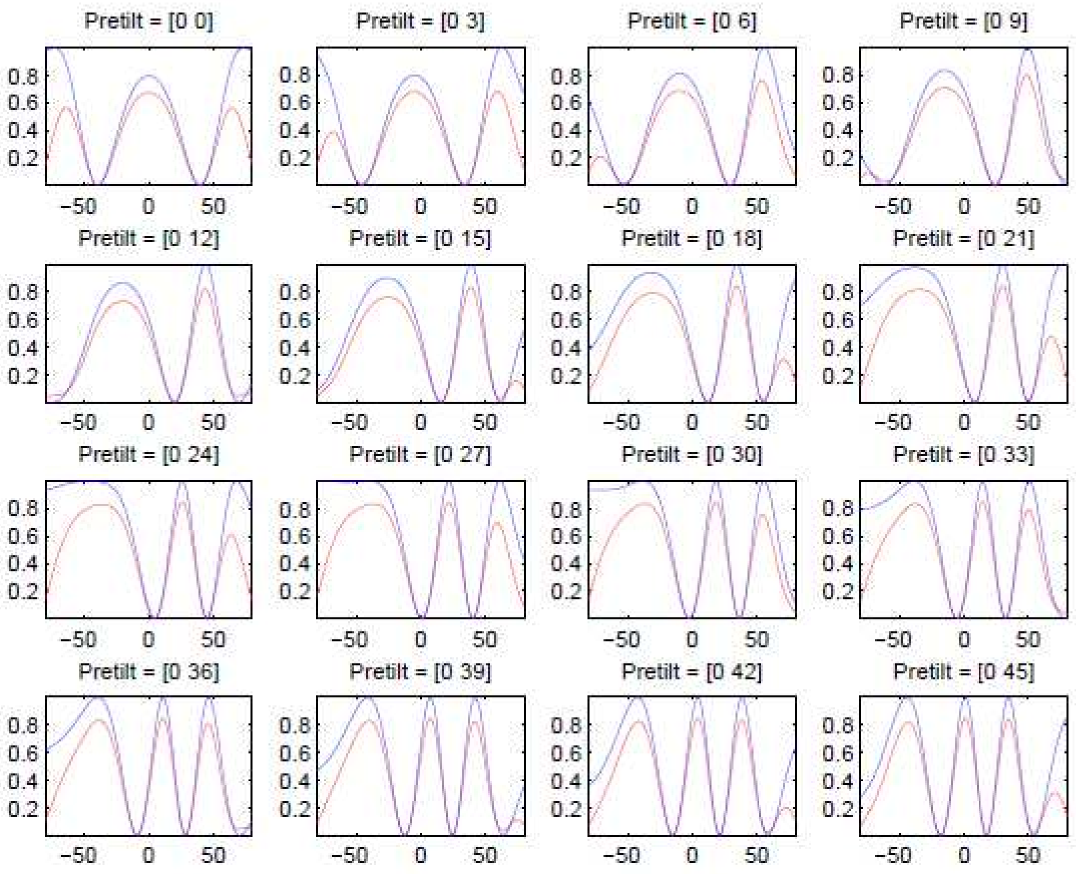

Conclusions:

Crystal rotation curves shift to the left with increasing light intensity, indicating an increase of the liquid crystal reorientation (deviation from the planar alignment). This can be caused either by the LC pretilt increase at the polymer boundary or by the LC reorientation in the cell due to photovoltage.

Contact Angle of water

1) Sample Structure

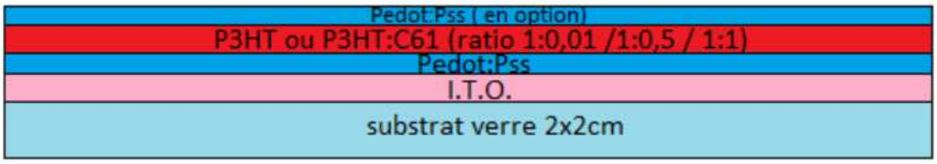

Figure 1: Sample structure

2) Experimental protocol

- A micro drop of deionized water of 5 µl is deposited on the surface of the sample
- A photo of the drop of water is recorded by the camera
- It is possible to illuminate more or less intensely the sample with a LED.
- The picture taken is then processed by the "ImageJ" software to determine the angle of contact between the horizontal and the tangent at the base of the drop of water

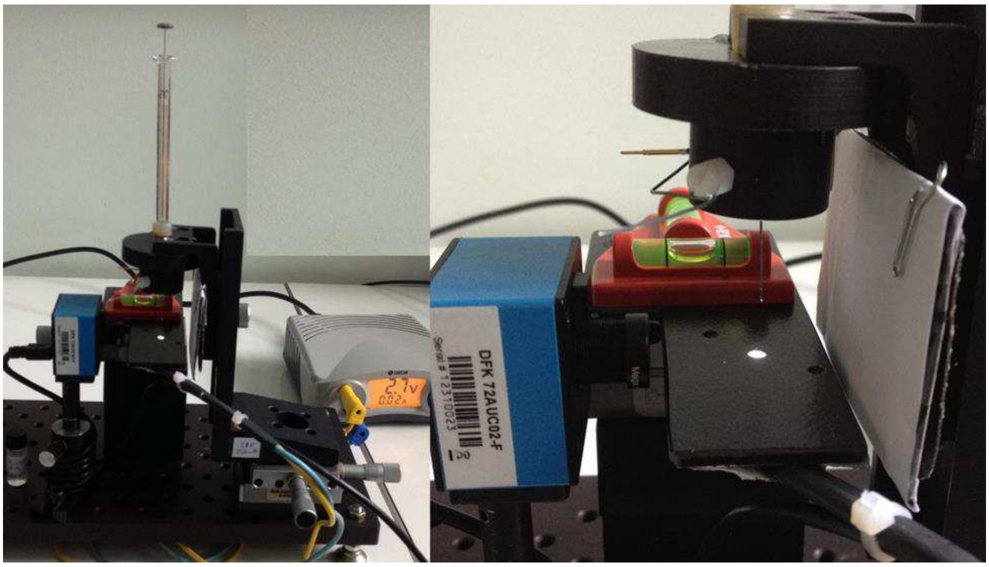

Figure 2: Experimental setup

3) Contact angles measurements

Contact Angle of water

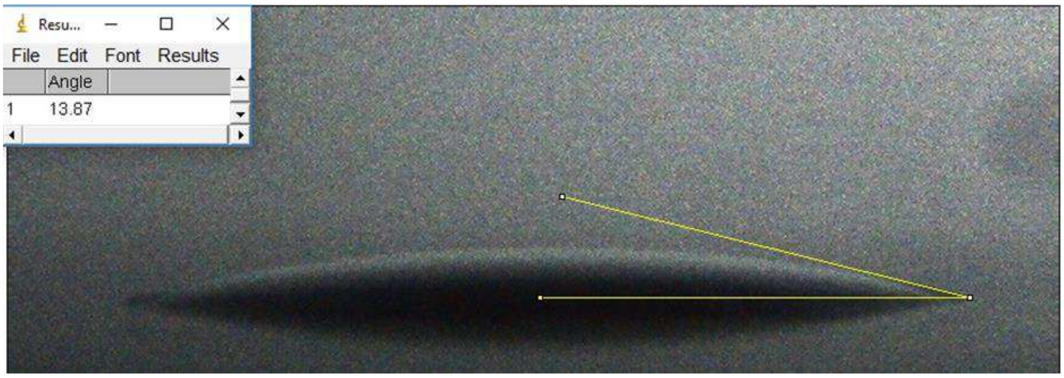

```
   Angle
1  13.87
```

Figure 3: ITO/PEDOT:PSS

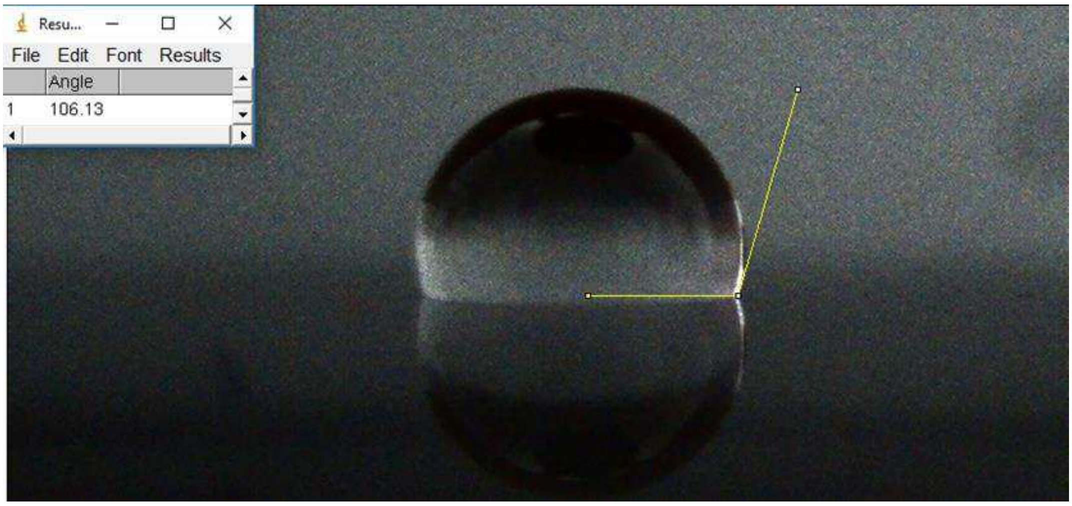

```
   Angle
1  106.13
```

Figure 4: ITO/PEDOT:PSS/P3HT:PCBM(1:1)

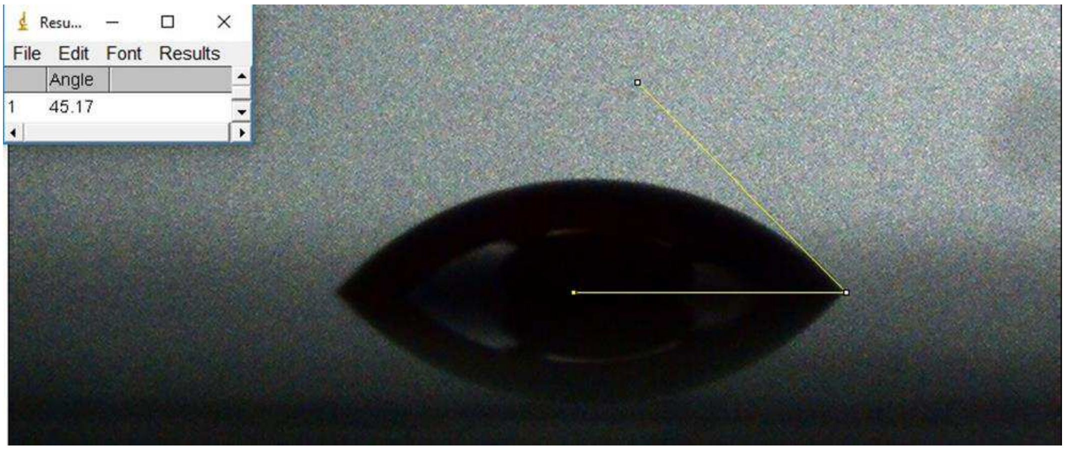

```
   Angle
1  45.17
```

Figure 5: ITO/PEDOT:PSS/P3HT:PCBM(1:1)/PEDOT:PSS

Contact Angle of water

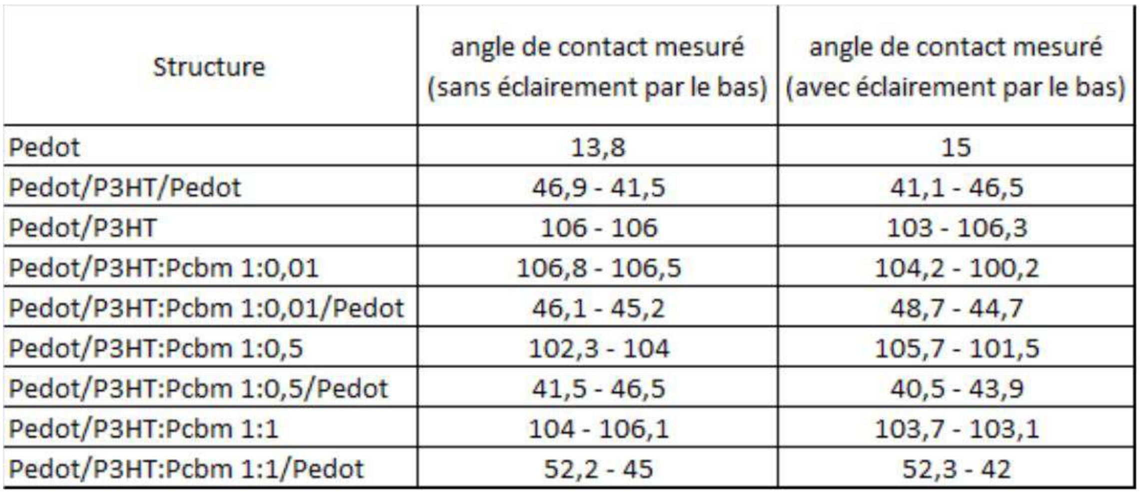

Structure	angle de contact mesuré (sans éclairement par le bas)	angle de contact mesuré (avec éclairement par le bas)
Pedot	13,8	15
Pedot/P3HT/Pedot	46,9 - 41,5	41,1 - 46,5
Pedot/P3HT	106 - 106	103 - 106,3
Pedot/P3HT:Pcbm 1:0,01	106,8 - 106,5	104,2 - 100,2
Pedot/P3HT:Pcbm 1:0,01/Pedot	46,1 - 45,2	48,7 - 44,7
Pedot/P3HT:Pcbm 1:0,5	102,3 - 104	105,7 - 101,5
Pedot/P3HT:Pcbm 1:0,5/Pedot	41,5 - 46,5	40,5 - 43,9
Pedot/P3HT:Pcbm 1:1	104 - 106,1	103,7 - 103,1
Pedot/P3HT:Pcbm 1:1/Pedot	52,2 - 45	52,3 - 42

Table 1: Summary of the contact angle measurements

SCLC curve fitting

Tutorial based on Sadiara's measurements on PCBM and CHLAR1.

If there is an SCLC regime (or a regime limited by charge injection), we should have a dependence of the current (I) on the square of the voltage (V). To distinguish between SCLC or charge injection limited regimes, it is necessary to elaborate several devices with different thicknesses, as the dependence of J on the thickness is different in the two regimes. If SCLC takes place, the current density (J) will depends on the voltage (V) as:

$$J = \frac{9}{8}\varepsilon_0\varepsilon\mu_0 e^{0.89\gamma\sqrt{E}}\frac{V^2}{d^3} \qquad (1)$$

Where ε are the dielectric constants, μ_o is the charge mobility at zero applied bias, γ is the mobility factor dependence on the electric field and d is the sample thickness. This equation (1) will simplify on the most usual equation (2) if the mobility is not dependent (or weakly dependent) on the electric field (i.e. $\gamma = 0$):

$$J = \frac{9}{8}\varepsilon_0\varepsilon\mu_0\frac{V^2}{d^3} \qquad (2)$$

Introducing the two parameters named P_1 and P_2 with the following definitions:

$$P_1 = \frac{9}{8}\varepsilon_0\varepsilon\mu_0\frac{1}{d^3} \qquad (3)$$

$$P_2 = 0.89\frac{\gamma}{\sqrt{d}} \qquad (4)$$

Then equation (1) can be re-written as:

$$J = P_1 e^{P_2\sqrt{V}}V^2 \qquad (5)$$

Or:

$$Ln(J) = Ln(P_1) + P_2\sqrt{V} + 4Ln(\sqrt{V}) \qquad (6)$$

If we plot $Ln(J) - 4Ln(\sqrt{V})$ as a function of $\sqrt{V}$, then a simple linear fit will give P_2 as the slope and Ln (P_1) as the intercept for $V = 0$.

This simple method is use to determine P_1 and P_2. After that, the formalism used is easily understandable. We chose with Sadiara to write J as a function of P_1 and P_2 (equation (5)) because both coefficients depends on d, the thickness of the sample. Indeed, $P_1 = \frac{9}{8}\varepsilon_0\varepsilon\mu_0\frac{1}{d^3}$ and $P_2 = 0.89\frac{\gamma}{\sqrt{d}}$. Then the ratio:

$$\frac{{P_1}^{1/3}}{{P_2}^2} = \frac{\left(\frac{9}{8}\varepsilon_0\varepsilon\mu_0\right)^{1/3}}{(0.89\gamma)^2} \qquad (7)$$

It does not depend on the thickness (stating that μ_0 and γ are equal for every sample).

Case of PCBM

3 diodes (2 mm^2) on two samples (thickness 280 and 200 nm)

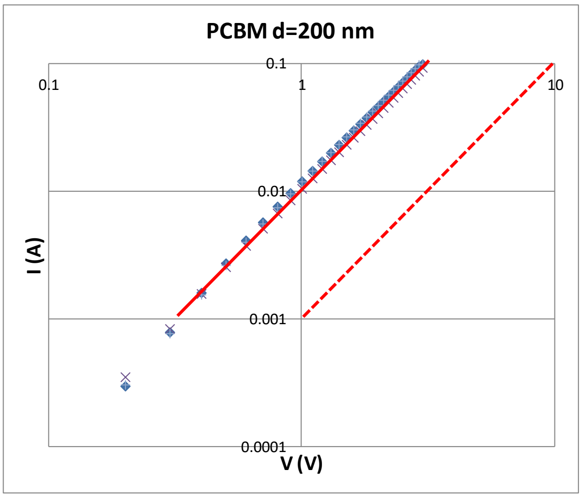

Figure 1: (I-V) in a Log-Log scale

As seen in figure 1, the (I-V) curve is correctly described by a linear dependence with a slope equal to 2. It means that for the three diodes, equation (2) is valid and $P2 = 0$. The mobility is not field dependent.

If we plot $Ln(J) - 4Ln(\sqrt{\mathrm{V}})$ as a function of $\sqrt{\mathrm{V}}$ according to equation (6) we obtain the graph in Figure 2 (J is in A/m^2 with a diode surface of 2 mm^2).

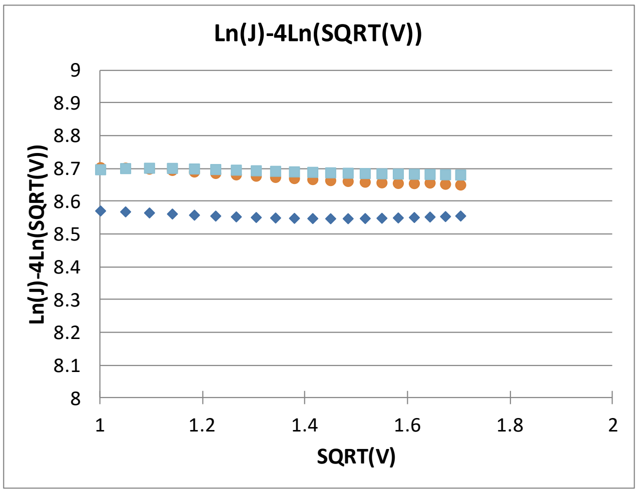

Figure 2: $Ln(J) - 4Ln(\sqrt{\mathrm{V}})$ as a function of $\sqrt{\mathrm{V}}$

The part $Ln(J) - 4Ln(\sqrt{\mathrm{V}})$ is almost constant as a function of $\sqrt{\mathrm{V}}$ (equation (6) with P_2 = 0) and Ln (P_1) varies from 8.55 to 8.7 depending on the diodes. From equation (3), we obtain:

$$\mu_o = \frac{8}{9}\frac{d^3}{\varepsilon_0 \varepsilon} P_1$$

With $d = 200 \times 10^{-9}\, m, \varepsilon = 3, \varepsilon_0 = 8.85 \times 10^{-12} \frac{F}{m}$

It follows with $Ln(P1) = (8.6 \pm 0.1)$ that $\mu_0 = (1.5 \pm 0.1) \times 10^{-2}\, cm^2/(V.s)$. From the other thickness (280 nm), we obtain $\mu_0 = (1.4 \pm 0.6) \times 10^{-2}\, cm^2/(V.s)$ with $Ln\,(P1) = (7.5 \pm 0.5)$. To check that SCLC takes place, for two thicknesses d_1 and d_2, we obtain two parameters P_1 (d_1) and P_1 (d_2). Then according to equation (3), we should have:

$$\frac{\mathrm{P}_1(\mathrm{d}_1)}{\mathrm{P}_1(\mathrm{d}_2)} = \frac{(\mathrm{d}_2)^3}{(\mathrm{d}_1)^3}$$

In our case, the first ratio is equal to 3 while the second one is equal to 2.7. This is acceptable as the precision on the thickness measurement is not so good (10 nm roughly). Taking into account the thickness uncertainty, the second ratio is equal to (2.7 ± 0.6). Moreover, if the current is limited by charge injection then the ratio will be equal to:

$$\frac{P_1(d_1)}{P_1(d_2)} = \frac{d_2}{d_1}$$

i.e. equal to (1.4 ± 0.1). We can then conclude unambiguously that SCLC takes place.

Case of CHLAR4

3 diodes (2 mm²) on two samples (thickness 400 and 440 nm)

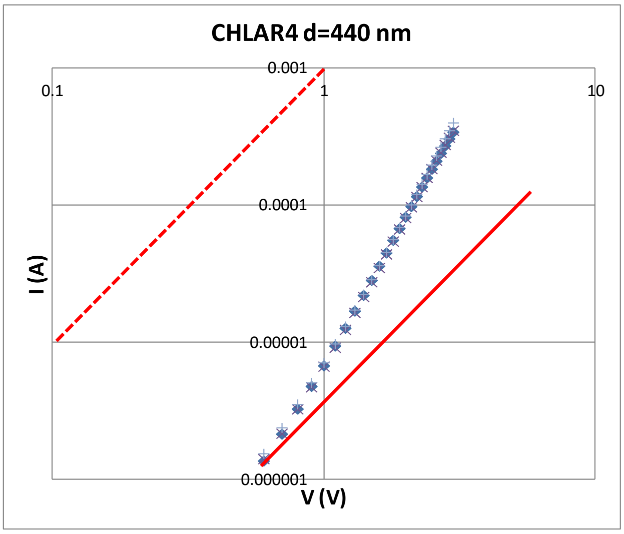

Figure 3: (I-V) in a Log-Log scale

The slope of the (I-V) curves in Log-Log scale is unambiguously greater than 2. Therefore equation (1) should be used or alternatively equation (6) as in Figure 4.

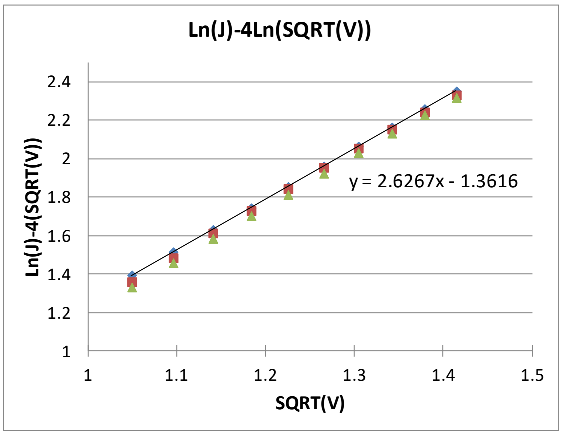

Figure 4: $Ln(J) - 4Ln(\sqrt{V})$ as a function of $\sqrt{V}$

This time we can define P_1 and P_2 for every diode with the following results:

$$P1 \;=\; (0.24 \pm 0.02) and \; P2 \;=\; (2.67 \pm 0.03)\; V^{-1/2}$$

Therefore, we find:

$$\mu_0 \;=\; (6.8 \;\pm\; 0.5) \times \; 10^{-6}\; cm^2/(V.s)$$

To check the parameters extracted, we can fit the experimental curve in Figure 3 with equation (5) (Figure 5).

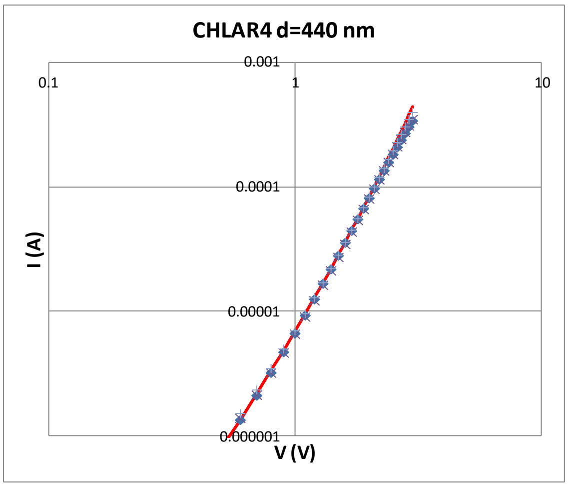

Figure 5: same as figure 3 with fit as a red line.

From the sample with a thickness of 400 nm, we find

$$P1 = (0.8 \pm 0.1)\ and\ P2 = (2.85 \pm 0.03)\ V^{-1/2}$$

Therefore, we find:

$$\mu_0 = (1.7 \pm 0.2) \times 10^{-5}\ \mathrm{cm^2/(V.s)}$$

The control procedure is somewhat different from when $P2 = 0$. We can check here that:

$$\frac{P_1^{1/3}}{P_2^{2}} = \frac{(\frac{9}{8}\varepsilon_0\varepsilon\mu_o)^{1/3}}{(0.89\gamma)^2}$$

The ratio does not depend on the thickness. For the first thickness, this ratio is equal to 0.9 and for the second to 1. Those two ratios can be considered as equal within the experimental uncertainty.

From the two thicknesses, we can also calculate from equation (4) the value of γ. For 440 nm thick sample, we have $\gamma = 0.002\ \mathrm{m^{1/2}V^{-1/2}}$ and for the 400 nm thick sample, the same value for γ.

Thomas REGRETTIER

Modulateurs de lumière à commande optique composés d'une couche photovoltaïque organique.

Résumé

Les performances des modulateurs de lumières à commande optique (OASLMs) à base de cristaux liquides (CLs) dépendent fortement des propriétés de la couche photosensible. Afin de concilier transparence, résolution latérale et production à bas coûts, les semi-conducteurs organiques apparaissent comme des candidats idéaux. Nous avons choisi d'utiliser un mélange P3HT:PCBM comme couche photosensible. Nos résultats ont montré que les cristaux liquides se réorientaient en fonction de l'intensité lumineuse seule et sans tension appliquée. Des mesures complémentaires indiquent que l'effet photovoltaïque est à l'origine de ce phénomène. Ce type de dispositif nous permet de moduler spatialement l'orientation des CLs et démontre son potentiel dans des applications liées à l'holographie. Un second type de dispositif intégrant des couches d'interfaces de PEIE et de PEDOT:PSS nous permet de contrôler l'orientation des CLs et donne de nouvelles pistes permettant de fabriquer des OASLMs autonomes.

Mots-clés : optique, électronique, photovoltaïque, cristaux liquides, afficheurs, fabrication de dispositifs optoélectroniques, photonique, semi-conducteurs organiques, OASLM

Summary

The performances of liquid crystals (LCs) based optically addressed Spatial Light Modulators (OASLMs) strongly depends on the photosensitive layer properties. To accommodate device transparency, lateral resolution and low cost production, organic semiconductors appear as the ideal candidates. We chose to use a P3HT: PCBM blend as the photosensitive layer. Our results showed that the liquid crystals reorient according to the luminous intensity alone and without external power supply. Additional measurements indicate that the photovoltaic effect is at the origin of this phenomenon. This type of device allowed spatial modulation of the LCs orientation and demonstrates its potential in holographic applications. A second type of device integrating interfacial layers of PEIE and PEDOT: PSS allowed us to control the orientation of the LCs and gives promising routes towards the design of self-sustainable OASLMs.

Keywords: optics, electronics, photovoltaics, liquid crystals, displays, optoelectronic devices, photonics, organic semiconductors, OASLM